Università di Pisa
Dipartimento di Ingegneria dell'Informazione

Laurea Magistrale in

Ingegneria Robotica e dell'Automazione

Nonlinear Control of Relative Motion in Space using Extend Linearization Technique

Giovanni Franzini

Relatori:

Prof. Mario Innocenti

Prof. Lucia Pallottino

Anno Accademico 2013/2014

Sommario

La NASA ha identificato gli algoritmi per la guida relativa nello spazio come una delle tecnologie chiave per lo sviluppo delle missioni future. Ogni qualvolta due o più veicoli spaziali debbono coordinare il loro moto, oppure deve essere eseguita una manovra di rendezvous terminale, è richiesto l'utilizzo di una legge di controllo robusta per governare il moto relativo tra gli oggetti. Questa legge dovrà garantire la sicurezza delle operazioni e minimizzare il consumo di carburante, vista l'impossibilità di rifornimenti in orbita. In questa tesi, la tecnica di linearizzazione estesa è stata utilizzata per lo sviluppo di leggi pseudo-ottime e robuste per il controllo delle equazioni non lineari di moto relativo. Sono state inoltre considerate le perturbazioni tipiche delle orbite terrestri basse per analizzare la fisibilità dei controllori proposti. Tutte le simulazioni sono state condotte utilizzando dati provenienti da missioni reali.

Abstract

Relative guidance algorithms for space applications were identified by NASA as an enabling technology for future missions development. Whenever two or more space vehicles must coordinate their motion or a terminal rendezvous has to be performed, a robust control of the relative motion occurring between the two objects is requested. Control must guarantee operation safety and minimize fuel consumption, since refuelling operations are currently too expensive. In this thesis, the extend linearization technique was adopted to design pseudo-optimal and robust control laws for nonlinear equations of relative motion. Typical perturbations of low Earth orbits were considered, in order to understand the feasibility of the developed controllers. Simulations were performed using data from real missions.

Contents

Chapter 1

Introduction

Relative guidance is a key technology for the development of future space missions. Operations such as rendezvous and docking, inspection and servicing require the on-board presence of a relative guidance and control system, that, given in input the relative position and attitude estimations, steers the spacecraft ensuring the safety of the involved vehicles and fuel consumption optimization. Nowadays, these operations are performed with the human intervention, except few cases (e.g. ESA's ATV). In order to lighten control station workload and to start developing new and ambitious space missions for deep space exploration, space vehicles autonomy must increase. The identification of robust control laws for relative motion in space is a fundamental step towards the development of relative guidance and control systems for space.

In this thesis, the relative motion problem is studied an the SDRE method (State-Dependent Riccati Equation) was applied in order to identify a new suitable control law for the development of a relative guidance system. Simulations were set up using data taken from real missions. Space perturbations were also considered to understand the potentialities of the SDRE method and its applicability to real situations.

The thesis is organized as follows. Space flight mechanics and relative motion are introduced in Chapter 2. The two body problem and Keplerian motion are dis-

cussed. The most important perturbations for low Earth orbits are also presented. After introducing the main concepts of space flight mechanics, equations for relative motion description are developed. Two formalisms are considered: the Cartesian and the orbital element differences descriptions.

In Chapter 3 the relative motion problem is stated, followed by a discussion about application and control requirements. A literature review of the solutions proposed during the years is presented, supported by a classification based on the control approach used and by a series of references to the most important works.

A recently developed near-optimal control law is then presented in Chapter 4. This solution is currently one of the closest to optimality, thanks to a series of mathematical tools developed by the authors.

The control method object of this thesis, the State-Dependent Riccati Equation control, is discussed in Chapter 5. SDRE theory is presented with its most important contributes. The main theorems for proving control stability and optimality are there proposed and a brief discussion about resolution methods for algebraic Riccati equation, which is at the base of the SDRE control, is offered. The chapter ends with a summary of some SDRE-based solutions proposed in literature for relative motion control.

In Chapter 6 the SDRE control is applied to the relative motion problem. Three different controllers are developed, using three possible parametrizations of the nonlinear equation of unperturbed relative motion. Controllers performance are then compared to the near-optimal control presented in Chapter 4.

Using the extended linearization technique, a nonlinear $\mathcal{H}_\infty$ controller is proposed in Chapter 7 for relative motion control in presence of perturbations. In particular, an SDRE-$\mathcal{H}_\infty$ controller is developed and compared to a typical SDRE controller based on nonlinear equations of relative perturbed motion. The use of a simpler SDRE controller using linearized equations is also considered.

Chapter 8 concludes the thesis with a discussion of the work presented and the results achieved by the proposed solutions.

Chapter 2

Space Flight Mechanics and Relative Motion

The aim of this chapter is to introduce the unfamiliar reader to the essential elements of the space flight mechanics, in order to understand the development of the equations of relative motion, subject of this thesis. The chapter is organized in two main sections.

In Section 2.1 the two body problem is discussed and the Keplerian motion is introduced. The orbital elements, a set of parameters for orbit description, are presented and a brief introduction to the main space perturbations for lower Earth orbits is proposed. The section ends with a mathematical model for propulsion, that will be used to account for satellite mass variation due to propellant consumption.

Section 2.2 presents the main formalization used for space relative motion description. The Cartesian representation is the most diffused, since it allows the use of sensors measurements for relative position and velocity without the introduction of any transformation or coordinate change. Orbit elements difference may be used to describe relative motion too. the result is the orbital elements difference description.

The theory and the results proposed in this chapter were developed using [1–4] as reference textbooks, whereas propulsion modelling was adapted from [5].

2.1 Essential Orbital Mechanics

2.1.1 The Two-Body Problem and the Keplerian Motion

Consider two point masses in an inertial reference frame. The masses are attracted to each other according to *Newton's Law of Universal Gravitation*. In particular, the attraction force exerted by body i on body j is given by

$$\boldsymbol{F}_{g_i} = -G\frac{m_i m_j}{r_{ij}^3}\boldsymbol{r}_{ji}$$

where $\boldsymbol{r}_{ji} = \boldsymbol{r}_i - \boldsymbol{r}_j$ with $\boldsymbol{r}_i$ position of body i with respect to the origin of the inertial reference frame, $G = 6.6726 \times 10^{-11}\,\mathrm{m}^3/(\mathrm{kg\,s}^2)$ is the *universal gravitational constant* and m_i is the mass of body i.

Assuming that the only force acting on the two point masses is the gravitational force, equation of motion for the two bodies can be computed using Newton's Second Law,

$$m_1\frac{\mathrm{d}^2}{\mathrm{d}t^2}\boldsymbol{r}_1 = G\frac{m_1 m_2}{r^3}\boldsymbol{r}$$
$$m_2\frac{\mathrm{d}^2}{\mathrm{d}t^2}\boldsymbol{r}_2 = -G\frac{m_1 m_2}{r^3}\boldsymbol{r}$$

having introduced the relative position vector $\boldsymbol{r} = \boldsymbol{r}_2 - \boldsymbol{r}_1$. The relative acceleration of the bodies is given by

$$\frac{\mathrm{d}^2}{\mathrm{d}t^2}\boldsymbol{r} = \frac{\mathrm{d}^2}{\mathrm{d}t^2}\boldsymbol{r}_2 - \frac{\mathrm{d}^2}{\mathrm{d}t^2}\boldsymbol{r}_1 = -G\frac{m_1 + m_2}{r^3}\boldsymbol{r} \tag{2.1}$$

During the study of the motion of a satellite around a planet (or a *primary body*), the satellite mass is often negligible. The *gravitational parameter* $\mu \triangleq GM$ is then introduced, where M is the planet mass, and Equation (2.1) can be written in the following form,

$$\frac{\mathrm{d}^2}{\mathrm{d}t^2}\boldsymbol{r} = -\frac{\mu}{r^3}\boldsymbol{r} \tag{2.2}$$

Equation (2.2) describes the motion of a small body around a primary body in

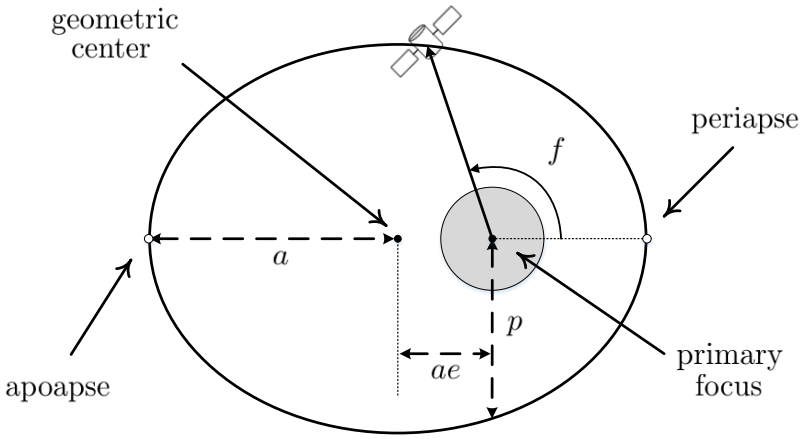

Figure 2.1: Ellipse geometry.

absence of perturbations. This type of motion is usually referred to as *Keplerian motion*. In the following, it will be assumed that the primary body is the Earth, which astronomical symbol is $\oplus$. In this case $M = 59.736 \times 10^{23}\,\mathrm{kg}$ and $\mu = 398\,600\,\mathrm{km/s^2}$.

An important property of the Keplerian motion is the massless angular momentum conservation. Satellite's *massless angular momentum* is defined as

$$\boldsymbol{h} \triangleq \boldsymbol{r} \times \boldsymbol{v}$$

where $\boldsymbol{v} = \frac{\mathrm{d}}{\mathrm{d}t}\boldsymbol{r}$. Left multiplication of Equation (2.2) by $\boldsymbol{r}$ (cross product) yields

$$\boldsymbol{r} \times \frac{\mathrm{d}^2}{\mathrm{d}t^2}\boldsymbol{r} + \boldsymbol{r} \times \frac{\mu}{r^3}\boldsymbol{r} = \boldsymbol{0} \quad \Longleftrightarrow \quad \boldsymbol{r} \times \frac{\mathrm{d}}{\mathrm{d}t}\boldsymbol{v} = \boldsymbol{0} \tag{2.3}$$

Left side of previous equation can be written as

$$\boldsymbol{r} \times \frac{\mathrm{d}}{\mathrm{d}t}\boldsymbol{v} = \frac{\mathrm{d}}{\mathrm{d}t}\left(\boldsymbol{r} \times \boldsymbol{v}\right) = \frac{\mathrm{d}}{\mathrm{d}t}\boldsymbol{h}$$

and together with Equation (2.3) proves that $\boldsymbol{h}$ is constant.

Satellite's trajectory equation may be obtained by integration of Equation (2.2). Different solutions were proposed during the years (a summary of classical solutions

can be found in [2]). All the possible trajectory are represented by the conic polar equation[1],

$$r = \frac{p}{1 + e\cos f} \tag{2.4}$$

where e and p are respectively the conic *eccentricity* and *semilatus rectum* and f is the satellite *true anomaly* (see Figure 2.1).

Two useful expressions for p are the following. The first one valid when $e \neq 1$

$$p = a\left(1 - e^2\right) \tag{2.5}$$

where a is the conic *semi-major axis*; the second one as a function of satellite's angular momentum

$$p = \frac{h^2}{\mu} \tag{2.6}$$

The eccentricity defines the type of conic and thus the orbit shape. In particular

- $e = 0 \rightarrow$ circumference;
- $0 < e < 1 \rightarrow$ ellipse;
- $e = 1 \rightarrow$ parabola;
- $e > 1 \rightarrow$ hyperbola.

In this thesis only elliptical and circular orbits are considered. The ellipse will be considered as the general orbit shape.

The primary body occupies one of the conic focus: the *primary focus*. The closest point on the ellipse to the primary focus is called *periapse*, whereas the furthest point is the *apoapse*.

The true anomaly is measured from periapse and its time derivative can be computed using $\boldsymbol{h}$. Let introduce a Cartesian coordinate system, with a radial and a perpendicular unit vector, respectively $\hat{\boldsymbol{i}}_r$ and $\hat{\boldsymbol{i}}_\perp$ (Figure 2.2). The position vector

[1] cfr. Kepler's First Law: *the orbit of each planet is an ellipse with the sun at one focus.*

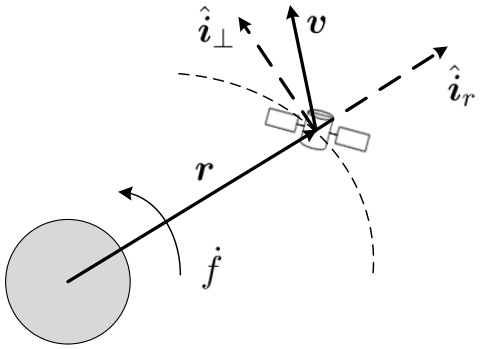

Figure 2.2: Definition of radial and perpendicular unit vectors.

can be written as $\boldsymbol{r} = r\hat{\boldsymbol{i}}_r$ and the velocity vector obtained by derivation,

$$\boldsymbol{v} = \frac{\mathrm{d}}{\mathrm{d}t}\boldsymbol{r} = \dot{r}\hat{\boldsymbol{i}}_r + r\frac{\mathrm{d}}{\mathrm{d}t}\hat{\boldsymbol{i}}_r$$

Time derivative of radial unit vector can be computed using satellite's angular velocity, that is directed along the unit vector $\hat{\boldsymbol{i}}_\theta = \hat{\boldsymbol{i}}_r \times \hat{\boldsymbol{i}}_\perp$. Therefore,

$$\frac{\mathrm{d}}{\mathrm{d}t}\hat{\boldsymbol{i}}_r = \dot{f}\hat{\boldsymbol{i}}_\theta \times \hat{\boldsymbol{i}}_r = \dot{f}\hat{\boldsymbol{i}}_\perp$$

and satellite's velocity can be rewritten as

$$\boldsymbol{v} = \dot{r}\hat{\boldsymbol{i}}_r + r\dot{f}\hat{\boldsymbol{i}}_\perp$$

Satellite's angular momentum is thus

$$\boldsymbol{h} = \boldsymbol{r} \times \boldsymbol{v} = r^2\dot{f}\hat{\boldsymbol{i}}_\theta$$

and true anomaly time derivative is given by

$$\dot{f} = \frac{h}{r^2} \tag{2.7}$$

Other important quantities are the orbital period and the mean motion. The *orbital*

period is the time taken for a satellite to make one complete orbit around the primary body and is given by,

$$T = 2\pi\sqrt{\frac{a^3}{\mu}}$$

Satellite's *mean motion* is the average angular speed in an elliptic orbit and is defined as

$$n \triangleq \frac{2\pi}{T} = \sqrt{\frac{\mu}{a^3}} \tag{2.8}$$

2.1.2 Orbital Elements

The position of a satellite can be described in different ways. The first and most simple solution is the use of a Cartesian coordinate system centred in the principal body center of mass, such as the *Earth-centred inertial coordinate frame* (ECI):

$$\{I\} = \left\{\hat{\boldsymbol{i}}_I, \hat{\boldsymbol{j}}_I, \hat{\boldsymbol{k}}_I\right\}$$

In this system, the unit vector $\hat{\boldsymbol{i}}_I$ points toward the first point of Aries[2], $\hat{\boldsymbol{k}}_I$ goes through the geographic North Pole and $\hat{\boldsymbol{j}}_I$ completes the reference frame lying in the equatorial plane. The adoption of a Cartesian reference frame allows the complete description of satellite's state by two $\mathbb{R}^3$ vectors: its position $\boldsymbol{r}$ and velocity $\boldsymbol{v}$.

However, visualization of satellite's orbit is difficult using such a type of coordinate system. Therefore, the orbit is usually described by means of six parameters shown in Figure 2.3, the *classical orbital elements*:

$$\boldsymbol{e} = \begin{bmatrix} a & e & i & \Omega & \omega & f \end{bmatrix}$$

The first five elements are constant in case of Keplerian motion and represent the shape, size and orientation of the orbit, whereas the sixth element locates the satel-

[2]For an observer on the Earth the Sun motion on the celestial sphere is the result of the day-night cycle and of its motion along the ecliptic. The Sun describes a circumference on the celestial sphere called *ecliptic* moving towards east with an average speed of $1\,^\circ$/d. The ecliptic plane intersects the equatorial plane in two points: the *first point of Aries* and the *first point of Libra*. The first one is occupied by the Sun during the vernal equinox, whereas the point of Libra is occupied at autumnal equinox

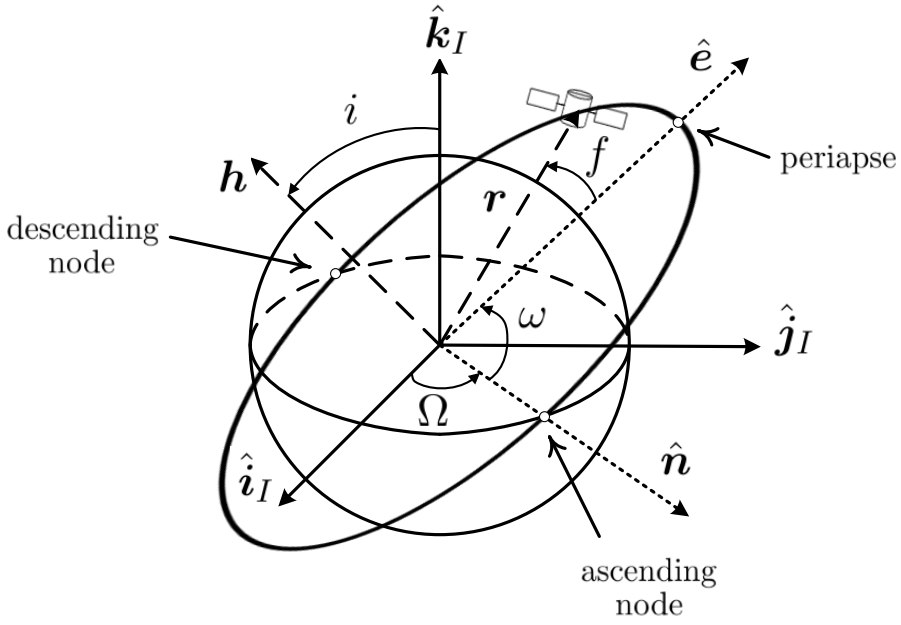

Figure 2.3: Classical orbital elements definition.

lite on the orbit.

Before giving a description of the orbital elements, some parameters and particular points must be introduced. In the general case, satellite's orbit intersects the equatorial plane in two points. In the *ascending node* the satellite crosses the equatorial planes south to north, whereas in the *descending node* the plane is crossed north to south. The line that passes through the ascending and the descending node is called *nodal line*. The unit vector $\hat{\boldsymbol{n}}$ has the same direction of the nodal line, it is centred in the primary focus and points the ascending node. It is defined as

$$\hat{\boldsymbol{n}} = \frac{\hat{\boldsymbol{k}}_I \times \boldsymbol{h}}{\left\| \hat{\boldsymbol{k}}_I \times \boldsymbol{h} \right\|}$$

The *eccentricity vector* $\boldsymbol{e}$ (the symbol must not be confused with the orbital elements vector defined above) lies on the line that connects the primary focus to the periapse and is defined by the following formula,

$$\boldsymbol{e} = \frac{1}{\mu}\left(\boldsymbol{v} \times \boldsymbol{h} - \mu \frac{\boldsymbol{r}}{r}\right) \tag{2.9}$$

The eccentricity unit vector is shown in Figure 2.3.

The classical orbital elements can now be described. Some of them were already introduced in Section 2.1.1.

- *Semi-major axis* a: describes the size of the ellipse;
- *Eccentricity* e: describes the shape of the ellipse;
- *Inclination* $i \in [0, \pi]$: the angle between the orbital and the equatorial planes;
- *Right ascension of the ascending node* $\Omega \in [0, 2\pi]$: the angle from vector $\hat{\boldsymbol{i}}_I$ to the nodal line $\hat{\boldsymbol{n}}$;
- *Argument of perigee* $\omega \in [0, 2\pi]$: the angle from the ascending node to the periapse (or *perigee*).
- *True anomaly* $f \in [0, 2\pi]$: the angle between satellite's current position and periapse.

However, this set of parameters is affected by a series of singularities. For example, in case of equatorial orbits, i.e. $i = 0$, Ω and ω are not defined (the equatorial plane coincides with the orbit plane). When the orbit is circular the eccentricity vector cannot be defined (the periapse is not defined). In these cases, other parameters are introduced (see for example [1], Chapter 3) or other set of orbital elements are used (such as the *equinoctial element set*, see [2], or the orbital elements that will be introduced in Section 2.2.5).

2.1.3 From Orbital Elements to $(\boldsymbol{r},\boldsymbol{v})$ and Vice Versa

The orbital elements introduced in the previous section can be computed using satellite's position and velocity vectors. In particular,

- the eccentricity norm e may be computed using Equation (2.9);
- using Equation (2.5) and Equation (2.6) the semi-major axis a is given by

$$p = a\left(1 - e^2\right) = \frac{h^2}{\mu} \quad \Longleftrightarrow \quad a = \frac{h^2}{\mu\left(1 - e^2\right)}$$

- inclination i can be computed using the dot product between $\hat{\boldsymbol{k}}_I$ and $\boldsymbol{h}$

$$\cos i = \frac{\hat{\boldsymbol{k}}_I \cdot \boldsymbol{h}}{h} \quad \Longleftrightarrow \quad i = \arccos\left(\frac{\hat{\boldsymbol{k}}_I \cdot \boldsymbol{h}}{h}\right)$$

- the same procedure can be followed for the right ascension of the ascending node Ω, remembering that, unlike inclination, $\Omega \in [0, 2\pi]$,

$$\cos\Omega = \hat{\boldsymbol{i}}_I \cdot \hat{\boldsymbol{n}} \quad \Longleftrightarrow \quad \Omega = \begin{cases} \arccos\left(\hat{\boldsymbol{i}}_I \cdot \hat{\boldsymbol{n}}\right), & \hat{\boldsymbol{n}} \cdot \hat{\boldsymbol{j}}_I > 0 \\ 2\pi - \arccos\left(\hat{\boldsymbol{i}}_I \cdot \hat{\boldsymbol{n}}\right), & \hat{\boldsymbol{n}} \cdot \hat{\boldsymbol{j}}_I < 0 \end{cases}$$

- the argument of perigee can be computed using unit vectors $\hat{\boldsymbol{e}}$ and $\hat{\boldsymbol{n}}$,

$$\cos\omega = \hat{\boldsymbol{n}} \cdot \hat{\boldsymbol{e}} \quad \Longleftrightarrow \quad \omega = \begin{cases} \arccos\left(\hat{\boldsymbol{n}} \cdot \hat{\boldsymbol{e}}\right), & \boldsymbol{e} \cdot \hat{\boldsymbol{k}}_I > 0 \\ 2\pi - \arccos\left(\hat{\boldsymbol{n}} \cdot \hat{\boldsymbol{e}}\right), & \boldsymbol{e} \cdot \hat{\boldsymbol{k}}_I < 0 \end{cases}$$

- finally, as for ω and Ω, the true anomaly can be computed as the angle between $\hat{\boldsymbol{e}}$ and the position unit vector $\hat{\boldsymbol{r}} = \boldsymbol{r}/r$.

$$\cos f = \hat{\boldsymbol{e}} \cdot \hat{\boldsymbol{r}} \quad \Longleftrightarrow \quad f = \begin{cases} \arccos\left(\hat{\boldsymbol{e}} \cdot \hat{\boldsymbol{r}}\right), & \boldsymbol{r} \cdot \boldsymbol{v} > 0 \\ 2\pi - \arccos\left(\hat{\boldsymbol{e}} \cdot \hat{\boldsymbol{r}}\right), & \boldsymbol{r} \cdot \boldsymbol{v} < 0 \end{cases}$$

The inverse transformation, from orbital elements to $(\boldsymbol{r}, \boldsymbol{v})$, needs the definition of a new coordinate systems, the *perifocal reference frame*,

$$\{P\} = \left\{\hat{\boldsymbol{P}}, \hat{\boldsymbol{W}}, \hat{\boldsymbol{Q}}\right\}$$

The perifocal coordinate system, shown in Figure 2.4, is centred in the primary focus. The unit vectors $\hat{\boldsymbol{P}}$ and $\hat{\boldsymbol{Q}}$ lies in the orbital plane with $\hat{\boldsymbol{P}}$ pointing to the periapse. $\hat{\boldsymbol{W}}$ has the same direction of the angular momentum vector $\boldsymbol{h}$ and $\hat{\boldsymbol{Q}}$ completes the coordinate system.

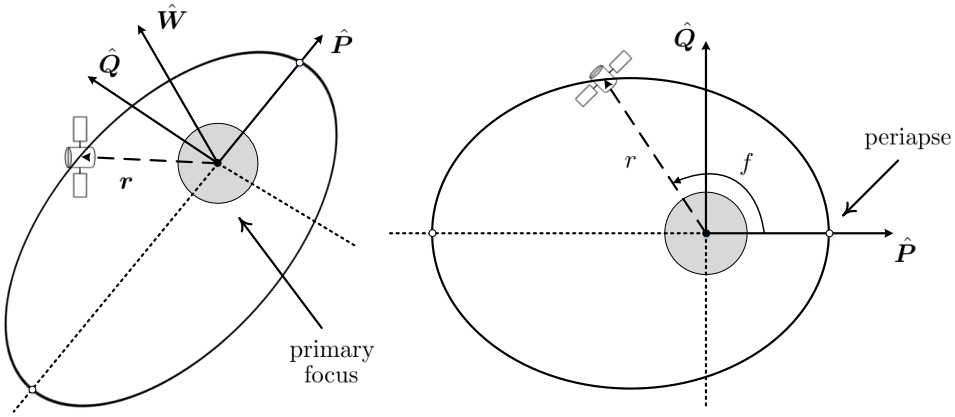

Figure 2.4: Perifocal reference frame.

The position $\boldsymbol{r}$ in the perifocal reference frame has the following expression,

$$\boldsymbol{r} = r\cos f\hat{\boldsymbol{P}} + r\sin f\hat{\boldsymbol{Q}} \tag{2.10}$$

Using Equation (2.4) and Equation (2.5), it is possible to express $\boldsymbol{r}$ as a function of the orbital elements.

$$\boldsymbol{r}^P = r\begin{bmatrix}\cos f\\ \sin f\\ 0\end{bmatrix} = \frac{a\left(1-e^2\right)}{1+e\cos f}\begin{bmatrix}\cos f\\ \sin f\\ 0\end{bmatrix}$$

In case of Keplerian motion the orbit does not change with time, thus the perifocal coordinate system is inertial and

$$\frac{\mathrm{d}}{\mathrm{d}t}\hat{\boldsymbol{P}} = \frac{\mathrm{d}}{\mathrm{d}t}\hat{\boldsymbol{Q}} = \boldsymbol{0}$$

Velocity $\boldsymbol{v}$ may be obtained by derivation of Equation (2.10),

$$\boldsymbol{v} = \frac{\mathrm{d}\boldsymbol{r}}{\mathrm{d}t} = \left(\dot{r}\cos f - r\dot{f}\sin f\right)\hat{\boldsymbol{P}} + \left(\dot{r}\sin f + r\dot{f}\cos f\right)\hat{\boldsymbol{Q}} \tag{2.11}$$

Time derivative of position norm can be computed as follows,

$$\dot{r} = \frac{\partial r}{\partial f}\dot{f} = \frac{pe\sin f}{(1+e\cos f)^2}\dot{f} = \frac{r\dot{f}e\sin f}{1+e\cos f} \tag{2.12}$$

and using Equation (2.6) and Equation (2.7), the expression of $\dot{r}$ as a function of the orbital parameters is given by

$$\dot{r} = \frac{r\dot{f}e\sin f}{1+e\cos f}\frac{r}{r} = \frac{\sqrt{\mu p}e\sin f}{r\,(1+e\cos f)} = \sqrt{\frac{\mu}{p}}e\sin f \tag{2.13}$$

Introducing Equation (2.13) in Equation (2.12) gives the expression for $r\dot{f}$,

$$r\dot{f} = \sqrt{\frac{\mu}{p}}\,(1+e\cos f) \tag{2.14}$$

Substituting Equations (2.13)-(2.14) in Equation (2.11) gives the expression of $\boldsymbol{v}$ in the perifocal frame,

$$\boldsymbol{v}^P = \sqrt{\frac{\mu}{p}}\begin{bmatrix} -\sin f \\ e+\cos f \\ 0 \end{bmatrix}$$

Finally, the expression of the position and velocity vectors in the ECI frame can be obtained using the coordinate change matrix $\boldsymbol{C}_P^I(i,\Omega,\omega) : \{P\} \to \{I\}$,

$$\boldsymbol{r}^I = \boldsymbol{C}_P^I(i,\Omega,\omega)\boldsymbol{r}^P, \qquad \boldsymbol{v}^I = \boldsymbol{C}_P^I(i,\Omega,\omega)\boldsymbol{v}^P$$

Its transpose, $\boldsymbol{C}_I^P(i,\Omega,\omega) : \{I\} \to \{P\}$ may be computed as composition of elementary rotation,

$$\boldsymbol{C}_I^P(i,\Omega,\omega) = \boldsymbol{C}_z(\omega)\boldsymbol{C}_x(i)\boldsymbol{C}_z(\Omega)$$

where the elementary rotation matrices are defined as follows,

$$\boldsymbol{C}_x(\alpha) = \begin{bmatrix} 1 & 0 & 0 \\ 0 & \cos\alpha & \sin\alpha \\ 0 & -\sin\alpha & \cos\alpha \end{bmatrix}, \quad \boldsymbol{C}_y(\alpha) = \begin{bmatrix} \cos\alpha & 0 & -\sin\alpha \\ 0 & 1 & 0 \\ \sin\alpha & 0 & \cos\alpha \end{bmatrix}$$

$$\boldsymbol{C}_z(\alpha) = \begin{bmatrix} \cos\alpha & \sin\alpha & 0 \\ -\sin\alpha & \cos\alpha & 0 \\ 0 & 0 & 1 \end{bmatrix}$$

2.1.4 Space Perturbations

In the previous sections the gravitational attraction between two point masses was considered and a basic mathematical model for satellite motion description was developed. However, during its motion in space a satellite is subjected not only to the gravitational force, but to many other forces that might change its orbit. The forces not considered in the Keplerian motion model are usually referred to as *perturbation forces*.

Perturbations are usually quantified in terms of accelerations, in order to write Equation (2.2) as

$$\ddot{\boldsymbol{r}} = -\frac{\mu}{r^3}\boldsymbol{r} + \boldsymbol{a}_p \tag{2.15}$$

introducing the perturbation acceleration $\boldsymbol{a}_p$. Numerical integration must be performed in order to compute satellite's trajectory, since closed form solutions for the considered perturbations often do not exist.

In this section, two of the most important perturbations for *lower Earth orbits* (LEO), orbits with altitude lower than 800 km and semi-major axis lower than 7178 km, are presented: atmospheric drag and J_2 perturbation.

Atmospheric Drag

In case of low orbits, which altitude is lower than 600 km, Earth's residual atmosphere produces a drag effect on the satellite. Exact quantification of the atmo-

spheric drag is difficult for different reasons. Atmosphere characteristics at high altitudes are extremely variable and change according to solar and geomagnetic activity. Moreover, drag magnitude and direction depends on satellites shape and orientation with respect to the surrounding atmosphere.

A simplified model for preliminary mission study is the following,

$$\boldsymbol{a}_{\text{Atm}} = -\frac{\rho v_r}{2c_b}\boldsymbol{v}_r \tag{2.16}$$

where $\boldsymbol{v}_r$ is the relative velocity of the satellite with respect to the atmosphere. An approximation is

$$\boldsymbol{v}_r = \boldsymbol{v} - \boldsymbol{v}_{\text{Atm}} \approx \boldsymbol{v} - \boldsymbol{\omega}_\oplus \times \boldsymbol{r}$$

where $\boldsymbol{\omega}_\oplus$ is the Earth angular velocity vector. The average Earth angular velocity is usually adopted: $\overline{\boldsymbol{\omega}}^I_\oplus = 7.292115 \times 10^{-5}\hat{\boldsymbol{k}}_I$ rad/s. Satellite's shape and weight is considered by the parameter c_b, the *ballistic coefficient*, expressed in kg/m^2 and defined as

$$c_b \triangleq \frac{m}{C_D A}$$

where m is the satellite mass in kg, C_D is the *drag coefficient* and A is the satellite's *transversal section average area* measured in m^2.

The term ρ is the *local atmosphere density*, measured in kg/m^3. This term is the most difficult to estimate, since the high variability of atmosphere. A model usually employed for preliminary mission study is the *atmosphere exponential model*. Denoting with h satellite's altitude, the local atmosphere density is given by

$$\rho = \rho_0 \exp\left(-\frac{h - h_0}{H}\right)$$

where ρ_0 and h_0 are two reference values, respectively for atmosphere density and altitude, and H is a scale factor. Their values can be found in [1]. Local atmosphere density variation as a function of the altitude is shown in Figure 2.5.

In Section 2.2.4 the time derivative of $\boldsymbol{a}_{\text{Atm}}$ will be needed. Equation (2.16) can

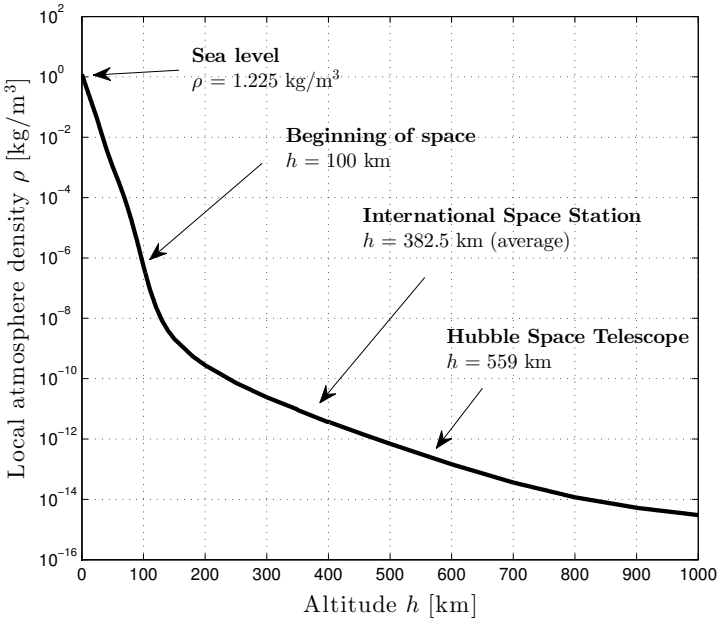

Figure 2.5: Atmosphere exponential model, density.

be written as

$$\boldsymbol{a}_{\text{Atm}} = K_{\text{Atm}} v_r \boldsymbol{v}_r$$

where $K_{\text{Atm}} = -\frac{\rho}{2c_b}$, and its time derivative is

$$\frac{\mathrm{d}}{\mathrm{d}t}\boldsymbol{a}_{\text{Atm}} = K_{\text{Atm}} \left(\dot{v}_r \boldsymbol{v}_r + v_r \frac{\mathrm{d}}{\mathrm{d}t}\boldsymbol{v}_r \right)$$

Using the average Earth angular velocity $\overline{\boldsymbol{\omega}}_{\oplus}$, relative acceleration can be computed as follows,

$$\frac{\mathrm{d}}{\mathrm{d}t}\boldsymbol{v}_r = \frac{\mathrm{d}}{\mathrm{d}t}\boldsymbol{v} - \frac{\mathrm{d}}{\mathrm{d}t}\overline{\boldsymbol{\omega}}_{\oplus} \times \boldsymbol{r} - \overline{\boldsymbol{\omega}}_{\oplus} \times \frac{\mathrm{d}}{\mathrm{d}t}\boldsymbol{r} = \frac{\mathrm{d}}{\mathrm{d}t}\boldsymbol{v} - \overline{\boldsymbol{\omega}}_{\oplus} \times \boldsymbol{v}$$

since $\frac{\mathrm{d}}{\mathrm{d}t}\overline{\boldsymbol{\omega}}_{\oplus} = \boldsymbol{0}$. It should be noted that satellite's acceleration is needed for time derivative computation of atmospheric drag acceleration.

In order to compute relative velocity norm time derivative, the following result must be introduced. Time derivative of a general vector's norm, e.g. $\boldsymbol{w} \in \mathbb{R}^3$ with components w_x, w_y and w_z in a given reference system, can be computed using the

following relationship,

$$\dot{w} = \frac{\mathrm{d}}{\mathrm{d}t}\sqrt{w_x^2 + w_y^2 + w_z^2} = \frac{1}{w}\left(\boldsymbol{w} \cdot \frac{\mathrm{d}}{\mathrm{d}t}\boldsymbol{w}\right) \tag{2.17}$$

Note that this results is independent from the chosen coordinate system, since the norm is a scalar. Thus, vector $\boldsymbol{w}$ can be derived in any type of reference frame.

Using Equation (2.17), relative velocity norm time derivative is given by

$$\dot{v}_r = \frac{1}{v_r}\left(\boldsymbol{v}_r \cdot \frac{\mathrm{d}}{\mathrm{d}t}\boldsymbol{v}_r\right)$$

and drag atmosphere perturbation acceleration can be finally computed.

J_2 Perturbation

An important source of perturbations for satellites in orbit around the Earth is caused by the non-spherical mass distribution of the planet and its non-uniform density. The equipotential surfaces of Earth's gravitational field are not spherical, but can be approximated as ellipsoids.

This approximation allows the mathematical description of the gravitational potential associated to the Earth. In particular, modelling Earth as an ellipsoid with equatorial radius $R_{\mathrm{eq}} = 6378.136\,\mathrm{km}$, approximately twenty kilometres greater than polar radius, its gravitational potential U_g is given by,

$$U_g = \frac{GM}{r}\left(1 - \sum_{n=2}^{+\infty} J_n \left(\frac{R_{\mathrm{eq}}}{r}\right)^n P_n(\sin\delta)\right)$$

The distance of a point P from the body center of mass is denoted with r, M is the Earth mass, δ is the declination (the angle between the equatorial plane and the vector that describes the position of P with respect to the Earth center of mass), J_n is the *zonal harmonic* of order n and $P_n(x)$ is the Legendre polynomial of order n defined as

$$P_n(x) = \frac{1}{2^n n!}\frac{\mathrm{d}^n}{\mathrm{d}x^n}\left(\left(x^2 - 1\right)^n\right)$$

Table 2.1: Zonal harmonics of Earth gravitational field.

J_2	1.0826×10^{-3}	J_8	-2.0480×10^{-7}
J_3	-2.5327×10^{-6}	J_9	-1.2062×10^{-7}
J_4	-1.6196×10^{-6}	J_{10}	-2.4115×10^{-7}
J_5	-2.2730×10^{-7}	J_{11}	2.4440×10^{-7}
J_6	5.4068×10^{-7}	J_{12}	-1.8863×10^{-7}
J_7	-3.5236×10^{-7}	J_{13}	-2.1979×10^{-7}

As can be seen in Table 2.1, J_2 is the predominant zonal harmonic, thus for a preliminary analysis it can be considered the following potential,

$$U_g\Big|_{n=2} = \frac{\mu}{r}\left(1 - J_2\left(\frac{R_{\text{eq}}}{r}\right)^2\left(\frac{3}{2}\sin^2\delta - \frac{1}{2}\right)\right)$$

Noting that μ/r is the gravitational potential of a spherical body, J_2 potential can be isolated,

$$U_{J_2} = -\frac{\mu}{r}J_2\left(\frac{R_{\text{eq}}}{r}\right)^2\left(\frac{3}{2}\sin^2\delta - \frac{1}{2}\right)$$

and integrated in order to obtain the perturbation acceleration,

$$\boldsymbol{a}_{J_2} = \nabla U_{J_2}$$

Denoting with $\boldsymbol{r}^I = [r_x, r_y, r_z]^T$ the spacecraft position in the ECI frame, J_2 perturbation acceleration is given by

$$\boldsymbol{a}^I_{J_2} = -\frac{3}{2}J_2\left(\frac{\mu}{r^2}\right)\left(\frac{R_{\text{eq}}}{r}\right)^2\begin{bmatrix}\left(1 - 5\left(\frac{r_z}{r}\right)^2\right)\frac{r_x}{r}\\ \left(1 - 5\left(\frac{r_z}{r}\right)^2\right)\frac{r_y}{r}\\ \left(3 - 5\left(\frac{r_z}{r}\right)^2\right)\frac{r_z}{r}\end{bmatrix} \tag{2.18}$$

Again, in Section 2.2.4 the expression of the J_2 perturbation acceleration time

derivative will be required. Equation (2.18) can be written as

$$\boldsymbol{a}^I_{J_2} = \frac{K_{J_2}}{r^5}\begin{bmatrix} r_x \\ r_y \\ 3r_z \end{bmatrix} - 5\frac{K_{J_2}}{r^7}\begin{bmatrix} r_x r_z^2 \\ r_y r_z^2 \\ r_z^3 \end{bmatrix}$$

where the constant $K_{J_2} = -\frac{3}{2}J_2\mu R^2_{\text{eq}}$ is introduced. Derivation with respect to time of the previous equation gives

$$\frac{\mathrm{d}}{\mathrm{d}t}\boldsymbol{a}^I_{J_2} = \frac{K_{J_2}}{r^5}\left(\begin{bmatrix} \dot{r}_x \\ \dot{r}_y \\ 3\dot{r}_z \end{bmatrix} - \frac{5\dot{r}}{r}\begin{bmatrix} r_x \\ r_y \\ 3r_z \end{bmatrix} - \frac{5}{r^2}\begin{bmatrix} r_z^2\dot{r}_x + 2r_x r_z \dot{r}_z \\ r_z^2\dot{r}_y + 2r_y r_z \dot{r}_z \\ 3r_z^2\dot{r}_z \end{bmatrix} + \frac{35\dot{r}}{r^3}\begin{bmatrix} r_x r_z^2 \\ r_y r_z^2 \\ r_z^3 \end{bmatrix}\right)$$

Gauss Variational Equations

Gauss variational equations describe the orbital elements variation in presence of perturbations. The equation set needs the introduction of a new coordinate system, the *RTN reference frame*. The frame will be denoted with

$$\{R\} = \left\{\hat{\boldsymbol{\imath}}_R, \hat{\boldsymbol{\imath}}_T, \hat{\boldsymbol{\imath}}_N\right\}$$

with unit vectors defined as

$$\hat{\boldsymbol{\imath}}_R = \boldsymbol{r}/r, \quad \hat{\boldsymbol{\imath}}_N = \boldsymbol{h}/h, \quad \hat{\boldsymbol{\imath}}_T = \hat{\boldsymbol{\imath}}_N \times \hat{\boldsymbol{\imath}}_R$$

and its origin is in the satellite's center of mass. The acronym RTN comes from unit vectors definition: *radial*, *transversal* and *normal*. In order to express the perturbation acceleration in the RTN frame, the coordinate change matrix from ECI to RTN, $\boldsymbol{C}^R_I(\boldsymbol{r}, \boldsymbol{v}) : \{I\} \to \{R\}$ must be introduced,

$$\boldsymbol{C}^R_I(\boldsymbol{r}, \boldsymbol{v}) = \left[\begin{array}{c|c|c} \hat{\boldsymbol{\imath}}^I_R & \hat{\boldsymbol{\imath}}^I_T & \hat{\boldsymbol{\imath}}^I_N \end{array}\right]$$

Writing the perturbation acceleration in this frame,

$$\boldsymbol{a}_p^R = \begin{bmatrix} a_{p_R} \\ a_{p_T} \\ a_{p_N} \end{bmatrix} = \boldsymbol{C}_I^R(\boldsymbol{r}, \boldsymbol{v})\boldsymbol{a}_p^I$$

the orbital elements change according to the following equations.

$$\begin{aligned}
\frac{\mathrm{d}a}{\mathrm{d}t} &= \frac{2a^2}{h}\left(e\sin f\, a_{p_R} + a_{p_T}\right) \\
\frac{\mathrm{d}e}{\mathrm{d}t} &= \frac{1}{h}\left(p\sin f\, a_{p_R} + \left((p+r)\cos f + re\right) a_{p_T}\right) \\
\frac{\mathrm{d}i}{\mathrm{d}t} &= \frac{r\cos\theta}{h} a_{p_N} \\
\frac{\mathrm{d}\Omega}{\mathrm{d}t} &= \frac{r\sin\theta}{h\sin i} a_{p_N} \\
\frac{\mathrm{d}\omega}{\mathrm{d}t} &= -\frac{p}{eh}\cos f a_{p_R} + \frac{p+r}{eh}\sin f\, a_{p_T} - \frac{r\sin\theta\cos i}{h\sin i} a_{p_N} \\
\frac{\mathrm{d}f}{\mathrm{d}t} &= \frac{h}{r^2} + \frac{1}{eh}\left(p\cos f\, a_{p_R} - (p+r)\sin f\, a_{p_T}\right)
\end{aligned}$$

In the previous equations a new orbital element, the *true latitude* $\theta = \omega + f$, was introduced.

2.1.5 Continuous-Thrust Propulsion

In presence of propulsion, satellite's mass changes according to the burnt propellant. Hence, a mathematical model for propulsion is needed in order to compute mass variation during maneuvering.

Introducing the propulsion thrust force $\boldsymbol{T}$, satellite's equation of motion becomes

$$\frac{\mathrm{d}^2}{\mathrm{d}t^2}\boldsymbol{r} = -\frac{\mu}{r^3}\boldsymbol{r} + \frac{\boldsymbol{T}}{m}$$

where now the satellite's mass m is a time varying parameter. A simplified model for thrust magnitude is given by the following formula,

$$T = g_0 I_{\mathrm{sp}} \dot{m}_{\mathrm{prop}}$$

Table 2.2: Performance for some classes of engines.

Technology	I_{sp} [s]	T [N]
Cold gas	60 - 250	0.1 - 50
Chemical	140 - 350	0.1 - 12 000 000
Nuclear	800 - 6000	up to 12 000 000
Electrical	500 - 10 000	0.0001 - 20

where it was introduced the *specific impulse* I_{sp}, g_0 is the gravity acceleration at sea level (for Earth, $g_0 = 9.8066\,\text{m/s}^2$) and $\dot{m}_{\text{prop}}$ is propellent mass flow rate.

The specific impulse is measured in s and cahnge according to the engine technology (typical values are given in Table 2.2, adapted from [1]).

If the propellent consumption is the only cause of mass variation, then satellite's mass changes according to

$$\frac{\mathrm{d}m}{\mathrm{d}t} = -\dot{m}_{\text{prop}} = -\frac{T}{g_0 I_{\text{sp}}}$$

During the development of a control law, the control vector $\boldsymbol{u}$ can be either the thrust requested to the propulsion system, $\boldsymbol{u} = \boldsymbol{T}$, or the acceleration that must be imparted to the satellite, $\boldsymbol{u} = \boldsymbol{T}/m$.

2.2 Relative Motion in Space

Whenever two object must meet in space (e.g. a service vehicle headed to the International Space Station or a spacecraft deployed to repair a satellite) or two or more satellites must keep a formation, a proper mathematical model of the relative motion describing the relative position and velocity of the two bodies is needed.

Two different representations can be used to model the relative motion dynamic. The Cartesian representation is one of the most used, since it allows the direct use of sensors measurements of relative position and velocity and gives quick information about the position of the incoming vehicle. Starting from the most general vectorial expression, different sets of equations can be developed that may take or not in

account perturbations.

Orbital elements introduced in Section 2.1.2 can be used too. In particular, the difference between the orbit elements of the two objects is a measure of the error, that must be driven to zero by a proper control law.

In this section a brief introduction to both the representations is proposed. In the following, the target spacecraft will be denoted with the term *chief*, whereas the spacecraft that must chase or follow the chief will be referred to as the *deputy* and its parameters will be differed from chief's ones using the subscript d.

2.2.1 General Cartesian Expression of Relative Motion

The Cartesian formulation of the relative equations of motion is developed in the *local-vertical local-horizontal frame* (LVLH), also known as *Hill frame*:

$$\{L\} = \left\{\hat{\boldsymbol{i}}, \hat{\boldsymbol{j}}, \hat{\boldsymbol{k}}\right\}$$

The origin of the LVLH reference system is the chief's center of mass and its unit vectors are defined as follows (Figure 2.6).

$$\hat{\boldsymbol{i}} = \boldsymbol{r}/r, \qquad \hat{\boldsymbol{k}} = \boldsymbol{h}/h, \qquad \hat{\boldsymbol{j}} = \hat{\boldsymbol{k}} \times \hat{\boldsymbol{i}}$$

Thus, the LVLH frame rotates as the chief rotates about the primary body and consequently it is a non-inertial frame. The deputy motion in this frame is divided in two components: the *in-plane motion*, along $\hat{\boldsymbol{i}}$ and $\hat{\boldsymbol{j}}$, and the *out-of-plane motion*, along $\hat{\boldsymbol{k}}$.

Let $\boldsymbol{\rho}$ and $\dot{\boldsymbol{\rho}}$ denote, respectively, deputy's relative position and velocity vectors with respect to the chief,

$$\boldsymbol{\rho} = x\hat{\boldsymbol{i}} + y\hat{\boldsymbol{j}} + z\hat{\boldsymbol{k}}, \qquad \dot{\boldsymbol{\rho}} = \dot{x}\hat{\boldsymbol{i}} + \dot{y}\hat{\boldsymbol{j}} + \dot{z}\hat{\boldsymbol{k}}$$

and $\boldsymbol{\omega}$ and $\dot{\boldsymbol{\omega}}$ denote the angular velocity and acceleration of the LVLH frame with

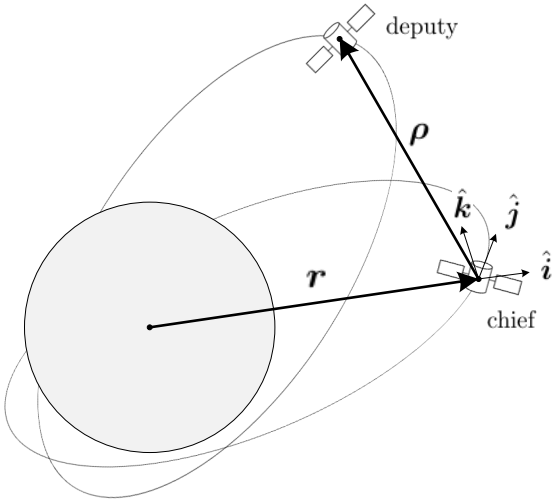

Figure 2.6: Local-vertical local-horizon frame.

respect to the ECI frame,

$$\boldsymbol{\omega} = \omega_x \hat{\boldsymbol{i}} + \omega_y \hat{\boldsymbol{j}} + \omega_z \hat{\boldsymbol{k}}, \qquad \dot{\boldsymbol{\omega}} = \dot{\omega}_x \hat{\boldsymbol{i}} + \dot{\omega}_y \hat{\boldsymbol{j}} + \dot{\omega}_z \hat{\boldsymbol{k}}$$

where the dot operator indicates the derivation with respect to time in the moving frame LVLH.

The absolute position of the deputy expressed in the LVLH frame is then

$$\boldsymbol{r}_d = \boldsymbol{r} + \boldsymbol{\rho} = (r + x)\,\hat{\boldsymbol{i}} + y\hat{\boldsymbol{j}} + z\hat{\boldsymbol{k}} \tag{2.20}$$

and the distance from the chief is given by

$$r_d = \sqrt{(r + x)^2 + y^2 + z^2}$$

Deputy's absolute velocity can be obtained deriving with respect to time Equation (2.20),

$$\frac{\mathrm{d}}{\mathrm{d}t}\boldsymbol{r}_d = \frac{\mathrm{d}}{\mathrm{d}t}\boldsymbol{r} + \frac{\mathrm{d}}{\mathrm{d}t}\boldsymbol{\rho} = \frac{\mathrm{d}}{\mathrm{d}t}\boldsymbol{r} + \dot{\boldsymbol{\rho}} + \boldsymbol{\omega} \times \boldsymbol{\rho} \tag{2.21}$$

The derivation with respect to time in the inertial frame is denoted with the operator $\frac{\mathrm{d}}{\mathrm{d}t}$. Further derivation of Equation (2.21) leads to the deputy's vectorial equation

of motion.

$$\begin{aligned}\frac{\mathrm{d}^2}{\mathrm{d}t^2}\boldsymbol{r}_d &= \frac{\mathrm{d}^2}{\mathrm{d}t^2}\boldsymbol{r} + \frac{\mathrm{d}}{\mathrm{d}t}\left(\dot{\boldsymbol{\rho}} + \boldsymbol{\omega}\times\boldsymbol{\rho}\right)\\ &= \frac{\mathrm{d}^2}{\mathrm{d}t^2}\boldsymbol{r} + \frac{\mathrm{d}}{\mathrm{d}t}\dot{\boldsymbol{\rho}} + \frac{\mathrm{d}}{\mathrm{d}t}\boldsymbol{\omega}\times\boldsymbol{\rho} + \boldsymbol{\omega}\times\frac{\mathrm{d}}{\mathrm{d}t}\boldsymbol{\rho}\\ &= \frac{\mathrm{d}^2}{\mathrm{d}t^2}\boldsymbol{r} + \ddot{\boldsymbol{\rho}} + \boldsymbol{\omega}\times\dot{\boldsymbol{\rho}} + \dot{\boldsymbol{\omega}}\times\boldsymbol{\rho} + \boldsymbol{\omega}\times\left(\dot{\boldsymbol{\rho}} + \boldsymbol{\omega}\times\boldsymbol{\rho}\right)\\ &= \frac{\mathrm{d}^2}{\mathrm{d}t^2}\boldsymbol{r} + \ddot{\boldsymbol{\rho}} + 2\boldsymbol{\omega}\times\dot{\boldsymbol{\rho}} + \dot{\boldsymbol{\omega}}\times\boldsymbol{\rho} + \boldsymbol{\omega}\times\left(\boldsymbol{\omega}\times\boldsymbol{\rho}\right)\end{aligned}$$

Introducing deputy's and chief's equations of perturbed motion using Equation (2.15),

$$\frac{\mathrm{d}^2}{\mathrm{d}t^2}\boldsymbol{r}_d = -\frac{\mu}{r_d^3}\boldsymbol{r}_d + \boldsymbol{a}_{p,d} + \boldsymbol{u}, \qquad \frac{\mathrm{d}^2}{\mathrm{d}t^2}\boldsymbol{r} = -\frac{\mu}{r^3}\boldsymbol{r} + \boldsymbol{a}_{p,c}$$

where $\boldsymbol{a}_{p,c}$ and $\boldsymbol{a}_{p,d}$ are the perturbation accelerations exerted respectively on chief and deputy and $\boldsymbol{u}$ is the control vector, writing the position as $\boldsymbol{r} = r\hat{\boldsymbol{i}}$ and defining the differential perturbation acceleration,

$$\Delta\boldsymbol{a}_p \triangleq \boldsymbol{a}_{p,d} - \boldsymbol{a}_{p,c} = \Delta a_{p_x}\hat{\boldsymbol{i}} + \Delta a_{p_y}\hat{\boldsymbol{j}} + \Delta a_{p_z}\hat{\boldsymbol{k}}$$

the general vectorial expression for the relative motion is given by

$$\ddot{\boldsymbol{\rho}} + 2\boldsymbol{\omega}\times\dot{\boldsymbol{\rho}} + \dot{\boldsymbol{\omega}}\times\boldsymbol{\rho} + \boldsymbol{\omega}\times\left(\boldsymbol{\omega}\times\boldsymbol{\rho}\right) - \frac{\mu}{r^3}\boldsymbol{r} + \frac{\mu}{r_d^3}\left(\boldsymbol{r}+\boldsymbol{\rho}\right) = \Delta\boldsymbol{a}_p + \boldsymbol{u} \tag{2.22}$$

This equation is the staring point for the derivation of the nonlinear equations of relative motion in the unpertubed and perturbed cases.

The components of vectors $\boldsymbol{\rho}$ and $\dot{\boldsymbol{\rho}}$ can be also computed using chief's and deputy's absolute position and velocity vectors expressed in the inertial frame, as shown in [6].

Let $\delta\boldsymbol{r}$ and $\delta\boldsymbol{v}$ be the inertial relative displacement and velocity, defined as

$$\delta\boldsymbol{r} = \boldsymbol{r}_d - \boldsymbol{r}, \qquad \delta\boldsymbol{v} = \boldsymbol{v}_d - \boldsymbol{v}$$

Then, the components of the relative position and velocity vectors can be computed

using the following equations set.

$$
\begin{aligned}
x =& \frac{\delta \boldsymbol{r}^T \boldsymbol{r}}{r} \\
y =& \frac{\delta \boldsymbol{r}^T (\boldsymbol{h} \times \boldsymbol{r})}{\|\boldsymbol{h} \times \boldsymbol{r}\|} \\
z =& \frac{\delta \boldsymbol{r}^T \boldsymbol{h}}{h} \\
\dot{x} =& \frac{\delta \boldsymbol{v}^T \boldsymbol{r} + \delta \boldsymbol{r}^T \boldsymbol{v}}{r} - \frac{\left(\delta \boldsymbol{r}^T \boldsymbol{r}\right)\left(\delta \boldsymbol{r}^T \boldsymbol{v}\right)}{r^3} \\
\dot{y} =& \frac{\delta \boldsymbol{v}^T (\boldsymbol{h} \times \boldsymbol{r}) + \delta \boldsymbol{r}^T \left(\dot{\boldsymbol{h}} \times \boldsymbol{r} + \boldsymbol{h} \times \boldsymbol{v}\right)}{\|\boldsymbol{h} \times \boldsymbol{r}\|} \\
& - \frac{\delta \boldsymbol{r}^T (\boldsymbol{h} \times \boldsymbol{r}) (\boldsymbol{h} \times \boldsymbol{r})^T \left(\dot{\boldsymbol{h}} \times \boldsymbol{r} + \boldsymbol{h} \times \boldsymbol{v}\right)}{\|\boldsymbol{h} \times \boldsymbol{r}\|^3} \\
\dot{z} =& \frac{\delta \boldsymbol{v}^T \boldsymbol{h} + \delta \boldsymbol{r}^T \dot{\boldsymbol{h}}}{h} - \frac{\left(\delta \boldsymbol{r}^T \boldsymbol{h}\right)\left(\boldsymbol{h}^T \dot{\boldsymbol{h}}\right)}{h^3}
\end{aligned}
$$

These equations allow the simulation of relative motion in presence of perturbation, avoiding the integration of Equation (2.22). Deputy and chief motion can be simulated separately and then relative motion can be computed using Equations (2.23).

2.2.2 Nonlinear Equations of Relative Motion

In absence of perturbation, i.e. $\Delta \boldsymbol{a}_p = \boldsymbol{0}$, the angular velocity $\boldsymbol{\omega}$ becomes

$$\boldsymbol{\omega} = \dot{f}\hat{\boldsymbol{k}} = \frac{h}{r^2}\hat{\boldsymbol{k}}$$

and recalling that the angular momentum $\boldsymbol{h}$ is constant in case of Keplerian motion, i.e. $\dot{h} = 0$, the angular acceleration is given by,

$$\dot{\boldsymbol{\omega}} = -\frac{2h\dot{r}}{r^3}\hat{\boldsymbol{k}} = -2\dot{f}\frac{\dot{r}}{r}\hat{\boldsymbol{k}}$$

Thus, the terms appearing in Equation (2.22) become

$$2\boldsymbol{\omega} \times \dot{\boldsymbol{\rho}} = -2\dot{f}\dot{y}\hat{\boldsymbol{\imath}} + 2\dot{f}\dot{x}\hat{\boldsymbol{\jmath}}$$

$$\dot{\boldsymbol{\omega}} \times \boldsymbol{\rho} = 2\dot{f}\frac{\dot{r}}{r}y\hat{\boldsymbol{i}} - 2\dot{f}\frac{\dot{r}}{r}x\hat{\boldsymbol{j}}$$
$$\boldsymbol{\omega} \times (\boldsymbol{\omega} \times \boldsymbol{\rho}) = -\dot{f}^2 x\hat{\boldsymbol{i}} - \dot{f}^2 y\hat{\boldsymbol{j}}$$

The *nonlinear equations of relative motion in the unperturbed case* (in the following denoted with the acronym NERM) are obtained substituting the terms in Equations (2.24) into Equation (2.22) and writing the motion along the LVLH unit vectors separately.

$$\ddot{x} = 2\dot{f}\left(\dot{y} - \frac{\dot{r}}{r}y\right) + \dot{f}^2 x + \frac{\mu}{r^2} - \frac{\mu}{r_d^3}(r + x) + u_x \tag{2.25a}$$
$$\ddot{y} = -2\dot{f}\left(\dot{x} - \frac{\dot{r}}{r}x\right) + \dot{f}^2 y - \frac{\mu}{r_d^3}y + u_y$$
$$\ddot{z} = -\frac{\mu}{r_d^3}z + u_z$$

This set of equations is a nonlinear time-varying system with state

$$\boldsymbol{x} = \begin{bmatrix} x & y & z & \dot{x} & \dot{y} & \dot{z} \end{bmatrix}^T$$

and time-varying coefficients r, $\dot{r}$, $\dot{f}$. The components of the control vector $\boldsymbol{u}$ influence the time derivative of the relative position vector, ensuring the full controllability of the system. This system is affine in the control, as it will be shown in Section 6.1.1.

2.2.3 Linear Equations of Relative Motion

The nonlinear equations of motion developed in the previous section can be linearized if it is assumed that the distance between the chief and the deputy is sufficiently small with respect to the distance of the two satellites from the primary body's center of mass, i.e. $\rho \ll r$ and $\rho \ll r_d$. Assuming that, the norm r_d may be

written as follows

$$\begin{aligned} r_d &= \sqrt{(r+x)^2 + y^2 + z^2} \\ &= r\sqrt{1 + \frac{2x}{r} + \frac{x^2+y^2+z^2}{r^2}} \\ &\approx r\sqrt{1 + \frac{2x}{r}} \\ &\approx r\left(1 + \frac{x}{r}\right) \end{aligned}$$

where the first order approximation $(1+\alpha)^n \approx 1+n\alpha$, valid when $\alpha \ll 1$, was introduced in the last step. The previous result is used to simplify deputy's gravitational acceleration $\frac{\mu}{r_d^3}\boldsymbol{r}_d$ appearing in Equations (2.25):

$$\begin{aligned} \frac{\mu}{r_d^3}\boldsymbol{r}_d &= \frac{\mu}{r_d^3}\left((r+x)\hat{\boldsymbol{i}} + y\hat{\boldsymbol{j}} + z\hat{\boldsymbol{k}}\right) \\ &\approx \frac{\mu}{r^3}\left(1 - \frac{3x}{r}\right)\left((r+x)\hat{\boldsymbol{i}} + y\hat{\boldsymbol{j}} + z\hat{\boldsymbol{k}}\right) \\ &\approx \frac{\mu}{r^3}\left((r-2x)\hat{\boldsymbol{i}} + y\hat{\boldsymbol{j}} + z\hat{\boldsymbol{k}}\right) \\ &= \left(\frac{\mu}{r^2} - 2\frac{\mu}{r^3}x\right)\hat{\boldsymbol{i}} + \frac{\mu}{r^3}y\hat{\boldsymbol{j}} + \frac{\mu}{r^3}z\hat{\boldsymbol{k}} \\ &= \left(\frac{\mu}{r^2} - 2\frac{r}{p}\dot{f}^2x\right)\hat{\boldsymbol{i}} + \frac{r}{p}\dot{f}^2y\hat{\boldsymbol{j}} + \frac{r}{p}\dot{f}^2\hat{\boldsymbol{k}} \end{aligned} \tag{2.26}$$

In the last step, Equation (2.6) was introduced to rewrite the gravitational parameter as $\mu = \frac{h^2}{p} = \frac{r^4\dot{f}^2}{p}$.

The *linear equations of relative motion in the unperturbed case* (LERM) can be obtained introducing Equation (2.26) into Equations (2.25),

$$\begin{aligned} \ddot{x} &= \dot{f}^2\left(1 + 2\frac{r}{p}\right)x + 2\dot{f}\left(\dot{y} - \frac{\dot{r}}{r}y\right) + u_x \\ \ddot{y} &= -2\dot{f}\left(\dot{x} - \frac{\dot{r}}{r}x\right) + \dot{f}^2\left(1 - \frac{r}{p}\right)y + u_y \\ \ddot{z} &= -\frac{r}{p}\dot{f}^2z + u_z \end{aligned}$$

With these approximations the system becomes linear time-varying.

A remarkable simplification of this mathematical model can be obtained assum-

ing that the chief's orbit is circular. In this case $\dot{r} = 0$, $p = r$ and $\dot{f}$ is constant. Rewriting $\dot{f}$ using Equation (2.6) and Equation (2.8),

$$\dot{f} = \frac{h}{r^2} = \frac{\sqrt{\mu p}}{p^2} = \sqrt{\frac{\mu}{p^3}} = \sqrt{\frac{\mu}{a^3}} = n$$

the *Hill - Clohessy - Wiltshire* equations set (HCW) can be obtained,

$$\ddot{x} = 3n^2 x + 2n\dot{y} + u_x$$

$$\ddot{y} = -2n\dot{x} + u_y$$

$$\ddot{z} = -n^2 z + u_z$$

This new set of equations forms a linear time-invariant system, allowing the design of linear optimal controllers.

Equations (2.28) made their first appearance in [7]. In this work, dated 1878, Hill studied the motion of the Moon around the Earth, inspired by Euler's "*Theoria motuum lunae nova methodo pertractata*" of 1772 [8]. Clohessy and Wiltshire in 1960 take the credit for using for the first time LERM equations to address the terminal guidance problem [9] and for this reason sometimes Equations (2.27) are known as Clohessy - Wiltshire equations. Other textbook, such as Schaub's [2] and Alfriend's [4], denote with the name Clohessy - Wiltshire equations the Equations (2.28). To avoid confusion, in this thesis Equations (2.27) will be referred with the acronym LERM, whereas linear time-invariant Equations (2.28) will be denoted with the acronym HCW, following Schaub's and Alfriend's nomenclature.

2.2.4 Nonlinear Equations of Relative Perturbed Motion

In presence of perturbations chief's angular momentum is no longer constant and the expression of the angular velocity $\boldsymbol{\omega}$ changes. It can be proved that [10, 11]

$$\omega_x = \frac{\mathrm{d}\Omega}{\mathrm{d}t} \sin i \sin\theta + \frac{\mathrm{d}i}{\mathrm{d}t} \cos\theta$$

$$\omega_y = \frac{\mathrm{d}\Omega}{\mathrm{d}t}\sin i\cos\theta - \frac{\mathrm{d}i}{\mathrm{d}t}\sin\theta$$
$$\omega_z = \frac{\mathrm{d}\Omega}{\mathrm{d}t}\cos i + \theta$$

where $\theta = \omega + f$ is the chief's true latitude (here ω denotes the argument of perigee). Using Gauss variational equations, Equations (2.19), for i and Ω, noting that the LVLH frame coincides with chief's RTN frame,

$$\frac{\mathrm{d}i}{\mathrm{d}t} = \frac{r}{h}\cos\theta\, a_{p,c_z}$$
$$\frac{\mathrm{d}\Omega}{\mathrm{d}t} = \frac{r\sin\theta}{h\sin i}a_{p,c_z}$$

the components of $\boldsymbol{\omega}$ in the LVLH reference system becomes

$$\omega_x = \frac{r}{h}a_{p,c_z}\,, \qquad \omega_y = 0, \qquad \omega_z = \frac{h}{r^2} \tag{2.31}$$

It is worth of note that ω_y will always be zero due to the choice of the LVLH frame unit vectors ($\hat{\boldsymbol{i}}$ always points to the primary body).

The angular acceleration $\dot{\boldsymbol{\omega}}$ can be computed deriving with respect to time Equations (2.31). But first, it is necessary to compute the time derivative of the angular momentum magnitude.

Chief's angular momentum time derivative in presence of perturbations is

$$\frac{\mathrm{d}}{\mathrm{d}t}\boldsymbol{h} = \frac{\mathrm{d}}{\mathrm{d}t}\left(\boldsymbol{r}\times\frac{\mathrm{d}}{\mathrm{d}t}\boldsymbol{r}\right) = \boldsymbol{r}\times\frac{\mathrm{d}^2}{\mathrm{d}t^2}\boldsymbol{r} = \boldsymbol{r}\times\left(-\frac{\mu}{r^3}\boldsymbol{r} + \boldsymbol{a}_{p,c}\right) = \boldsymbol{r}\times\boldsymbol{a}_{p,c}$$

that resolved in the LVLH frame becomes

$$\dot{\boldsymbol{h}} = r\hat{\boldsymbol{i}}\times\left(a_{p,c_x}\hat{\boldsymbol{i}} + a_{p,c_y}\hat{\boldsymbol{j}} + a_{p,c_z}\hat{\boldsymbol{k}}\right) = -ra_{p,c_z}\hat{\boldsymbol{j}} + ra_{p,c_y}\hat{\boldsymbol{k}} \tag{2.32}$$

Remembering the expression of $\boldsymbol{h}$ in the LVLH reference systems, $\boldsymbol{h} = h\hat{\boldsymbol{k}}$, and using Equation (2.17) and Equation (2.32), chief's angular momentum magnitude

time derivative can be computed as follows,

$$\dot{h} = \frac{1}{h}\left(h\hat{\boldsymbol{k}} \cdot \left(-ra_{p,c_z}\hat{\boldsymbol{j}} + ra_{p,c_y}\hat{\boldsymbol{k}}\right)\right) = ra_{p,c_y}$$

The angular acceleration $\dot{\boldsymbol{\omega}}$ is then given by,

$$\begin{aligned}
\dot{\boldsymbol{\omega}} &= \dot{\omega}_x\hat{\boldsymbol{i}} + \dot{\omega}_z\hat{\boldsymbol{k}} \\
&= \frac{1}{h^2}\left(\left(\dot{r}a_{p,c_z} + r\dot{a}_{p,c_z}\right)h - ra_{p,c_z}\dot{h}\right)\hat{\boldsymbol{i}} + \frac{1}{r^4}\left(\dot{h}r^2 - 2hr\dot{r}\right)\hat{\boldsymbol{k}} \\
&= \frac{1}{h}\left(\dot{r}a_{p,c_z} + r\dot{a}_{p,c_z} - \omega_x\dot{h}\right)\hat{\boldsymbol{i}} + \frac{1}{r^2}\left(\dot{h} - 2\omega_z r\dot{r}\right)\hat{\boldsymbol{k}} \\
&= \frac{1}{h}\left(\dot{r}a_{p,c_z} + r\dot{a}_{p,c_z} - \omega_x ra_{p,c_y}\right)\hat{\boldsymbol{i}} + \frac{1}{r}\left(a_{p,c_y} - 2\omega_z\dot{r}\right)\hat{\boldsymbol{k}}
\end{aligned}$$

In this expression the time derivative of the perturbation acceleration along $\hat{\boldsymbol{k}}$ appears. A possible way to compute the perturbation acceleration time derivative in the LVLH frame exploits the relationship existing between a time-derived vector in an inertial frame and the same vector time-derived in a moving frame,

$$\frac{\mathrm{d}}{\mathrm{d}t}\boldsymbol{a}_p = \dot{\boldsymbol{a}}_p + \boldsymbol{\omega} \times \boldsymbol{a}_p \quad \Longleftrightarrow \quad \dot{\boldsymbol{a}}_p = \frac{\mathrm{d}}{\mathrm{d}t}\boldsymbol{a}_p - \boldsymbol{\omega} \times \boldsymbol{a}_p$$

Finally, the terms appearing in the general vectorial equation of relative motion (2.22) can be computed for the perturbed case,

$$\begin{aligned}
2\boldsymbol{\omega} \times \dot{\boldsymbol{\rho}} &= -2\omega_z\dot{y}\hat{\boldsymbol{i}} + 2\left(\omega_z\dot{x} - \omega_z\dot{x}\right)\hat{\boldsymbol{j}} + 2\omega_x\dot{y}\hat{\boldsymbol{k}} \\
\dot{\boldsymbol{\omega}} \times \boldsymbol{\rho} &= -\dot{\omega}_z y\hat{\boldsymbol{i}} + \left(\dot{\omega}_z x - \dot{\omega}_x z\right)\hat{\boldsymbol{j}} + \dot{\omega}_x y\hat{\boldsymbol{k}} \\
\boldsymbol{\omega} \times (\boldsymbol{\omega} \times \boldsymbol{\rho}) &= \left(\omega_x\omega_z z - \omega_z^2\right)\hat{\boldsymbol{i}} - \left(\omega_x^2 + \omega_z^2\right)y\hat{\boldsymbol{j}} + \left(\omega_x\omega_z x - \omega_x^2 z\right)\hat{\boldsymbol{k}}
\end{aligned}$$

The *nonlinear equation of relative perturbed motion* (in the following referred to simply as perturbed NERM) can be obtained introducing the terms in Equations (2.33) into Equation (2.22), substituting the remaining vectors with their LVLH expres-

sions and writing the motion components along LVLH unit vectors separately.

$$\ddot{x} = \left(\omega_z^2 - \frac{\mu}{r_d^3}\right) x + \dot{\omega}_z y - \omega_x \omega_z z + 2\omega_z \dot{y} + \mu \left(\frac{1}{r^2} - \frac{r}{r_d^3}\right) + \Delta a_{p_x} + u_x$$
$$\ddot{y} = -\dot{\omega}_z x + \left(\omega_x^2 + \omega_z^2 - \frac{\mu}{r_d^3}\right) y + \dot{\omega}_x z - 2\omega_z \dot{x} + 2\omega_x \dot{z} + \Delta a_{p_y} + u_y$$
$$\ddot{z} = -\omega_x \omega_z x - \dot{\omega}_x y + \left(\omega_x^2 - \frac{\mu}{r_d^3}\right) z - 2\omega_x \dot{y} + \Delta a_{p_z} + u_z$$

In Section 2.1.4 the expressions in the ECI frame for the most important space perturbations were introduced. In order to compute the differential perturbation acceleration $\Delta \boldsymbol{a}_p$ these accelerations must be expressed in the LVLH frame.

Therefore, once the rotation matrix $\boldsymbol{C}_I^L(\boldsymbol{r}, \boldsymbol{v}) : I \to L$ is introduced,

$$\boldsymbol{C}_I^L(\boldsymbol{r}, \boldsymbol{v}) = \left[\begin{array}{c|c|c} \hat{\boldsymbol{i}}^I & \hat{\boldsymbol{j}}^I & \hat{\boldsymbol{k}}^I \end{array} \right]^T$$

the differential perturbation can be computed as follows.

$$\Delta \boldsymbol{a}_p^L = \boldsymbol{C}_I^L \left(\boldsymbol{a}_{p,d}^I - \boldsymbol{a}_{p,c}^I\right)$$

2.2.5 Orbital Element Differences

Another possible way to describe relative motion makes use of the orbital elements of the two spacecraft. Let the following set of orbital elements describe chief's orbit about the primary body,

$$\boldsymbol{e} = \left[\begin{array}{cccccc} a & \theta & i & q_1 & q_2 & \Omega \end{array} \right]^T$$
$$\theta = \omega + f, \quad q_1 = e\cos\omega, \quad q_2 = e\sin\omega$$

Again, the parameter θ is the chief's true latitude. This set of orbital parameters was introduced by Deprit and Rom in [12] to alleviate the singularity of the classical elements for circular orbits. However, this set is still singular for equatorial orbits.

If the deputy's orbit is described using the same set of parameters, denoted with

$\boldsymbol{e}_d$, then the *orbital element differences* vector $\delta\boldsymbol{e}$ can be introduced,

$$\delta\boldsymbol{e} = \boldsymbol{e}_d - \boldsymbol{e} = \begin{bmatrix} \delta a & \delta\theta & \delta i & \delta q_1 & \delta q_2 & \delta\Omega \end{bmatrix}^T$$

The use of orbital element differences has several advantages. In absence of perturbations and control thrust, all the parameters, except $\delta\theta$, are constant. The true latitude difference variation can be computed using chief's and deputy's orbital elements [2],

$$\begin{aligned}\delta\dot{\theta} =& \dot{f}_d - \dot{f} = \frac{h_d}{r_d^2} - \frac{h}{r^2} = \sqrt{\frac{\mu}{p_d^3}}\left(1 + e_d\cos f_d\right)^2 - \sqrt{\frac{\mu}{p^3}}\left(1 + e\cos f\right)^2 \\ =& \frac{\sqrt{\mu}\left(1 + (q_1 + \delta q_1)\cos\left(\theta + \delta\theta\right) + (q_2 + \delta q_2)\sin\left(\theta + \delta\theta\right)\right)^2}{\sqrt{(a+\delta a)^3\left(1 - (q_1+\delta q_1)^2 - (q_2+\delta q_2)^2\right)^3}} + \\ & - \frac{\sqrt{\mu}\left(1 + q_1\cos\theta + q_2\sin\theta\right)^2}{\sqrt{a^3\left(1 - q_1^2 - q_2^2\right)^3}}\end{aligned}$$

Instead, if perturbations are considered then chief's and deputy's orbital elements will change slowly. However, the components of the Cartesian relative motion state $\boldsymbol{x}$ are fast variables even in the unperturbed case. Therefore, orbit element differences are always preferable from a computing point of view.

The orbit element differences must be computed carefully, since they involve the computation of angle differences. Choosing the domain $[0, 2\pi]$ for the angles and $[-\pi, \pi]$ for their difference, the difference between two angles α_1 and α_2 is given by[3]

$$\alpha_2 - \alpha_1 = \mathrm{mod}\left(\alpha_2 - \alpha_1, 2\pi\right) - \pi \tag{2.35}$$

A complete discussion about orbital element differences can be found in [13, 14].

The NERM state vector $\boldsymbol{x}$ can be transformed into the orbital element differences vector $\delta\boldsymbol{e}$ using a nonlinear transformation function and vice versa. Let $\boldsymbol{g}(\cdot)$ and

[3] mod is the MATLAB modulus function `mod`.

$\boldsymbol{k}(\cdot)$ denote the the two transformation function,

$$\boldsymbol{x} = \boldsymbol{g}(\boldsymbol{e}, \delta\boldsymbol{e}), \qquad \delta\boldsymbol{e} = \boldsymbol{k}(\boldsymbol{e}, \boldsymbol{x})$$

Algorithmically, the transformation function $\boldsymbol{k}(\cdot)$ is composed by the following steps.

1) Compute chief's position in the inertial frame $\boldsymbol{r}^I$ using $\boldsymbol{e}$ (see Section 2.1.3).

2) Compute deputy's position and velocity, respectively $\boldsymbol{r}_d^I$ and $\boldsymbol{v}_d^I$, using NERM solution $\boldsymbol{x} = \left[\boldsymbol{\rho}^L, \dot{\boldsymbol{\rho}}^L\right]^T$ and $\boldsymbol{r}^I$,

$$\boldsymbol{r}_d^I = \boldsymbol{r}^I + \boldsymbol{C}_L^I(\boldsymbol{r}, \boldsymbol{v})\boldsymbol{\rho}^L, \quad \boldsymbol{v}_d^I = \boldsymbol{v}^I + \boldsymbol{C}_L^I(\boldsymbol{r}, \boldsymbol{v})\dot{\boldsymbol{\rho}}^L + \boldsymbol{\omega}^I \times \boldsymbol{C}_L^I(\boldsymbol{r}, \boldsymbol{v})\boldsymbol{\rho}^L$$

3) Compute deputy's orbital element vector $\boldsymbol{e}_d$ using $\boldsymbol{r}_d^I$ and $\boldsymbol{v}_d^I$ (see Section 2.1.3).

4) Compute orbital elements difference vector $\delta\boldsymbol{e} = \boldsymbol{e}_d - \boldsymbol{e}$, using for angles differences Equation (2.35).

The transformation function $\boldsymbol{g}(\cdot)$ can be obtained adapting the precedent algorithm and following the steps in opposite order, inverting each one.

A linear transformation between NERM solution and orbit element differences was proposed by Schaub et al. in [2, 15, 16]. Assume that the relative orbit radius ρ is smaller than the chief orbit radius r. Then, the components of $\boldsymbol{x}$ can be written in terms of orbit element differences vector components as follows,

$$\begin{aligned}
x =& \frac{r}{a}\delta a + \frac{v_r}{v_t} r\delta\theta - \frac{r}{p}\left(2aq_1 + r\cos\theta\right)\delta q_1 - \frac{r}{p}\left(2aq_2 + r\sin\theta\right)\delta q_2 \\
y =& r\delta\theta + r\cos i\,\delta\Omega \\
z =& r\sin\theta\,\delta i - \cos\theta\sin i\,\delta\Omega \\
\dot{x} =& -\frac{v_r}{2a}\delta a + \left(\frac{1}{r} - \frac{1}{p}\right) h\delta\theta + \left(v_r a q_1 + h\sin\theta\right)\frac{\delta q_1}{p} + \\
&+ \left(v_r a q_2 - h\cos\theta\right)\frac{\delta q_2}{p}
\end{aligned}$$

$$\begin{aligned}\dot{y} =& -\frac{3v_t}{2a}\delta a - v_r\delta\theta + (3v_t a q_1 + 2h\cos\theta)\frac{\delta q_1}{p} + \\ &+ (3v_t a q_2 + 2h\sin\theta)\frac{\delta q_2}{p} + v_r\cos i\,\delta\Omega \\ \dot{z} =& (v_t\cos\theta + v_r\sin\theta)\,\delta i + (v_t\sin\theta - v_r\cos\theta)\sin i\,\delta\Omega\end{aligned}$$

where chief's radial v_r and transversal v_t velocity components were introduced,

$$v_r = \frac{h}{p}\left(q_1\sin\theta - q_2\cos\theta\right), \qquad v_t = \frac{h}{p}\left(1 + q_1\cos\theta + q_2\sin\theta\right)$$

The transformation operated by Equations (2.36) can also be expressed by an orbit-dependent matrix $\boldsymbol{G}(\boldsymbol{e})$,

$$\boldsymbol{x} = \boldsymbol{G}(\boldsymbol{e})\delta\boldsymbol{e}$$

and the inverse mapping is given by the inverse of $\boldsymbol{G}(\boldsymbol{e})$.

Chapter 3

Relative Motion Control

Relative motion control was studied extensively during the years, since its importance for future missions development. Robust and optimal control techniques are sought in order to improve spacecraft autonomy during common operations, such as rendezvous and docking with an another spacecraft, primitive body inspection and so on. However, solutions proposed so far do not seem fully mature, as proved by the numerous glitches and anomalies occurred during the various demonstration missions. Thus, great efforts are being made by the scientific community to find a reliable solution for relative motion control problem.

In this chapter, relative motion control is discussed. The problem is stated and application and control requirements discussed. The chapter ends with a brief survey of the proposed solutions that can be found in literature. The discussion here offered is based principally on [17].

3.1 Problem Statement

Relative motion control may be classified as a classical problem of guidance, navigation and control (GN&C), since the objective is to pursue a moving target and to keep a specific position with respect to this. Optimal GN&C problems require

the minimization of a cost function,

$$\min_{t_f, \boldsymbol{u}} \left\{ \psi_f(\boldsymbol{x}(t_f)) + \int_{t_0}^{t_f} \psi(\boldsymbol{x}(t), \boldsymbol{u}(t)) \, \mathrm{d}t \right\}$$

subject to the following constraints $\forall t \in [t_0, t_f]$

$$\dot{\boldsymbol{x}}(t) = f(t, \boldsymbol{x}(t), \boldsymbol{u}(t))$$

$$\boldsymbol{x}(t) \in \mathcal{X}(t)$$

$$\boldsymbol{u}(t) \in \mathcal{U}(t)$$

Here $\boldsymbol{x} \in \mathbb{R}^n$ is the state of the spacecraft, $\boldsymbol{u} \in \mathbb{R}^m$ is the control vector, t_0 and t_f are respectively initial and final time, $\psi : \mathbb{R}^n \times \mathbb{R}^m \to \mathbb{R}$ and $\psi_f : \mathbb{R}^n \to \mathbb{R}$ are cost functions, $f : \mathbb{R} \times \mathbb{R}^n \times \mathbb{R}^m \to \mathbb{R}^n$ is the system dynamic, $\mathcal{X}(t) \subseteq \mathbb{R}^n$ and $\mathcal{U}(t) \subseteq \mathbb{R}^m$ define control and state constraints that depend on time.

As seen in Chapter 2, numerous dynamical models for relative motion description exist, with different degree of accuracy. Optimal closed-form solutions can be found if linear time-invariant models (e.g. HCW equations) without constraints on control and state are chosen. However, they might not be of interest for a real implementation, since constraints are ignored and error might grow significantly as a result of linear approximation. If constraints are introduced, then numerical methods are required in order to find a solution. Adoption of nonlinear models increases control algorithm computational cost. Since control action must be computed quickly, resolution of nonlinear optimal control problem might be infeasible, especially if several constraints are introduced. Hence, a trade-off between solution requirements (optimality, constraints, accuracy) and computational cost must be found.

3.2 Application Requirements

Space missions design usually deals with lot of different requirements, in order to achieve mission's goals and guarantee safety of involved vehicles during the operations. Moreover, space is an harsh environment characterized by many sources of disturbance (e.g. solar radiation, rarefied atmosphere at low Earth orbits, etc.) and, in the last decades, by a growing number of debris in orbit. All this problems must be addressed during spacecraft development and mission planning.

The relative guidance problem shares some of the requirements of a general space mission, but is demanded to satisfy specific constraints according to the mission (proximity operations for primitive bodies, autonomous rendezvous and docking, autonomous inspection and servicing). Minimization of fuel consumption is the most important, in order to extend as much as possible mission lifetime. Well defined approaching maneuvers characterize automatic rendezvous and docking missions (e.g. V-bar maneuver), as well as collision avoidance with the target spacecraft.

Here a non exhaustive list of the most common requirements is proposed. Mathematical expressions are developed when possible.

- **Fuel consumption minimization**: Mission lifetime is strictly related to fuel consumption. Spacecraft refuel and resupply is currently impossible due to the high cost to access space, thus minimization of propellent usage is a key factor.

- **Limitations on thrusters and silence times handling**: Proper handling of thrusters capability is essential to improve spacecraft performance. Thrusters have finite upper bounds on force they can provide, due to limitation on fuel storage and nozzle design constraints. Moreover, they cannot exert arbitrarily small forces. These limitations affect the accuracy of critical operations, such as docking and proximity flight, if not proper handled. Control must also guarantee silence times between thrusters firings. During firing noise is introduced in the state estimation. Silence periods give to the state

estimator time to cut off this noise and reacquire a proper degree of accuracy.

Thruster limitation can be easily described as follows,

$$u_{T,j}(t) \in \{0\} \cup [\underline{u}_{T,j}, \overline{u}_{T,j}], \quad 0 < \underline{u}_{T,j} < \overline{u}_{T,j} \quad \forall j = 1, \ldots, n_T$$

whereas silence times can be modelled as null control during prescribed time periods,

$$u_{T,j}(t) = 0 \quad \forall j = 1, \ldots, n_T \quad \text{when} \quad t \in \bigcup_{j=1,\ldots,n_s} \mathcal{T}_j$$

where $u_{T,j}$ is the thruster j command signal, n_T is the number of thrusters and $\mathcal{T}_j$ are a disjoint set of n_s silence time intervals.

- **Plume impingement avoidance**: Thrusters pointing at close objects must not fire, in order to avoid plume impingement. As a matter of fact, thrusters plume can damage spacecraft sensors and coatings and also introduce disturbance forces and torques. Moreover, during docking operations target vehicle can be damaged or, in case the target is a primitive body like an asteroid, plume impingement can seriously contaminate the examination area.

  Constraint for avoiding plume impingement can be stated in the following form,

  $$u_{T,j} = 0 \quad \text{if} \quad \boldsymbol{\rho}^L \cdot \boldsymbol{C}_B^L(\boldsymbol{q}) \hat{\boldsymbol{t}}_j^B \geq \rho \cos \beta_p \quad \text{and} \quad \rho \leq R_p$$

  Here $\boldsymbol{\rho}$ is the vector of relative position, $\boldsymbol{C}_L^B(\boldsymbol{q})$ is the coordinate transformation matrix from body frame $\{B\}$ to LVLH frame $\{L\}$ that depends on spacecraft attitude quaternion $\boldsymbol{q}$, $\hat{\boldsymbol{t}}_j$ is the unit vector denoting firing direction of thruster j, β_p is the plume cone angle and R_p is the maximum effective plume radius.

- **Collision avoidance**: Collision with target and other obstacles along the approaching path must be avoided. A collision can seriously damage the spacecraft or other participating vehicles, resulting in an immediate mission

failure.

Denoting with $\boldsymbol{r}$ the spacecraft position and with $\boldsymbol{r}_{O,j}$ the position of obstacle j, assuming the presence of n_O obstacles, to avoid collision the following expressions must hold,

$$\left|\left|\boldsymbol{r} - \boldsymbol{r}_{O,j}\right|\right| > R_{O,j} \quad \forall j = 1, \ldots, n_O$$

For the sake of simplicity, here it is assumed that all the obstacles are surrounded by a sphere of radius $R_{O,j}$. This radius is different for every obstacle, in order to account for its dimensions and shape.

- **Constraint on sensor field-of-view**: Several sensors need to face the target in order to acquire its position and attitude (e.g. vision and laser based systems). Therefore, spacecraft must keep a proper attitude while approaching the target.

  Mathematically, this requirement can be expressed as follows,

$$\boldsymbol{\rho}^L \cdot \boldsymbol{C}_B^L(\boldsymbol{q})\hat{\boldsymbol{n}}^B \geq \rho \cos\frac{\alpha}{2}$$

  where $\hat{\boldsymbol{n}}$ and α are, respectively, the field-of-view direction and aperture angle.

- **Uncertainties handling**: Relative motion equations used for control design usually do not consider the several disturbances present in the space environment. Moreover, the accuracy of linearized models (e.g. HCW and LERM) decreases as the relative distance between chief and deputy increases. Sensors measurements may become an additional problem when significantly affected by noise or show large errors. All these uncertainties should be modelled as much as possible and considered during control design.

3.3 Control Algorithm Requirements

Autonomy is a key enabling factor for future space missions. Currently most missions rely on ground-in-the-loop architectures but this will not be sustainable in future, since the growing number of spacecraft in orbit and the delays that affect communication. Significant improvements in spacecraft autonomy were made during the years (Mars Curiosity mission is the most important result), but recent anomalies on autonomous demonstration missions (e.g. NASA's DART spacecraft [18], AVGS test on DARPA's Orbital Express [19]) points out the technology immatureness. The National Research Council identified robotics and autonomous systems as an high-priority technology area [20].

Reliable and fault-tolerance control techniques are required to increase autonomy. Thus, control algorithms must satisfy the following requirements:

- **Robustness**: The algorithm should find a feasible solution if one exists, possibly an optimal one.
- **Real-time implementability**: The control law must be implementable and able to execute processing operations with certified off-the-shelf components in a finite and reasonable amount of time.
- **Verifiability**: Performance and robustness of the proposed algorithm must be validated using proper metrics.

3.4 Spacecraft Propulsion and Control

Thrusters handling was listed in Section 3.2 among the application requirements. Different propulsion systems are currently employed, depending on mission requirements and goals. From control design point of view, they can be classified in,

- **High-thrust systems**: In these systems the duration of thrust arcs is short compared to the mission time. Hence, thruster firings are modelled as isolated

events, i.e. as impulses. Thrust optimization is then reduced to a discrete-time optimal control problem.

- **Low-thrust systems**: Conversely, low-thrust propulsion systems are employed for a significant part of the overall mission time. Control then is modelled as a continuous function and a continuous-time optimal control problem need to be set up and resolved.

Examples of high-thrust propulsion system are rocket engines, instead among low-thrust system the most diffused are electromagnetic propulsion systems. Compared to low-thrust propulsion systems, optimal solution computation for spacecraft with high-thrust propulsion is easier, since a discrete optimal control problem need to be solved. On the other hand, resolution of continuous optimization problem is not straightforward and might be time-consuming.

In addition to the before mentioned classes, there is a third class of propulsion systems that do not use any reaction mass to generate thrust. Gravitational and magnetic fields, electromagnetic waves, solar wind and radiation can be exploited in order to move a spacecraft, especially inside the Solar System. Two examples of propulsion without internal reaction mass are solar sails, that use radiation pressure from electromagnetic energy, and magnetic sails, that use a magnetic field to deflect charged particles from solar wind. These types of propulsion systems do not require propellent, thus time minimization is of interest.

3.5 Literature Review

Numerous control laws and techniques were developed for relative motion control problem during the years. An interesting survey is presented in [21], with emphasis on the optimization methods currently available. Another reference worth of note is [17], where the authors propose a classification for current state-of-the-art control algorithms and discuss their vantages and weak points. The work is focused in particular on the necessary developments for autonomy improving of future space

missions, with reference to NASA's needs for the 2011-2021 decade [20].

Here a possible classification of relative motion control techniques is proposed, based on the previously cited works.

- Model predictive control.
- Artificial potential functions based controls.
- Motion planning algorithms.
- Optimal and suboptimal control laws.
- Glideslope guidance.
- Other controls.

In the next sections a brief description of these classes of control technique is offered, as well as references to the most representative implementation proposed in literature.

3.5.1 Model Predictive Control

Model predictive control (MPC) computes a feedback law solving an optimal control problem at each sample time, using current state as initial state. State evolution is predicted using a mathematical model of the system and then used to compute control over a prescribed time period (*time horizon*). For these characteristics, MPC is usually referred to as *receding* (or *moving*) *horizon optimal control*. Recalculation of control law allows disturbance mitigation and error reduction. One of the main advantages of this method is the framework offered to control designers, that ease the introduction of constraints on state and control, increasing, however, computational cost. Closed-loop stability and state convergence can be proved under appropriate assumptions without prior knowledge of disturbances [22]. A classical reference for MPC is [23].

MPC was used extensively for relative motion control. The main drawback of this technique for this kind of problem is its real-time implementation. As a matter

of fact, many solutions proposed in literature rely on linear or linear time-varying dynamic models, eluding nonlinear equations that drastically increase optimal control computation time.

Petersen et al. in [24] propose a rendezvous control algorithm based on MPC and supported by a collision avoidance routine, using HCW equations as dynamic model. Another example for rendezvous and proximity operations, using HCW equations, is proposed in [25], but here with constraints on thrust magnitude, spacecraft positioning (chief vehicle must be within deputy's field-of-view) and soft-docking requirement (deputy's velocity must match chief's velocity at the end of the maneuver). A comparison between the use of MPC on NERM equations and a linearized version of Gauss variational equation is presented in [26], whereas the authors of [27] propose a framework for MPC design and implementation using LERM equations, dividing rendezvous operation in four phases, each one with different requirements.

3.5.2 Artificial Potential Functions Based Controls

Artificial potential functions (APF) based controls represent the environment by potential functions distributed over the state space. Repulsive potentials are used to represent obstacles, whereas attractive potentials denote goal regions. The path to the goal is obtained using algorithms based on gradient ascent, or setting up an optimal control problem. Representation of dynamic environment, where both obstacles and goals change their positions, could be difficult and computationally onerous. Another drawback of APF controls is the possible convergence to local minima if the potential functions are not properly defined. Additional heuristic techniques are required in order to prevent this phenomenon.

One of the first examples of APF control was presented by Lopez et al. in [28]. Roger et al. in [29] discuss a possible implementation for a free-flying robot camera aimed at International Space Station inspection. Other important examples of APF controls can be found in [30], where the technique is employed for construction of in-orbit structures using swarms of free-flying spacecrafts, and in [31] where it is

proposed for configuring satellite formations.

3.5.3 Motion Planning Algorithms

A *motion planning algorithm* generates a sequence of decisions, a *plan*, that navigate an agent or a group of agents from an initial state to one or more desired states. During the planning phase, different type of requirements may be taken in account, e.g. collision avoidance, dynamic constraints of the agent (for example turning radius), etc. Motion planning can be *exact* (*combinatorial*) or *approximate* (*sampling-based*). The former class computes the possible paths using a complete representation of the configuration space; the latter avoid the explicit construction of the obstacles configuration space and explores possible paths to the goal via sampling. In this case a collision detection algorithm ensure the safety of the trajectory. Combinatorial planning always find a solution if one exists, whereas sampling-based algorithms cannot guarantee the existence of feasible plans in finite time without drawing an infinite set of samples. However, approximate motion planning demands less computational resources and has great appeal for real-time implementation.

Although motion planning is widely used in many different fields, few space applications can be found. As a matter of fact, motion planning finds feasible paths rather than optimal ones. This limitation has increased the interest in developing algorithms that can offer some kind of optimality, even weak.

Two interesting spacecraft motion planning algorithms are proposed in [32] and [33]. The first reference focuses on real-time implementation of sampling-based planning algorithms able to coordinate multiple spacecraft. Impulsive propulsion is considered and obstacles avoidance is achieved using a collision avoidance algorithm. Planning algorithm also takes in account plume impingement avoidance. The second reference split planning in an offline phase, aimed to find a path that avoids known obstacles and plume impingement, and an online phase, for real-time avoidance of unaccounted obstacles and error growth mitigation. Between feasible paths, the optimal one is chosen.

3.5.4 Optimal and Suboptimal Control Laws

Numerous optimal and suboptimal control laws were proposed during the years, with particular focus on fuel consumption. Relative motion equations in their nonlinear form are difficult to manipulate, thus most of the solutions proposed in literature assume chief in circular orbits, or small distance between deputy and chief, so that HCW and LERM equations can be adopted.

A series of papers worth of note for optimal control were written by Carter and co-workers. General linear equations of relative motion (either with time or chief's true anomaly as independent variable, see Section 4.1) are used to develop fuel-optimal control [34], accounting for spacecraft mass change due to fuel consumption [35] and constraints on thruster power [36, 37]. Proposed controls are extended to the nonlinear case updating the gain matrix periodically.

Recent works consider more difficult scenarios and other type of constraints. For example in [38] rendezvous with an uncontrolled tumbling object is considered. The authors develop controls for relative motion and attitude, using HCW equations and quaternions. Optimality is achieved through recursive methods. Baldwin et al. in [39] propose a robust and optimal control, again considering motion governed by HCW equations. Presence of bounded disturbances is assumed and field-of-view constraint is taken in account. In [40] an optimal trajectory is computed using geometric Hermite interpolation and a robust controller for reference tracking is developed.

When nonlinear equations are considered, numerical methods are required to obtain an optimal solution. Computational cost of these algorithms could significantly impact real-time implementation. Therefore, control requirements are usually relaxed in order to find a trade-off between optimality and real-time implementability. A survey of optimization methods is proposed in [41] and a framework for optimal control is developed in [42]. In particular, different types of models for relative motion are considered and optimal control is the result of recursive resolution methods.

Suboptimal solutions using nonlinear equations may be developed using State-

Dependent Riccati Equations control (SDRE). The method is discussed in Chapter 5, as well as some of the solutions proposed so far in literature that use this control technique.

3.5.5 Glideslope Guidance

In the *glideslope guidance* control technique the controlled vehicle approaches the target along a straight line. This is one of the most simple control and it is widely used in current rendezvous and docking operations with the International Space Station (e.g. H-II Transfer Vehicle (HTV) [43] and Automated Transfer Vehicle (ATV) [44]). Crew on-board the station can easily monitor the maneuver and detect anomalies during the approaching. However, glideslope trajectory generally is not optimal. Still, this guidance technique is valuable for close range rendezvous when spacecraft is demanded to move along a fixed direction for safety reasons and for docking procedure.

Glideslope guidance is discussed in detail in [45]. In [46] optimal glideslope guidance is derived in the case of chief's circular orbits.

3.5.6 Other Controls

A lot of different techniques were used during the years to address the rendezvous problem, coming from different fields and sometimes inspired by nature, as in the case of [47], where the hoverfly mating is analysed. This particular mating is characterized by trajectories that do not require acceleration. The idea is to find a way to generate this trajectory for space rendezvous, mimicking the hoverfly behaviour. Use of classical robotics control methods, such as computed torque, is proposed in [48] where NERM equations are manipulated and written in Lagrange form. Neural networks use was also investigated. In [49] a finite-horizon optimal control is developed, based on approximate dynamic programming. A fuzzy controller is presented in [50]. An extended command governor is proposed in [24] to generate a reference trajectory that takes in account control requirements. An LQR controller

is then developed in order to track the generated trajectory.

3.6 Comment on Proposed Solutions

Relative motion control demands an optimal and robust solution in order to meet the application requirements and operate in a dynamic environment autonomously. Many of the proposed solutions are computationally expensive or based on linearized equations that might be inaccurate for large separations. Moreover, introduction of constraints in optimal and suboptimal problems is not straightforward. Other techniques were developed to cope with constraints integration and to reduce computational costs, but they often lack of optimality.

Two promising techniques are MPC and SDRE. The first one offers a ready-to-use framework that considers optimality, constraints, disturbances, and collision avoidance, but, again, it could be time-consuming if it is not proper designed. SDRE controls, among the techniques analysed here, are the closest to the sought optimality. However, constraints integration it is not easy and ARE resolution need to be proper handled for real-time implementation.

Chapter 4

A Near-Optimal Control Law for Relative Motion

In this section a recently proposed near-optimal control law for relative motion is presented. Sinclair and co-workers developed, in a series of papers, tools aimed to extend linear optimal control laws, designed using HCW equations, to LERM and NERM equations of motion. The result is a near-optimal controller for nonlinear equations of relative motion. By means of Lyapunov - Floquet theory, it is possible to find several transformation functions that relate HCW equations to LERM solution and vice versa. Moreover, a calibration process for LERM state vector was developed to reduce the error introduced by the assumptions at the base of NERM linearization (small distance between chief and deputy). Combining this two results, the authors obtained a control architecture that currently is one of the most close to the optimality. Therefore, it is a good reference for drawing a comparison with the controllers that will be developed in the next sections.

The Lyapunov-Floquet transformation matrices are discussed in Section 4.1. The calibration process is presented in Section 4.2 and in Section 4.3 a series of simulations are proposed to show the advantages of using the calibrated state rather than the true state.

4.1 HCW to LERM Transformation Matrices

According to the Lyapunov - Floquet theory, it is possible to introduce a change of coordinates that reduces a linear time-periodic autonomous system, i.e. a system of the form $\dot{\boldsymbol{x}} = \boldsymbol{A}(t)\boldsymbol{x}$ where $\boldsymbol{A}(t)$ is T periodic such that $\boldsymbol{A}(t) = \boldsymbol{A}(t+T)$, to a system of constant coefficients (see [51] and reference therein). Sherrill et al. in [51, 52] exploit the instruments offered by this theory and develop a series of transformations functions that relate HCW solutions to LERM solutions in a one-by-one manner. The transformations make use of LERM and HCW state transition matrices, that are here briefly introduced.

HCW equations set is linear time-invariant and it may be written in the form

$$\dot{\boldsymbol{x}}_{\mathrm{H}}(t) = \boldsymbol{A}\boldsymbol{x}_{\mathrm{H}}(t) + \boldsymbol{B}\boldsymbol{u}(t)$$

where $\boldsymbol{x}_{\mathrm{H}}$ is the HCW state vector. The state transition matrix $\boldsymbol{\Phi}_{\mathrm{HCW}}$ is given by

$$\boldsymbol{x}_{\mathrm{H}}(t) = e^{\boldsymbol{A}(t-t_0)}\boldsymbol{x}_{\mathrm{H}}(t_0) = \boldsymbol{\Phi}_{\mathrm{HCW}}\left(t, t_0\right)\boldsymbol{x}_{\mathrm{H}}(t_0)$$

LERM equations are instead linear time-varying. The state transition matrix $\boldsymbol{\Phi}_{\mathrm{LERM}}$ may be obtained by means of an another set of equations for relative motion: the *Tschauner - Hempel equations set* (TH) [53]. This set is the result of a coordinate change operated by the transformation matrix $\boldsymbol{T}(f)$ on LERM state vector,

$$\boldsymbol{x}_{\mathrm{T}} = \boldsymbol{T}(f)\boldsymbol{x}_{\mathrm{L}}, \qquad \boldsymbol{T}(f) = \begin{bmatrix} (1+e\cos f)\,\boldsymbol{I}_{3\times 3} & \boldsymbol{0}_{3\times 3} \\ -e\sin f\,\boldsymbol{I}_{3\times 3} & \frac{p^2}{h(1+e\cos f)}\boldsymbol{I}_{3\times 3} \end{bmatrix}$$

TH state vector or solution is denoted with $\boldsymbol{x}_{\mathrm{T}}$, whereas $\boldsymbol{x}_{\mathrm{L}}$ is LERM state vector. Applying the transformation to LERM equations results in the Tschauner-Hempel

equations set,

$$
\begin{aligned}
x''_{\mathrm{T}} &= \frac{3}{1+e\cos f}x_{\mathrm{T}} + 2y'_{\mathrm{T}} \\
y''_{\mathrm{T}} &= -2x'_{\mathrm{T}} \\
z''_{\mathrm{T}} &= -z_{\mathrm{T}}
\end{aligned}
$$

The operator $(\cdot)'$ denotes the derivation with respect to the true anomaly f. This new set of equations is nonlinear and it is a function of f instead of the time. Different solutions were proposed in literature (a review can be found in [54]). Sherrill et al. in [52] adopt the following solution that consists in a matrix $\boldsymbol{\Psi}$ and in a vector $\boldsymbol{k}$ defined as

$$
\boldsymbol{\Psi}(f) = \begin{bmatrix} \psi_1 & \psi_2 & \psi_3 & \psi_4 & \psi_5 & \psi_6 \end{bmatrix}, \qquad \boldsymbol{k} = \boldsymbol{\Psi}^{-1}(f)\boldsymbol{T}(f)\boldsymbol{x}(t)
$$

The columns of $\boldsymbol{\Psi}$ are

$$
\psi_1 = \begin{bmatrix} (1+e\cos f)\sin f \\ 2\cos f - e\sin^2 f \\ 0 \\ \cos f + e\cos 2f \\ -2\,(1+e\cos f)\sin f \\ 0 \end{bmatrix}, \qquad \psi_2 = \begin{bmatrix} (1+e\cos f)\cos f \\ -2\sin f - e\sin f\cos f \\ 0 \\ -\sin f - e\sin 2f \\ e - 2\,(1+e\cos f)\cos f \\ 0 \end{bmatrix}
$$

$$
\psi_3 = \begin{bmatrix} 1 - \frac{3}{2}Ke\,(1+e\cos f)\sin f \\ -\frac{3}{2}K\,(1+e\cos f)^2 \\ 0 \\ -\frac{3}{2}Ke\,(\cos f + e\cos 2f) - \frac{3e\sin f}{2(1+e\cos f)} \\ 3Ke\,(1+e\cos f)\sin f - \frac{3}{2} \\ 0 \end{bmatrix}, \qquad \psi_4 = \begin{bmatrix} 0 \\ 1 \\ 0 \\ 0 \\ 0 \\ 0 \end{bmatrix}
$$

$$\psi_5 = \begin{bmatrix} 0 \\ 0 \\ \sin f \\ 0 \\ 0 \\ \cos f \end{bmatrix}, \qquad \psi_6 = \begin{bmatrix} 0 \\ 0 \\ \cos f \\ 0 \\ 0 \\ -\sin f \end{bmatrix}$$

where it was introduced

$$K \triangleq \frac{M}{(1-e^2)^{\frac{3}{2}}}$$

with M chief's *mean anomaly* defined as

$$M(t) \triangleq nt$$

where n is chief's orbit mean motion, Equation (2.8). Solution of Equations (4.1) is then

$$\boldsymbol{x}_{\mathrm{T}} = \boldsymbol{\Psi}(f)\boldsymbol{k}$$

and after evaluating $\boldsymbol{k}$ at t_0 the solution of LERM equations can be constructed exploiting the relationship with the TH equations,

$$\boldsymbol{x}_{\mathrm{L}}(t) = \boldsymbol{T}^{-1}(f)\boldsymbol{\Psi}(f)\boldsymbol{\Psi}^{-1}(f_0)\boldsymbol{T}(f_0)\boldsymbol{x}_{\mathrm{L}}(t_0) = \boldsymbol{\Phi}_{\mathrm{LERM}}(f, f_0)\boldsymbol{x}_{\mathrm{L}}(t_0)$$

Having introduced HCW and LERM state transition matrices, it is now possible to present the Lyapunov - Floquet transformation matrices developed by Sherrill.

The first transformation provides exact matching between the position components of $\boldsymbol{x}_{\mathrm{H}}$ and $\boldsymbol{x}_{\mathrm{L}}$ at periapse and thus it was named *periapse-matching transformation*,

$$\boldsymbol{x}_{\mathrm{L}} = \boldsymbol{P}(f)\boldsymbol{x}_{\mathrm{H}}, \qquad \boldsymbol{P}(f) = \boldsymbol{\Phi}_{\mathrm{LERM}}(f, 0)\boldsymbol{P}_0\boldsymbol{\Phi}^{-1}_{\mathrm{HCW}}(t, 0)$$

It was assumed that $f(t_0) = 0$ and $t_0 = 0$. $\boldsymbol{P}_0$ is a constant matrix that depends on

chief's orbit:

$$\boldsymbol{P}_0 = \begin{bmatrix} \frac{2\left(1-e^2\right)^{\frac{5}{2}}}{(e+1)^3(e+2)} & 0 & 0 & 0 & \frac{\left(1-e^2\right)^{\frac{5}{2}}}{n(e+1)^3(e+2)} - \frac{1}{2n} & 0 \\ 0 & 1 & 0 & 0 & 0 & 0 \\ 0 & 0 & 1 & 0 & 0 & 0 \\ 0 & \frac{eh(e+1)}{p^2} & 0 & \frac{np^2(e+1)^2}{h(1-e^2)^{\frac{5}{2}}} & 0 & 0 \\ 0 & 0 & 0 & 0 & \frac{h(e+1)(e+2)}{2np^2} & 0 \\ 0 & 0 & 0 & 0 & 0 & 1 \end{bmatrix}$$

The *apoapse-matching transformation* provides instead an approximate position matching at apoapse. The transformation matrix $\overline{\boldsymbol{P}}(f)$ is given by the following formula,

$$\boldsymbol{x}_{\mathrm{L}} = \overline{\boldsymbol{P}}(f)\boldsymbol{x}_{\mathrm{H}}, \qquad \overline{\boldsymbol{P}}(f) = \boldsymbol{\Phi}_{\mathrm{LERM}}(f,\pi)\overline{\boldsymbol{P}}_0\boldsymbol{\Phi}_{\mathrm{HCW}}^{-1}\left(t, \frac{\pi}{n}\right)$$

where $\overline{\boldsymbol{P}}_0$ is defined as

$$\overline{\boldsymbol{P}}_0 = \begin{bmatrix} \frac{2\left(1-e^2\right)^{\frac{5}{2}}}{(e-1)^3(e-2)} & 0 & 0 & 0 & \frac{\left(1-e^2\right)^{\frac{5}{2}}}{n(e-1)^3(e-2)} - \frac{1}{2n} & 0 \\ 0 & 1 & 0 & 0 & 0 & 0 \\ 0 & 0 & 1 & 0 & 0 & 0 \\ 0 & \frac{eh(e-1)}{p^2} & 0 & 4e+1 & 0 & 0 \\ 0 & 0 & 0 & 0 & \frac{h(e-1)(e-2)}{2np^2} & 0 \\ 0 & 0 & 0 & 0 & 0 & 1 \end{bmatrix}$$

These transformations can be used to extend control laws developed for HCW equations to LERM equations. Assume to control HCW equations using a linear quadratic regulator (LQR) characterized by a gain matrix $\boldsymbol{K}$. By means of the following formula it is possible to extend the control law to LERM equations,

$$\boldsymbol{u}(t) = -\left(\boldsymbol{B}^T\boldsymbol{B}\right)^{-1}\boldsymbol{B}^T\boldsymbol{P}(t)\boldsymbol{B}\boldsymbol{K}\boldsymbol{P}^{-1}\boldsymbol{x}_{\mathrm{L}}(t) \tag{4.2}$$

In this way a pseudo-optimal control law was obtained for LERM equations.

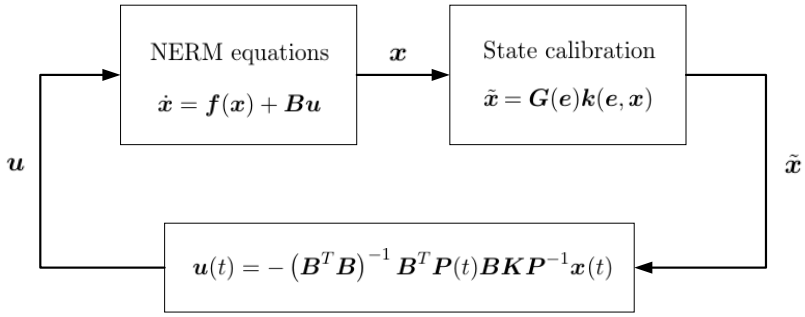

Figure 4.1: Relative motion control using calibrated state.

4.2 State Calibration

Control law presented in Equation (4.2) can be also used to control NERM equations. In order to mitigate the linearization error, Sinclair et al. developed in [55] a state calibration procedure.

The calibration process is based on the nonlinear and linear transformation functions that relates orbital element differences and Cartesian state vector, introduced in Section 2.2.5. In particular, the state calibration is performed combining the transformation function $\boldsymbol{k}(\boldsymbol{e}, \boldsymbol{x})$ and the transformation matrix $\boldsymbol{G}(\boldsymbol{e})$,

$$\tilde{\boldsymbol{x}}_{\mathrm{N}} = \boldsymbol{G}(\boldsymbol{e})\boldsymbol{k}(\boldsymbol{e}, \boldsymbol{x}_{\mathrm{N}})$$

NERM state vector is denoted with $\boldsymbol{x}_{\mathrm{N}}$, whereas $\tilde{\boldsymbol{x}}_{\mathrm{N}}$ is the *calibrated state*. After the calibration process, $\tilde{\boldsymbol{x}}_{\mathrm{N}}$ is given in input to the control law described by Equation (4.2) (Figure 4.1). In [55] it is shown that the state calibration process improves the accuracy and expands the domain of validity of the linearized approximation. In the following section the use of the calibrated state for NERM control is compared against the use of the true state.

4.3 True State vs. Calibrated State Feedback

The performance of the calibrated state feedback controller was analysed and compared against the use of the true state in [56]. The following chief's orbit around

Table 4.1: Test cases, $e = 0$.

Orbital element differences $\delta\boldsymbol{e}$	Cartesian state vector $\boldsymbol{x}$					
	x (km)	y (km)	z (km)	$\dot{x}$ (km/s)	$\dot{y}$ (km/s)	$\dot{z}$ (km/s)
$\delta e = 0.01$, $\delta i = 0.01\,\text{rad}$	-110	0	0	0	0.120	0.061
$\delta e = 0.1$, $\delta i = 0.1\,\text{rad}$	-1100	0	0	0	1.204	0.664
$\delta e = 0.2$, $\delta i = 0.2\,\text{rad}$	-2200	0	0	0	2.410	1.465
$\delta\Omega = \delta\omega = 0.01\,\text{rad}$	-1.476	147.617	-103.356	$2.658 \cdot 10^{-6}$	$2.658 \cdot 10^{-4}$	$6.624 \cdot 10^{-4}$
$\delta\Omega = \delta\omega = 0.1\,\text{rad}$	-147.131	1471.245	-1025.021	0.003	0.026	0.066
$\delta\Omega = \delta\omega = 0.2\,\text{rad}$	-582.658	2912.806	-1998.634	0.021	0.104	0.261

Table 4.2: Test cases, $e = 0.3$.

Orbital element differences $\delta\boldsymbol{e}$	Cartesian state vector $\boldsymbol{x}$					
	x (km)	y (km)	z (km)	$\dot{x}$ (km/s)	$\dot{y}$ (km/s)	$\dot{z}$ (km/s)
$\delta e = 0.01$, $\delta i = 0.01\,\text{rad}$	-110	0	0	0	0.208	0.083
$\delta e = 0.1$, $\delta i = 0.1\,\text{rad}$	-1100	0	0	0	2.118	0.918
$\delta e = 0.2$, $\delta i = 0.2\,\text{rad}$	-2200	0	0	0	4.359	2.071
$\delta\Omega = \delta\omega = 0.01\,\text{rad}$	-1.033	103.332	-72.350	$3.622 \cdot 10^{-6}$	$3.622 \cdot 10^{-4}$	$9.027 \cdot 10^{-4}$
$\delta\Omega = \delta\omega = 0.1\,\text{rad}$	-102.992	102.871	-717.515	0.004	0.036	0.090
$\delta\Omega = \delta\omega = 0.2\,\text{rad}$	-407.860	2038.964	-1399.044	0.029	0.142	0.356

the Earth was chosen,

$$a = 11\,000\,\text{km}, \quad e = \{0,\, 0.3\}, \quad i = 70^\circ, \quad \Omega = 45^\circ, \quad \omega = 0, \quad f(t_0) = 0$$

Six different initial condition in terms of orbit element differences and two different chief's orbit eccentricity were considered, resulting in twelve test cases. These are shown in Tables 4.1 and 4.2, along with the equivalent Cartesian state.

A linear quadratic regulator was designed using HCW equations, choosing the following weighting matrices,

$$\boldsymbol{Q} = \begin{bmatrix} \boldsymbol{I}_{3\times3} & \boldsymbol{0}_{3\times3} \\ \boldsymbol{0}_{3\times3} & \frac{1}{n^2}\boldsymbol{I}_{3\times3} \end{bmatrix}, \qquad \boldsymbol{R} = \frac{100}{n^4}\boldsymbol{I}_{3\times3}$$

Controllers performance were evaluated over two chief's orbit periods and simulations were performed using Simulink, choosing 4^{th} order Runge - Kutta integration algorithm with step size 60 s. Three indexes were used to compare the two con-

trollers:

- The norm of the difference between the position components of controlled NERM equations using both control laws, denoted here with $\boldsymbol{\rho}_{\mathrm{nl}}(t)$, and the position components of controlled LERM equations using control in Equation (4.2), denoted with $\boldsymbol{\rho}_{\mathrm{l}}(t)$.

$$\epsilon(t) = \|\boldsymbol{\rho}_{\mathrm{nl}}(t) - \boldsymbol{\rho}_{\mathrm{l}}(t)\|$$

- Total control usage.

$$\Delta v = \int_0^{t_f} u(t)\mathrm{d}t \tag{4.3}$$

- Integral time square error.

$$\mathrm{ITSE}^2 = \int_0^{t_f} t\rho(t)^2\mathrm{d}t$$

Tables 4.3, 4.4 and 4.5 resumes indexes values at the end of the simulations. Calibrated state shows better performance in almost all the simulations, in particular in those where orbits difference is significant. Linearization error and total error at end of simulation are significantly lower than values shown by true state feedback control, as well as total control usage during the manoeuvre. In Figures 4.2 and 4.3 the trajectories of the deputy in the LVLH frame are shown. Calibrated state feedback law always converges to the origin, whereas sometimes true state feedback law is unstable and the deputy drifts away from the chief.

Table 4.3: Average ϵ and total control usage for $e = 0$.

Case	Average ϵ (km)		Δv (m/s)	
	True	Calibrated	True	Calibrated
$\delta e = 0.01$, $\delta i = 0.01$ rad	6.26	1.03	61.45	61.87
$\delta e = 0.1$, $\delta i = 0.1$ rad	905.52	109.16	813.37	625.37
$\delta e = 0.2$, $\delta i = 0.2$ rad	11 359.53	467.96	46 680.29	1281.33
$\delta\Omega = \delta\omega = 0.01$ rad	7.38	2.02	47.26	46.59
$\delta\Omega = \delta\omega = 0.1$ rad	727.68	197.93	603.46	466.35
$\delta\Omega = \delta\omega = 0.2$ rad	8020.57	768.57	22 913.54	944.34

Table 4.4: Average ϵ and total control usage for $e = 0.3$.

Case	Average ϵ (km)		Δv (m/s)	
	True	Calibrated	True	Calibrated
$\delta e = 0.01$, $\delta i = 0.01$ rad	7.20	1.11	77.30	77.67
$\delta e = 0.1$, $\delta i = 0.1$ rad	2382.11	118.97	5846.52	781.07
$\delta e = 0.2$, $\delta i = 0.2$ rad	16 767.48	522.45	91 568.89	1579.97
$\delta\Omega = \delta\omega = 0.01$ rad	8.67	1.62	48.08	47.11
$\delta\Omega = \delta\omega = 0.1$ rad	852.90	157.41	676.12	471.45
$\delta\Omega = \delta\omega = 0.2$ rad	10 769.91	606.58	47 615.82	950.75

Table 4.5: ITSE^2 final values.

Case	$e = 0$		$e = 0.3$	
	True	Calibrated	True	Calibrated
$\delta e = 0.01$, $\delta i = 0.01$ rad	$1.1568 \cdot 10^{12}$	$\mathbf{1.1501 \cdot 10^{12}}$	$1.2605 \cdot 10^{12}$	$\mathbf{1.2031 \cdot 10^{12}}$
$\delta e = 0.1$, $\delta i = 0.1$ rad	$4.1329 \cdot 10^{14}$	$\mathbf{1.1629 \cdot 10^{14}}$	$4.3351 \cdot 10^{15}$	$\mathbf{1.1068 \cdot 10^{14}}$
$\delta e = 0.2$, $\delta i = 0.2$ rad	$1.1683 \cdot 10^{17}$	$\mathbf{4.8419 \cdot 10^{14}}$	$2.3792 \cdot 10^{17}$	$\mathbf{3.9988 \cdot 10^{14}}$
$\delta\Omega = \delta\omega = 0.01$ rad	$\mathbf{7.5394 \cdot 10^{11}}$	$7.8832 \cdot 10^{11}$	$\mathbf{1.3215 \cdot 10^{12}}$	$1.4538 \cdot 10^{12}$
$\delta\Omega = \delta\omega = 0.1$ rad	$1.3223 \cdot 10^{14}$	$\mathbf{8.0706 \cdot 10^{13}}$	$1.5075 \cdot 10^{14}$	$\mathbf{1.4935 \cdot 10^{14}}$
$\delta\Omega = \delta\omega = 0.2$ rad	$5.1240 \cdot 10^{16}$	$\mathbf{3.3545 \cdot 10^{14}}$	$8.1872 \cdot 10^{16}$	$\mathbf{6.0972 \cdot 10^{14}}$

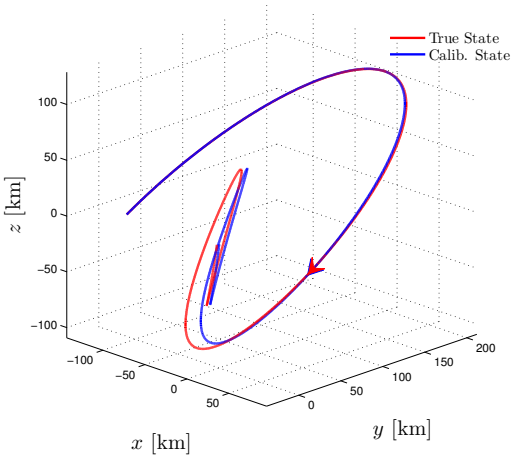

(a) $\delta e = 0.01$, $\delta i = 0.01$ rad.

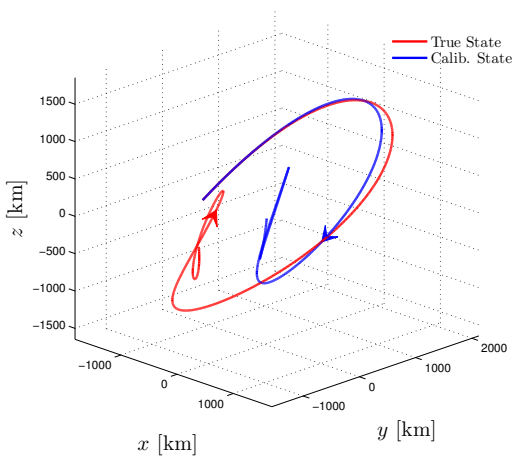

(b) $\delta e = 0.1$, $\delta i = 0.1$ rad.

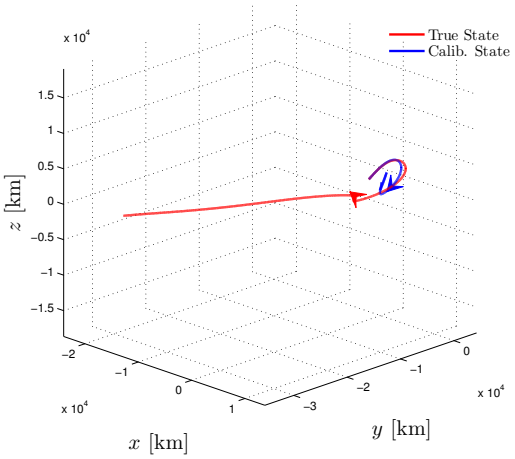

(c) $\delta e = 0.2$, $\delta i = 0.2$ rad.

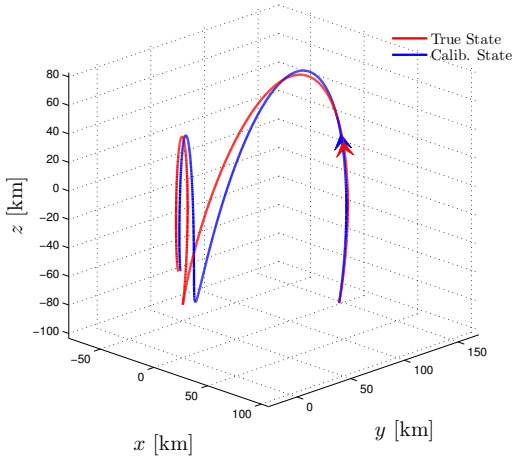

(d) $\delta\Omega = \delta\omega = 0.01$ rad.

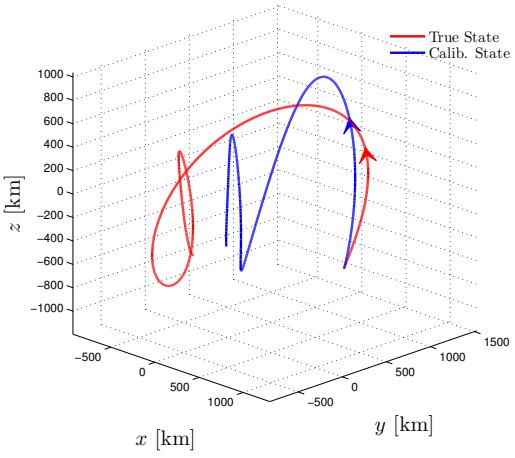

(e) $\delta\Omega = \delta\omega = 0.1$ rad.

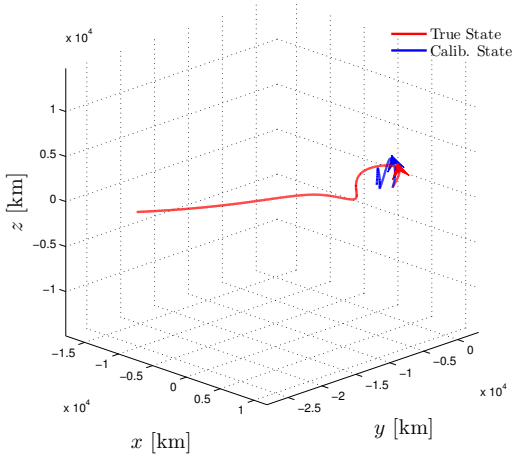

(f) $\delta\Omega = \delta\omega = 0.2$ rad.

Figure 4.2: True state and calibrated state feedback, trajectories for $e = 0$.

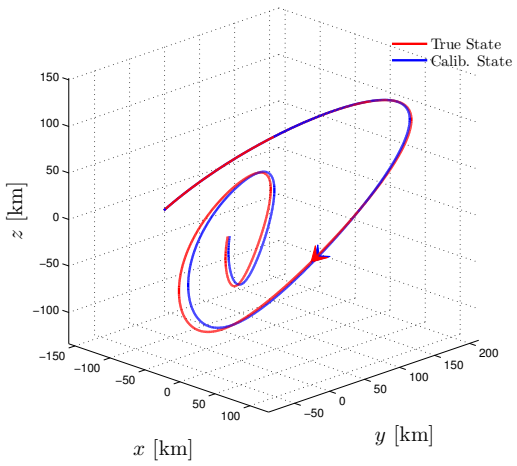

(a) $\delta e = 0.01$, $\delta i = 0.01$ rad.

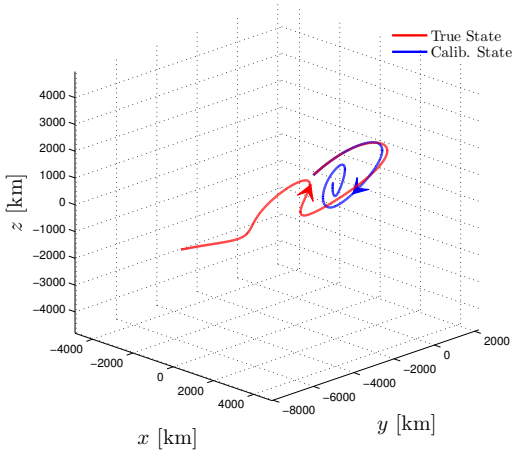

(b) $\delta e = 0.1$, $\delta i = 0.1$ rad.

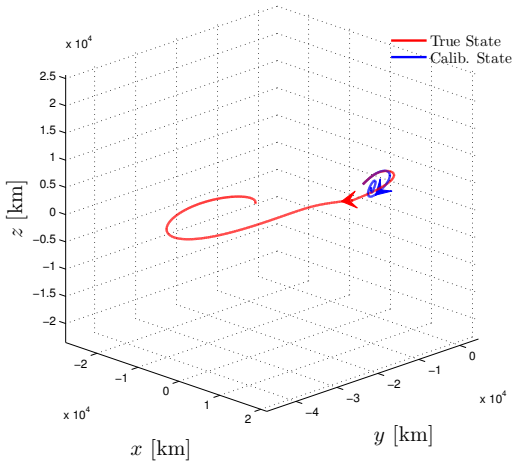

(c) $\delta e = 0.2$, $\delta i = 0.2$ rad.

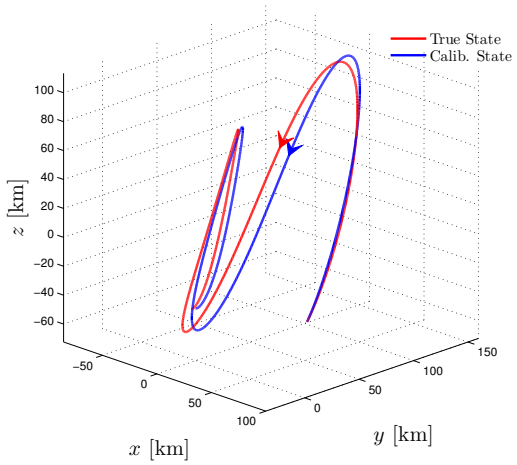

(d) $\delta\Omega = \delta\omega = 0.01$ rad.

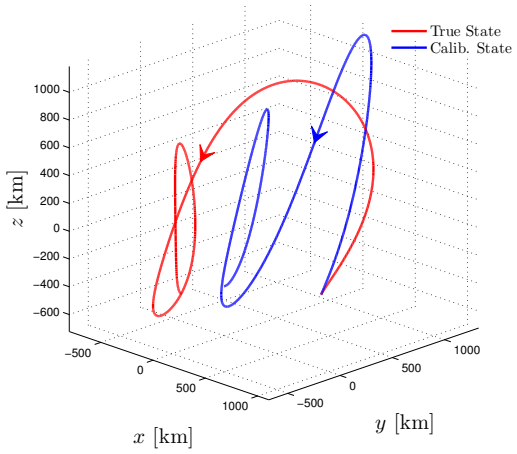

(e) $\delta\Omega = \delta\omega = 0.1$ rad.

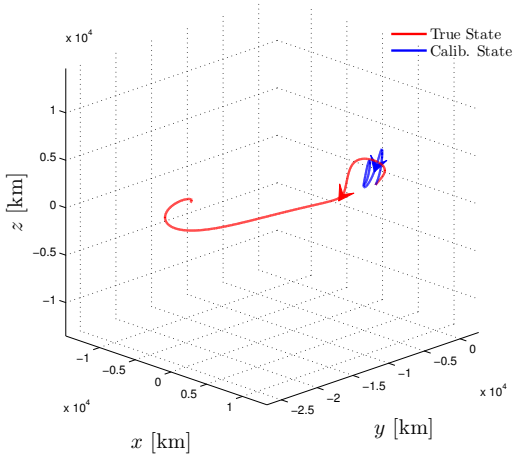

(f) $\delta\Omega = \delta\omega = 0.2$ rad.

Figure 4.3: True state and calibrated state feedback, trajectories for $e = 0.3$.

Chapter 5

State-Dependent Riccati Equation Control

The State-Dependent Riccati Equation Control technique (SDRE) is one of the most powerful and systematic approach for nonlinear systems sub-optimal controller design. The method is based on the extended linearization process, that transforms a nonlinear system into a linear-like form. Then, the linear quadratic regulator control law is mimicked in order to compute a sub-optimal feedback control law. The SDRE control was born in the late 90s and was applied with success in a lot of different fields, including advanced guide law development, satellite and spacecraft control, process control, robotics and cybernetics. Moreover, the extended linearization technique may be used as a starting point for the development of new nonlinear controllers. Linear control techniques may be used on the linearized equations, resulting in a nonlinear control law.

In this chapter the SDRE method is presented. Stability and optimality of SDRE controllers are also discussed, as well as control implementation and issues. The chapter ends with a presentation of some of the SDRE-based solutions proposed so far for the relative motion problem.

5.1 Problem Statement

Consider a system nonlinear in the state and affine in the input having dynamics

$$\boldsymbol{x} = \boldsymbol{f}(\boldsymbol{x}) + \boldsymbol{g}(\boldsymbol{x})\boldsymbol{u} \tag{5.1}$$

where $\boldsymbol{x} \in \mathbb{R}^n$ is the state, $\boldsymbol{u} \in \mathbb{R}^m$ is the input vector, $\boldsymbol{f} : \mathbb{R}^n \to \mathbb{R}^n$ and $\boldsymbol{g} : \mathbb{R}^n \to \mathbb{R}^{n\times m}$, such that $\boldsymbol{g}(\boldsymbol{x}) \neq \boldsymbol{0}\ \forall \boldsymbol{x} \in \mathbb{R}^n$, and a cost function

$$J(\boldsymbol{x}, \boldsymbol{u}) = \lim_{t\to+\infty} \int_0^t \Big[\boldsymbol{x}^T \boldsymbol{Q}(\boldsymbol{x})\boldsymbol{x} + \boldsymbol{u}^T \boldsymbol{R}(\boldsymbol{x})\boldsymbol{u}\Big] \mathrm{d}\tau \tag{5.2}$$

where $\boldsymbol{Q} : \mathbb{R}^n \to \mathbb{R}^{n\times n}$ is the state weighting matrix, that may be factored as $\boldsymbol{Q}(\boldsymbol{x}) = \boldsymbol{C}^T(\boldsymbol{x})\boldsymbol{C}(\boldsymbol{x})$, and $\boldsymbol{R} : \mathbb{R}^n \to \mathbb{R}^{m\times m}$ is the input weighting matrix.

Suppose then that $\boldsymbol{f}(\boldsymbol{x})$ is, at least, a continuous mapping in a bounded open set $\Omega \subseteq \mathbb{R}^n$ containing the origin and the initial state $\boldsymbol{x}_0 = \boldsymbol{x}(0)$ (i.e. $\boldsymbol{f} \in \mathcal{C}^k(\Omega)$, $k \geq 0$) and that the same holds for the matrix-valued functions $\boldsymbol{g}(\boldsymbol{x})$, $\boldsymbol{Q}(\boldsymbol{x})$, and $\boldsymbol{R}(\boldsymbol{x})$.

A stabilizing feedback control law

$$\boldsymbol{u}(\boldsymbol{x}) = \boldsymbol{k}(\boldsymbol{x})$$

such that $\boldsymbol{k}(\boldsymbol{0}) = \boldsymbol{0}$ and $\boldsymbol{k} \in \mathcal{C}^1(\Omega)$ is then sought, that will approximately minimize the Equation (5.2) and drives the system to the origin $\forall \boldsymbol{x}_0 \in \Omega$. A possible control law is the following,

$$\boldsymbol{u}(\boldsymbol{x}) = -\boldsymbol{K}(\boldsymbol{x})\boldsymbol{x}$$

thanks to the assumption of continuity on $\boldsymbol{k}(\boldsymbol{x})$, where $\boldsymbol{K} : \mathbb{R}^n \to \mathbb{R}^{m\times n}$.

5.2 Extended Linearization

The *extended linearization* process aims at finding a linear-like factorization of a nonlinear system, through the definition of state-dependent coefficient (SDC) ma-

trices,

$$\dot{\boldsymbol{x}} = \boldsymbol{A}(\boldsymbol{x})\boldsymbol{x} + \boldsymbol{B}(\boldsymbol{x})\boldsymbol{u} \tag{5.3}$$

The following proposition guarantees the existence of an SDC parametrization for $\boldsymbol{f}(\boldsymbol{x})$ under proper conditions [57].

Proposition 1 (Çimen, 2010)**.** *Let* $\boldsymbol{f} : \Omega \to \mathbb{R}^n$ *be such that* $\boldsymbol{f}(\boldsymbol{0}) = \boldsymbol{0}$ *and* $\boldsymbol{f} \in \mathcal{C}^k(\Omega)$*,* $k \geq 1$*. Then for all* $\boldsymbol{x} \in \Omega$ *an SDC parametrization* $\boldsymbol{f}(\boldsymbol{x}) = \boldsymbol{A}(\boldsymbol{x})\boldsymbol{x}$ *always exits for some* $\boldsymbol{A} : \Omega \to \mathbb{R}^{n \times n}$*.*

Some of the linear system properties can be reformulated for the SDC representation (5.3).

Definition 1. The SDC representation (5.3) is a stabilizable (controllable) parametrization of the nonlinear system (5.1) in Ω if the pair $\big\{\boldsymbol{A}(\boldsymbol{x}), \boldsymbol{B}(\boldsymbol{x})\big\}$ is pointwise stabilizable (controllable) in the linear sense for all $\boldsymbol{x} \in \Omega$.

Definition 2. The SDC representation (5.3) is a detectable (observable) parametrization of the nonlinear system (5.1) in Ω if the pair $\big\{\boldsymbol{C}(\boldsymbol{x}), \boldsymbol{A}(\boldsymbol{x})\big\}$ is pointwise detectable (observable) in the linear sense for all $\boldsymbol{x} \in \Omega$.

It is worth of note that the parametrization is not unique when $n > 1$. This adds an important degree of freedom to the SDRE methodology. Given for example two different parametrization for $\boldsymbol{f}(\boldsymbol{x})$, an infinite number of SDC parametrization can be obtained,

$$\boldsymbol{A}(\boldsymbol{x}, \alpha) = \alpha \boldsymbol{A}_1(\boldsymbol{x}) + (1 - \alpha)\boldsymbol{A}_2(\boldsymbol{x}), \qquad \alpha \in [0, 1]$$

This flexibility may be exploited to achieve better performance or to satisfy specific design requirements. Usually the coefficient α is tuned to ensure the stabilizability (controllability) and the detectability (observability) of the parametrization over the domain of interest. The analysis of this two properties may be carried out using

the controllability matrix $\boldsymbol{M}_C(\boldsymbol{x})$,

$$\boldsymbol{M}_C(\boldsymbol{x}) = \left[\boldsymbol{B}(\boldsymbol{x}) \mid \boldsymbol{A}(\boldsymbol{x})\boldsymbol{B}(\boldsymbol{x}) \mid \ \ldots \ \mid \boldsymbol{A}^{n-1}(\boldsymbol{x})\boldsymbol{B}(\boldsymbol{x})\right]$$

and the observability matrix $\boldsymbol{M}_O(\boldsymbol{x})$,

$$\boldsymbol{M}_O(\boldsymbol{x}) = \left[\boldsymbol{C}^T(\boldsymbol{x}) \mid \boldsymbol{A}^T(\boldsymbol{x})\boldsymbol{C}^T(\boldsymbol{x}) \mid \ \ldots \ \mid (\boldsymbol{A}^T(\boldsymbol{x}))^{n-1}\boldsymbol{C}^T(\boldsymbol{x})\right]$$

The SDC representation will be stabilizable if $\text{rank}(\boldsymbol{M}_C(\boldsymbol{x})) \neq 0 \ \forall \boldsymbol{x} \in \Omega$ and will be detectable if $\text{rank}(\boldsymbol{M}_O(\boldsymbol{x})) \neq 0 \ \forall \boldsymbol{x} \in \Omega$. If $\boldsymbol{C}(\boldsymbol{x})$ is chosen positive-semidefinite $\forall \boldsymbol{x} \in \Omega$, then detectability is guaranteed.

The use of linear control methods on the SDC representation (5.3), treating $\boldsymbol{A}(\boldsymbol{x})$ and $\boldsymbol{B}(\boldsymbol{x})$ as constant matrices at each instant, takes the name of *extended linearization control method*.

5.3 SDRE Control Technique

One of the most widely diffused extended linearization control method is the state-dependent Riccati equation control technique. The nonlinear optimal regulation problem stated in Section 5.1 is characterized by a state-dependent linear quadratic cost function, that recall the linear quadratic regulator problem (LQR). Thus, mimicking the LQR technique, a controller can be designed that, at each sample time, computes a matrix gain $\boldsymbol{K}$ treating the SDC matrices as being constant.

Let be $\boldsymbol{f} \in \mathcal{C}^1(\Omega)$, $\boldsymbol{B}(\boldsymbol{x}) = \boldsymbol{g}(\boldsymbol{x}) \in \mathcal{C}^0(\Omega)$ and $\boldsymbol{B}(\boldsymbol{x}) \neq \boldsymbol{0} \ \forall \boldsymbol{x} \in \Omega$. Without loss of generality, let $\boldsymbol{x} = \boldsymbol{0} \in \Omega$ be an equilibrium of the system with $\boldsymbol{u} = \boldsymbol{0}$. Under this condition the system (5.1) has an SDC representation (5.3) by Proposition 1.

An LQR-like state-feedback controller can be designed

$$\boldsymbol{u}(\boldsymbol{x}) = -\boldsymbol{R}^{-1}(\boldsymbol{x})\boldsymbol{B}^T(\boldsymbol{x})\boldsymbol{P}(\boldsymbol{x})\boldsymbol{x} \tag{5.4}$$

where $\boldsymbol{P}(\boldsymbol{x})$ is the unique, symmetric, positive-definite and pointwise stabilizing

solution of the continuous-time *State-Dependent Riccati Equation* (SDRE),

$$\boldsymbol{A}^T(\boldsymbol{x})\boldsymbol{P}(\boldsymbol{x}) + \boldsymbol{P}(\boldsymbol{x})\boldsymbol{A}(\boldsymbol{x}) - \boldsymbol{P}(\boldsymbol{x})\boldsymbol{B}(\boldsymbol{x})\boldsymbol{R}^{-1}(\boldsymbol{x})\boldsymbol{B}^T(\boldsymbol{x})\boldsymbol{P}(\boldsymbol{x}) + \boldsymbol{Q}(\boldsymbol{x}) = \boldsymbol{0} \qquad (5.5)$$

under the following assumptions:

1) The state and input weighting matrices are continuous and symmetric matrix-valued functions, such that $\boldsymbol{Q}(\boldsymbol{x}) \geq \boldsymbol{0}$ (positive-semidefinite) and $\boldsymbol{R}(\boldsymbol{x}) > \boldsymbol{0}$ (positive-definite) $\forall \boldsymbol{x} \in \Omega$.

2) The SDC representation is stabilizable and detectable in Ω.

SDRE control is therefore a generalization of the LQR problem, and it collapse to this when the coefficient and weighting matrices are constant. The resolution of an algebraic Riccati equation (ARE) simplify the implementation of the controller and avoid the resolution of the Hamilton-Jacobi-Bellman equation.

5.4 Stability of SDRE control

Local asymptotic stability of the SDRE control can be proved by means of the following theorem, developed by Mracek et al. in [58].

Theorem 1 (Mracek & Cloutier, 1998)**.** *Consider the nonlinear system* (5.1) *with feedback control* (5.4) *applied, where* $\boldsymbol{x} \in \mathbb{R}^n$ *with* $n > 1$ *and* $\boldsymbol{P}(\boldsymbol{x})$ *is the unique, symmetric, positive-definite and pointwise stabilizing solution of the SDRE* (5.5)*. Then, if* (5.3) *is a stabilizable and detectable SDC parametrization such that* $\boldsymbol{A}(\boldsymbol{x})$*,* $\boldsymbol{B}(\boldsymbol{x})$*,* $\boldsymbol{Q}(\boldsymbol{x})$ *and* $\boldsymbol{R}(\boldsymbol{x})$ *are* $\mathcal{C}^1(\mathbb{R}^{\boldsymbol{n}})$ *matrix-valued functions, the SDRE control technique produces a closed-loop solution which is locally asymptotically stable.*

However, the asymptotic stability is limited to a neighbourhood of the origin. Global asymptotic stability can be proved only for two particular cases by the following theorems, proposed in [59].

Theorem 2 (Cloutier, D'Souza & Mracek, 1996)**.** *If the closed-loop coefficient matrix* $\boldsymbol{A}_{CL}(\boldsymbol{x}) = \boldsymbol{A}(\boldsymbol{x}) - \boldsymbol{B}(\boldsymbol{x})\boldsymbol{K}(\boldsymbol{x})$ *is symmetric for all* $\boldsymbol{x}$*, then if* (5.3) *is a*

stabilizable and detectable SDC parametrization such that $\boldsymbol{A}(\boldsymbol{x})$, $\boldsymbol{B}(\boldsymbol{x})$, $\boldsymbol{Q}(\boldsymbol{x})$ *and* $\boldsymbol{R}(\boldsymbol{x})$ *are* $\mathcal{C}^1(\mathbb{R}^{\boldsymbol{n}})$ *matrix-valued functions, the SDRE closed-loop solution is globally asymptotically stable.*

Theorem 3 (Cloutier, D'Souza & Mracek, 1996)**.** *In the scalar case* $n = 1$ *the SDRE closed-loop solution is globally asymptotically stable.*

Extension of Theorem 3 to higher order systems is possible but under strong conditions (see in [59] and references therein).

Alternatively to global stability, it is desirable to estimate the stability region for the system, i.e. the *region of attraction* (ROA). A powerful approach to the systematic estimation of the ROA is proposed by Bracci et al. in [60]:

1) Consider the autonomous system $\dot{\boldsymbol{x}} = \boldsymbol{f}(\boldsymbol{x})$ and suppose the origin is an equilibrium (otherwise translate the state variables). Linearize the system in the neighbourhood of the origin obtaining the following matrix.

$$\boldsymbol{A} = \frac{\partial \boldsymbol{f}}{\partial \boldsymbol{x}}\Big|_{\boldsymbol{x}=\boldsymbol{0}}$$

2) If $\boldsymbol{A}$ is Hurwitz (i.e all its eigenvalues are in the open left half complex plane) find a Lyapunov function for the system

$$V(\boldsymbol{x}) = \boldsymbol{x}^T P \boldsymbol{x}$$

using the Lyapunov equation

$$\boldsymbol{A}^T \boldsymbol{P} + \boldsymbol{P}\boldsymbol{A} = -\boldsymbol{Q}$$

where $\boldsymbol{Q}$ must be chosen positive-definite.

3) Derive $V(\boldsymbol{x})$ obtaining

$$\dot{V}(\boldsymbol{x}) = 2\boldsymbol{x}^T \boldsymbol{P} \boldsymbol{f}(\boldsymbol{x})$$

and find the state-space region L defined as follows.

$$L = \left\{ \boldsymbol{x} \in \mathbb{R}^n \mid \dot{V}(\boldsymbol{x}) < 0 \right\}$$

4) Find the lowest value $\overline{V}$ such that $\dot{V}(\boldsymbol{x}) \geq 0$

$$\overline{V} = \inf_{\boldsymbol{x} \in \{\mathbb{R}^n - L\}} V(\boldsymbol{x})$$

and the highest value V_M, such that the corresponding level set is entirely inside L.

$$V_M = \sup_{V(\boldsymbol{x}) \leq V_M} V(\boldsymbol{x})$$

5) The connected area

$$E = \left\{ \boldsymbol{x} \in \mathbb{R}^n \mid V(\boldsymbol{x}) \leq V_M \right\}$$

belongs to the ROA according to the Lyapunov theorem for local stability.

The algorithm can be easily extended to a system controlled using SDRE technique, after computing the closed-loop system matrix $\boldsymbol{A}_{\mathrm{CL}}(\boldsymbol{x})$. If $\boldsymbol{K}(\boldsymbol{x})$ is not available in closed form, then the state-dependent Riccati equation (5.5) must be computed pointwise in order to obtain $\boldsymbol{A}_{\mathrm{CL}}(\boldsymbol{x})$, during the evaluation of L.

5.5 Optimality of SDRE Control

As the state $\boldsymbol{x}$ is driven to the origin, $\boldsymbol{A}(\boldsymbol{x}) \to \frac{\partial \boldsymbol{f}(\mathbf{0})}{\partial \boldsymbol{x}}$ and the solution of the state-dependent Riccati equation, $\boldsymbol{P}(\boldsymbol{x})$, tends to the solution of the ARE for the linearized problem at the origin. Thus, in a small neighbourhood of the origin the SDRE control law is arbitrary close to the optimal control law. The SDRE control method is therefore asymptotically optimal, since it converges to the optimal control law close to the origin as $\boldsymbol{x} \to \mathbf{0}$.

Some of the necessary conditions for optimality of the SDRE control law may be verified by the following theorem, presented in [58]. Recalling Pontryagin's max-

imum principle, these are,

$$\frac{\partial H}{\partial \boldsymbol{u}} = \mathbf{0} \tag{5.6a}$$

$$\dot{\boldsymbol{\lambda}} = -\frac{\partial H}{\partial \boldsymbol{x}} \tag{5.6b}$$

$$\dot{\boldsymbol{x}} = -\frac{\partial H}{\partial \boldsymbol{x}}$$

where H is the *Hamiltonian function* defined as

$$H = \frac{\partial V(\boldsymbol{x})}{\partial \boldsymbol{x}}^T \left(\boldsymbol{f}(\boldsymbol{x}) + \boldsymbol{g}(\boldsymbol{x})\boldsymbol{u}\right) + \frac{1}{2}\left(\boldsymbol{x}^T\boldsymbol{Q}(\boldsymbol{x})\boldsymbol{x} + \boldsymbol{u}^T\boldsymbol{R}(\boldsymbol{x})\boldsymbol{u}\right)$$

and $V(\boldsymbol{x})$ is the *value function* given by

$$V(\boldsymbol{x}) \triangleq \inf_{\boldsymbol{u}(\cdot)\in\mathcal{U}} J\left(\boldsymbol{x}, \boldsymbol{u}(\cdot)\right)$$

It is assumed that the SDC parametrization (5.3) is pointwise stabilizable and detectable for all $\boldsymbol{x}$, so that $\boldsymbol{P}(\boldsymbol{x})$ exists.

Theorem 4 (Mracek & Cloutier, 1998)**.** *In the general multi-variable case, $n > 1$, the SDRE nonlinear feedback solution and its associated state and costate trajectories satisfy the first necessary condition for optimality* (5.6a) *of the nonlinear optimal regulation problem defined by Equation* (5.1)-(5.2)*.*

Additionally, if $\boldsymbol{A}(\boldsymbol{x})$, $\boldsymbol{B}(\boldsymbol{x})$, $\boldsymbol{P}(\boldsymbol{x})$, $\boldsymbol{Q}(\boldsymbol{x})$ and $\boldsymbol{R}(\boldsymbol{x})$ are bounded in a neighbourhood Ω about the origin along with their gradients, under asymptotic stability as the state $\boldsymbol{x}$ is driven to zero the second necessary condition for optimality (5.6b) *is asymptotically satisfied at a quadratic rate.*

This theorem represent a sub-optimality property of the SDRE method, since the second necessary condition for optimality is satisfied only asymptotically. Global optimality can be proved for scalar systems by the following theorem [58].

Theorem 5 (Mracek & Cloutier, 1998)**.** *For scalar system, $n = 1$, the globally asymptotically stabilizing SDRE feedback solution of the nonlinear optimal regulator*

problem defined by Equation (5.1)-(5.2) *is always globally optimal in* $\mathbb{R}^1$.

Global optimality in case of multi-variable systems cannot be proved. Huang and Lu in [61] proved that an SDC representation always exists such that the SDRE control law produces the optimal feedback control law (see also [62] and references therein). Nevertheless there are no methods that identify the "optimal" SDC representation, to the best of the author's knowledge.

5.6 Algebraic Riccati Equation Online Resolution

The resolution of the ARE at each sampling time is the most expensive step in terms of computational resources. Several methods were proposed during the years, that may be categorized in two classes: *direct* and *iterative methods*. The former class returns an exact solution at each execution, whereas the latter, starting from an initial guess, compute an approximate solution through consecutive iterations and are usually faster.

ARE solution can be computed using the correspondent *Hamiltonian matrix*,

$$\boldsymbol{H} = \begin{bmatrix} \boldsymbol{A} & -\boldsymbol{B}\boldsymbol{R}^{-1}\boldsymbol{B}^T \\ -\boldsymbol{Q} & -\boldsymbol{A}^T \end{bmatrix} \in \mathbb{R}^{2n\times 2n}$$

By similiarity transformation $\boldsymbol{H}$ can be written as

$$\boldsymbol{H} = \boldsymbol{T}\boldsymbol{\Lambda}\boldsymbol{T}^{-1} \tag{5.7}$$

where the first n columns of $\boldsymbol{T}$ are the eigenvectors relative to the eigenvalues of $\boldsymbol{H}$ with positive real part, whereas the second n columns are the eigenvectors relative to the eigenvalues with negative real part. $\boldsymbol{T}$ and $\boldsymbol{\Lambda}$ can then be factorized as follows,

$$\boldsymbol{\Lambda} = \begin{bmatrix} \boldsymbol{\Lambda}_+ & \boldsymbol{0}_{n\times n} \\ \boldsymbol{0}_{n\times n} & \boldsymbol{\Lambda}_- \end{bmatrix}, \qquad \boldsymbol{T} = \begin{bmatrix} \boldsymbol{T}_+ & \boldsymbol{T}_- \end{bmatrix} = \begin{bmatrix} \boldsymbol{T}_{11} & \boldsymbol{T}_{12} \\ \boldsymbol{T}_{21} & \boldsymbol{T}_{22} \end{bmatrix}$$

The ARE solution is then given by

$$\boldsymbol{P} = \boldsymbol{T}_{22}\boldsymbol{T}_{12}^{-1}$$

The Hamiltonian matrix may be balanced before computing the similiarity transformation in Equation (5.7), for example using the algorithm proposed in [63], Section 11.6.1. The balanced Hamiltonian matrix $\boldsymbol{H}_b$ is given by

$$\boldsymbol{H} = \boldsymbol{D}\boldsymbol{H}_b\boldsymbol{D}^{-1} \tag{5.8}$$

where $\boldsymbol{D}$ is the transformation matrix computed by the balancing process. Transformation in Equation (5.7) can be applied to $\boldsymbol{H}_b$,

$$\boldsymbol{H}_b = \boldsymbol{T}_b\boldsymbol{\Lambda}\boldsymbol{T}_b^{-1} \tag{5.9}$$

Introducing Equation (5.9) in Equation (5.8) gives

$$\boldsymbol{T} = \boldsymbol{D}\boldsymbol{T}_b$$

A more robust direct numerical procedure is based on the *Schur decomposition* of the Hamiltonian matrix,

$$\boldsymbol{H} = \boldsymbol{U}^T\boldsymbol{L}\boldsymbol{U}, \quad \boldsymbol{L} = \begin{bmatrix} \boldsymbol{L}_{11} & \boldsymbol{L}_{12} \\ \boldsymbol{L}_{21} & \boldsymbol{L}_{22} \end{bmatrix}$$

where $\boldsymbol{L}$ is the Schur form of $\boldsymbol{H}$, with $\boldsymbol{L}_{11}$ possessing all negative real part eigenvalues, and the matrix $\boldsymbol{U}$ is orthogonal. The solution of the Riccati equation in this case is given by

$$\boldsymbol{P} = \boldsymbol{U}_{12}^T\left(\boldsymbol{U}_{11}^{-1}\right)^T$$

An approximate estimate of the computational cost of Schur method is given in [64]. Solution is found in approximately $75n^3$ floating point operations.

Among the iterative methods, the most famous is the *Kleinman algorithm* [65], that uses an initial guess of the closed gain to compute $\boldsymbol{P}$.

Let $\boldsymbol{K}_0$ be such that the closed loop system $\left(\boldsymbol{A}+\boldsymbol{B}\boldsymbol{K}_0^T\right)$ has all eigenvalues with negative real parts. Then, $\boldsymbol{P}_i$ and $\boldsymbol{K}_i$ are defined recursively by

$$\boldsymbol{P}_i\left(\boldsymbol{A}+\boldsymbol{B}\boldsymbol{K}_i^T\right)+\left(\boldsymbol{A}+\boldsymbol{B}\boldsymbol{K}_i^T\right)^T\boldsymbol{P}_i=-\boldsymbol{K}_i\boldsymbol{R}\boldsymbol{K}_i^T-\boldsymbol{Q}$$

$$\boldsymbol{K}_{i+1}=-\boldsymbol{P}_i\boldsymbol{B}\boldsymbol{R}^{-1}$$

It can be proved that $\lim_{i\to+\infty}\boldsymbol{P}_i=\boldsymbol{P}$ and that $\|\boldsymbol{P}_{i+1}-\boldsymbol{P}\|\leq c\,\|\boldsymbol{P}_i-\boldsymbol{P}\|^2$ with $c>0$. Therefore, the convergence of the algorithm is quadratic. The Kleinman algorithm requires $6n^3$ floating point operations per iteration and, depending upon the initial guess, 10 or more iterations may be required to converge to the solution.

Initial guess for $\boldsymbol{K}_0$ can be generated, for example, using pole placement. Alternately, Schur algorithm can be used to obtain a first estimation of $\boldsymbol{P}$ and the algorithm can start from $\boldsymbol{K}_0=-\boldsymbol{P}_0\boldsymbol{B}\boldsymbol{R}^{-1}$.

Further information about algorithms for ARE resolution and their computational costs can be found in [66] and references therein.

5.7 Existing SDRE Controllers for Relative Motion

SDRE control was recently proposed for relative motion problem, even if the first example of control for both attitude and position is dated 2000 [67]. The control technique was applied principally for formation flying control. Park et al. in [68] consider formation reconfiguration and station-keeping maneuvers. J_2 perturbation is taken in account and it is computed using deputy's orbital elements. Massari et al. in [69] apply, again, the SDRE method for formation flying and state estimation. Moreover, collision avoidance between the two satellites is considered and the relative constraint is introduced in the system dynamics equations. Other SDRE applications on formation flying are proposed in [70–72].

Autonomous rendezvous and docking operation is considered in [73]. The SDRE

controller was tested on real hardware, using a testbed developed by DLR. In [74, 75] Lee et al. study the relative attitude and position control of a spacecraft approaching the International Space Station. Atmospheric drag and J_2 perturbations were considered.

Often the proposed solutions do not consider deputy's mass variation due to propellant consumption. This aspect is not negligible when the maneuver covers long distances. Moreover, satellite's mass variation should be considered also in the inertia tensor, if relative attitude control problem is considered. Also limitations on control are usually not taken in account.

Chapter 6

SDRE Control of Relative Motion

In this chapter the SDRE method is applied to develop controllers for nonlinear equation of relative unperturbed motion. Three different parametrization were developed and tested. The tools of the SDRE method were used in order to rewrite the state-independent parameters, also known as bias terms.

In the first parametrization, bias terms were reformulated and included in the SDC matrices. In the second one, a fictitious state was introduced and the in-plane and out-of-plane motion were decoupled, resulting in two different systems to control. The third parametrization was developed introducing a first control law that dynamically cancels bias terms, in a computed torque fashion. Again the in-plane and out-plane components were decoupled, resulting in a time-varying and a time-invariant systems to control.

The developed SDRE controllers were then compared to calibrated state feedback control law presented in Chapter 4. Different tests were performed, in order to analyse and improve controls performances, introducing also satellite mass variation due to propellant consumption into the SDC parametrizations.

6.1 SDC Parametrization of NERM

6.1.1 Existence of SDC Parametrizations

Nonlinear equation of relative motion in the unperturbed case can be easily rewritten in control affine form

$$\dot{\boldsymbol{x}} = \boldsymbol{f}(\boldsymbol{x}) + \boldsymbol{g}(\boldsymbol{x})\boldsymbol{u}$$

where $\boldsymbol{f}(\boldsymbol{x}) : \mathbb{R}^n \to \mathbb{R}^n$ and $\boldsymbol{g}(\boldsymbol{x}) : \mathbb{R}^n \to \mathbb{R}^n$ have the following expressions,

$$\boldsymbol{f}(\boldsymbol{x}) = \begin{bmatrix} \dot{x} \\ \dot{y} \\ \dot{z} \\ 2\dot{f}\left(\dot{y} - y\frac{\dot{r}}{r}\right) + x\dot{f}^2 - \frac{\mu}{r_d^3}(r+x) + \frac{\mu}{r^2} \\ -2\dot{f}\left(\dot{x} - x\frac{\dot{r}}{r}\right) + y\dot{f}^2 - \frac{\mu}{r_d^3}y \\ -\frac{\mu}{r_d^3}z \end{bmatrix}, \qquad \boldsymbol{g}(\boldsymbol{x}) = \begin{bmatrix} \boldsymbol{0}_{3\times 3} \\ \boldsymbol{I}_{3\times 3} \end{bmatrix}$$

Since $\boldsymbol{f}(\boldsymbol{0}) = \boldsymbol{0}$, extended linearization of NERM equations is possible by Proposition 1, even though the fourth element of $\boldsymbol{f}(\boldsymbol{x})$, Equation (2.25a), presents what it may be called (abusing of SDRE terminology) a bias term,

$$\frac{\mu}{r^2} - \frac{\mu}{r_d^3}r \tag{6.1}$$

Formally, in the SDRE literature a *bias term* is a state-independent term which cause the violation of the requirement $\boldsymbol{f}(\boldsymbol{0}) = \boldsymbol{0}$. In this case, the term (6.1) does not cause the violation of the before mentioned requirement, since r_d is state-dependent (remember that $r_d = \sqrt{(r+x)^2 + y^2 + z^2}$) and it is equal to r when $\boldsymbol{x} = \boldsymbol{0}$. Nevertheless, an explicit state-dependent expression must be found in order to obtain the SDC matrices. Different expressions may be proposed, that lead to different SDRE controllers.

6.1.2 Parametrization 1

An explicit linear dependence from the state $\boldsymbol{x}$ of the term (6.1) can be found after some mathematical manipulations,

$$\begin{aligned}
\mu\left(\frac{1}{r^2}-\frac{r}{r_d^3}\right) &= \mu\frac{r_d^3-r^3}{r^2r_d^3} \\
&= \mu\frac{(r_d-r)(r_d^2+rr_d+r^2)}{r^2r_d^3} \\
&= \mu\frac{(r_d^2-r^2)(r_d^2+rr_d+r^2)}{(r_d+r)r^2r_d^3} \\
&= \mu\frac{((r+x)^2+y^2+z^2-r^2)(r_d^2+rr_d+r^2)}{(r_d+r)r^2r_d^3} \\
&= \mu\frac{((2r+x)x+y^2+z^2)(r_d^2+rr_d+r^2)}{(r_d+r)r^2r_d^3} \\
&= \gamma(2r+x)x+\gamma y^2+\gamma z^2
\end{aligned} \tag{6.2}$$

In the previous expression it was introduced the time-variant parameter γ, which was defined as,

$$\gamma \triangleq \mu\frac{r_d^2+rr_d+r^2}{(r_d+r)r^2r_d^3}$$

The SDC matrices are then

$$\boldsymbol{A}(\boldsymbol{x}) = \begin{bmatrix}
0 & 0 & 0 & 1 & 0 & 0 \\
0 & 0 & 0 & 0 & 1 & 0 \\
0 & 0 & 0 & 0 & 0 & 1 \\
\dot{f}^2-\frac{\mu}{r_d^3}+\gamma(2r+x) & -2\dot{f}\frac{\dot{r}}{r}+\gamma y & \gamma z & 0 & 2\dot{f} & 0 \\
2\dot{f}\frac{\dot{r}}{r} & \dot{f}^2-\frac{\mu}{r_d^3} & 0 & -2\dot{f} & 0 & 0 \\
0 & 0 & -\frac{\mu}{r_d^3} & 0 & 0 & 0
\end{bmatrix} \quad \boldsymbol{B} = \begin{bmatrix} \boldsymbol{0}_{3\times3} \\ \boldsymbol{I}_{3\times3} \end{bmatrix}$$

This SDC representation is a stabilizable (and controllable) parametrization of the system, since the controllability matrix has rank 6, as can be proved by computing

its first columns,

$$\det\left[\boldsymbol{B} \mid \boldsymbol{A}(\boldsymbol{x})\boldsymbol{B}\right] = \det\left[\begin{array}{ccc|ccc} 0 & 0 & 0 & 1 & 0 & 0 \\ 0 & 0 & 0 & 0 & 1 & 0 \\ 0 & 0 & 0 & 0 & 0 & 1 \\ 1 & 0 & 0 & 0 & 2\dot{f} & 0 \\ 0 & 1 & 0 & -2\dot{f} & 0 & 0 \\ 0 & 0 & 1 & 0 & 0 & 0 \end{array}\right] = -1$$

The SDC matrices here found were already proposed in literature [69, 70].

6.1.3 Parametrization 2

Instead of writing the term (6.1) as a linear function of the state, it can be introduced a fictitious stable state ξ with a slow dynamic, for example $\dot{\xi} = -\lambda\xi$. Then Equation (2.25a) can be written as

$$\ddot{x} = \left(\dot{f}^2 - \frac{\mu}{r_d^3}\right) x - 2\dot{f}\frac{\dot{r}}{r} y + 2\dot{f}\dot{y} + \left(\frac{\mu}{r^2} - \frac{\mu}{r_d^3} r\right) \frac{1}{\xi} \cdot \xi + u_x$$

Introducing the extended state $\tilde{\boldsymbol{x}} = [x, y, z, \dot{x}, \dot{y}, \dot{z}, \xi]^T$, the SDC matrices are

$$\boldsymbol{A}(\tilde{\boldsymbol{x}}) = \begin{bmatrix} 0 & 0 & 0 & 1 & 0 & 0 & 0 \\ 0 & 0 & 0 & 0 & 1 & 0 & 0 \\ 0 & 0 & 0 & 0 & 0 & 1 & 0 \\ \dot{f}^2 - \frac{\mu}{r_d^3} & -2\dot{f}\frac{\dot{r}}{r} & 0 & 0 & 2\dot{f} & 0 & \left(\frac{\mu}{r^2} - \frac{\mu}{r_d^3} r\right)\frac{1}{\xi} \\ 2\dot{f}\frac{\dot{r}}{r} & \dot{f}^2 - \frac{\mu}{r_d^3} & 0 & -2\dot{f} & 0 & 0 & 0 \\ 0 & 0 & -\frac{\mu}{r_d^3} & 0 & 0 & 0 & 0 \\ 0 & 0 & 0 & 0 & 0 & 0 & -\lambda \end{bmatrix} \quad \boldsymbol{B} = \begin{bmatrix} \boldsymbol{0}_{3\times 3} \\ \boldsymbol{I}_{3\times 3} \\ \boldsymbol{0}_{1\times 3} \end{bmatrix}$$

This parametrization decouples the motion into the in-plane, $\tilde{\boldsymbol{x}}_{ip} = [x, y, \dot{x}, \dot{y}, \xi]^T$, and the out-of-plane, $\tilde{\boldsymbol{x}}_{op} = [z, \dot{z}]^T$, components. Therefore, two different controllers can be designed: one that controls the in-plane motion through $\boldsymbol{u}_{ip} = [u_x, u_y]^T$ and

the other one that uses $u_{op} = u_z$ to control the out-of-plane motion.

The two motion components are characterized by the following SDC parametrizations.

$$\boldsymbol{A}_{ip}(\tilde{\boldsymbol{x}}_{ip}) = \begin{bmatrix} 0 & 0 & 1 & 0 & 0 \\ 0 & 0 & 0 & 1 & 0 \\ \dot{f}^2 - \frac{\mu}{r_d^3} & -2\dot{f}\frac{\dot{r}}{r} & 0 & 2\dot{f} & \left(\frac{\mu}{r^2} - \frac{\mu}{r_d^3} r\right)\frac{1}{\xi} \\ 2\dot{f}\frac{\dot{r}}{r} & \dot{f}^2 - \frac{\mu}{r_d^3} & -2\dot{f} & 0 & 0 \\ 0 & 0 & 0 & 0 & -\lambda \end{bmatrix} \quad \boldsymbol{B}_{ip} = \begin{bmatrix} 0 & 0 \\ 0 & 0 \\ 1 & 0 \\ 0 & 1 \\ 0 & 0 \end{bmatrix}$$

$$\boldsymbol{A}_{op}(\tilde{\boldsymbol{x}}_{op}) = \begin{bmatrix} 0 & 1 \\ -\frac{\mu}{r_d^3} & 0 \end{bmatrix} \quad \boldsymbol{B}_{op} = \begin{bmatrix} 0 \\ 1 \end{bmatrix}$$

Proving the controllability of the out-of-plane motion is straightforward. The in-plane motion is not completely controllable, since the state ξ is not influenced by inputs or other controllable states. The remaining states are controllable and the SDC representation is thus stabilizable. The particular expression of the controllability matrix proves what already said. In particular its last row is null, as can be seen computing the first columns.

$$\left[\boldsymbol{B} \mid \boldsymbol{A}(\boldsymbol{x})\boldsymbol{B} \mid \boldsymbol{A}^2(\boldsymbol{x})\boldsymbol{B}\right] = \left[\begin{array}{cc|cc|cc} 0 & 0 & 1 & 0 & 0 & 2\dot{f} \\ 0 & 0 & 0 & 1 & -2\dot{f} & 0 \\ 1 & 0 & 0 & 2\dot{f} & -3\dot{f}^2 - \frac{\mu}{r_d^3} & -2\dot{f}\frac{\dot{r}}{r} \\ 0 & 1 & -\dot{f} & 0 & 2\dot{f}\frac{\dot{r}}{r} & -3\dot{f}^2 - \frac{\mu}{r_d^3} \\ 0 & 0 & 0 & 0 & 0 & 0 \end{array}\right]$$

Considering the sub-matrix formed by the first four rows and columns, it can be shown that $\text{rank}(\boldsymbol{M}_C(\boldsymbol{x})) = 4$.

6.1.4 Parametrization 3

Controls expression can be chosen to dynamically cancel the nonlinear and bias terms of Equations (2.25), in a computed torque fashion.

In particular, introducing a new control vector

$$\boldsymbol{\tau} = \tau_x \hat{\boldsymbol{i}} + \tau_y \hat{\boldsymbol{j}} + \tau_z \hat{\boldsymbol{k}}$$

it can be chosen the following control vector

$$\begin{aligned} u_x &= \frac{\mu}{r_d^3}(r + x) - \frac{\mu}{r^2} + \tau_x \\ u_y &= \frac{\mu}{r_d^3} y + \tau_y \\ u_z &= \frac{\mu}{r_d^3} z + \tau_z \end{aligned}$$

that transforms the system in a set of linear time-varying equations,

$$\begin{aligned} \ddot{x} - 2\dot{f}\left(\dot{y} - y\frac{\dot{r}}{r}\right) - x\dot{f}^2 &= \tau_x \\ \ddot{y} + 2\dot{f}\left(\dot{x} - x\frac{\dot{r}}{r}\right) - y\dot{f}^2 &= \tau_y \\ \ddot{z} &= \tau_z \end{aligned}$$

Again, the in-plane and the out-of-plane motion are decoupled. Moreover, the system describing the out-of-plane motion is a linear time-invariant system (a double integrator). Once the states of the two systems are defined,

$$\boldsymbol{x}_{ip} = [\ x \quad y \quad \dot{x} \quad \dot{y}\ ]^T, \qquad \boldsymbol{x}_{op} = [\ z \quad \dot{z}\ ]^T$$

the SDC matrices are characterized by the following expressions.

$$\boldsymbol{A}_{ip}(\boldsymbol{x}_{ip}) = \begin{bmatrix} 0 & 0 & 1 & 0 \\ 0 & 0 & 0 & 1 \\ \dot{f}^2 & -2\dot{f}\frac{\dot{r}}{r} & 0 & 2\dot{f} \\ 2\dot{f}\frac{\dot{r}}{r} & \dot{f}^2 & -2\dot{f} & 0 \end{bmatrix} \qquad \boldsymbol{B}_{ip} = \begin{bmatrix} 0 & 0 \\ 0 & 0 \\ 1 & 0 \\ 0 & 1 \end{bmatrix}$$

$$\boldsymbol{A}_{op} = \begin{bmatrix} 0 & 1 \\ 0 & 0 \end{bmatrix} \qquad \boldsymbol{B}_{op} = \begin{bmatrix} 0 \\ 1 \end{bmatrix}$$

Prove of out-of-plane system controllability is straightforward. Controllability matrix of in-plane system has rank 4, since

$$\det\left[\boldsymbol{B}_{ip} \mid \boldsymbol{A}_{ip}(\boldsymbol{x}_{ip})\boldsymbol{B}_{ip}\right] = \det\left[\begin{array}{cc|cc} 0 & 0 & 1 & 0 \\ 0 & 0 & 0 & 1 \\ 1 & 0 & 0 & 2\dot{f} \\ 0 & 1 & -2\dot{f} & 0 \end{array}\right] = 1$$

6.2 Simulations Results

The parametrization proposed in the previous sections were used to develop three SDRE controllers. Their performance were compared setting up a terminal rendezvous mission scenario using the same test cases presented in Section 4.3 (see Tables 4.1 and 4.2). Simulations were developed in Simulink. Runge - Kutta 4^{th} order integration algorithm was used and sample time was set to $T/1000$. SDRE controllers were compared to calibrated state feedback control presented in Section 4.

Before starting the simulations, SDRE controllers weighting matrices coefficients were tuned in order to minimize propellant consumption. An automatic tuning procedure was set up to find an optimal combination of coefficients. The procedure simulates one of the test cases trying different coefficients combinations and simulation results are then compared.

Several simulations were performed in order to analyse the controller performances. During the first set of simulations, in the following referred to as *Test 1*, controllers performance were evaluated over two orbital periods. In particular, total control usage, Equation (4.3), and final distance values were used to compare the controllers. The automatic tuning procedure found the following set of weighting matrices for the SDRE controllers,

$$\boldsymbol{Q}_1 = \begin{bmatrix} 6.5 \times 10^{-2}\boldsymbol{I}_{3\times3} & \boldsymbol{0}_{3\times3} \\ \boldsymbol{0}_{3\times3} & 2.2 \times 10^{5}\boldsymbol{I}_{3\times3} \end{bmatrix}, \quad \boldsymbol{R}_1 = 3.7474 \times 10^{11}\boldsymbol{I}_{3\times3}$$

$$\boldsymbol{Q}_{2,ip} = \begin{bmatrix} 5 \times 10^{-4}\boldsymbol{I}_{2\times2} & \boldsymbol{0}_{2\times3} \\ \boldsymbol{0}_{3\times2} & \boldsymbol{0}_{3\times3} \end{bmatrix}, \quad \boldsymbol{R}_{2,ip} = 3.8 \times 10^{8}\boldsymbol{I}_{2\times2}$$

$$\boldsymbol{Q}_{2,op} = \begin{bmatrix} 2.5 \times 10^{-5} & 0 \\ 0 & 0 \end{bmatrix}, \quad \boldsymbol{R}_{2,op} = 5 \times 10^{7}$$

$$\boldsymbol{Q}_{3,ip} = \begin{bmatrix} 3 \times 10^{-6}\boldsymbol{I}_{2\times2} & \boldsymbol{0}_{2\times2} \\ \boldsymbol{0}_{2\times2} & 7\boldsymbol{I}_{2\times2} \end{bmatrix}, \quad \boldsymbol{R}_{3,ip} = 8 \times 10^{6}\boldsymbol{I}_{2\times2}$$

$$\boldsymbol{Q}_{3,op} = \begin{bmatrix} 4 \times 10^{-4} & 0 \\ 0 & 8 \end{bmatrix}, \quad \boldsymbol{R}_{3,op} = 1.5 \times 10^{6}$$

The number in the subscript denotes the parametrization. The weighting matrices $\boldsymbol{Q}_{3,op}$ and $\boldsymbol{R}_{3,op}$ were used to compute an LQR controller for the out-of-plane component of parametrization 3.

Simulations results for this first set of tests are shown in Tables 6.1 and 6.2. SDRE controllers showed greater control usage than calibrated state feedback control. However, at the end of the simulations deputies that used SDRE controllers were significantly closer to the chief.

Therefore, a second set of tests was set up, *Test 2*, to understand time needed by deputies to converge to a condition suitable for a rendezvous and docking operation. Inspired by ESA's ATV docking, the deputy had to converge and to keep for 10 minutes the following conditions: $\rho < 20\,\mathrm{m}$, $\dot{\rho} < 0.01\,\mathrm{m/s}$. For this set of tests, total

Table 6.1: Test 1, total control usage Δv in m/s.

Test case	Calib.State	SDRE Par.1	SDRE Par.2	SDRE Par.3
		$e = 0$		
$\delta e = 0.01$, $\delta i = 0.01$ rad	62	164	288	228
$\delta e = 0.1$, $\delta i = 0.1$ rad	625	1662	3193	2370
$\delta e = 0.2$, $\delta i = 0.2$ rad	1281	3405	7435	4962
$\delta\Omega = \delta\omega = 0.01$ rad	47	118	233	419
$\delta\Omega = \delta\omega = 0.1$ rad	466	1221	2404	4207
$\delta\Omega = \delta\omega = 0.2$ rad	944	2550	4979	8350
		$e = 0.3$		
$\delta e = 0.01$, $\delta i = 0.01$ rad	78	155	287	263
$\delta e = 0.1$, $\delta i = 0.1$ rad	781	1546	3040	2764
$\delta e = 0.2$, $\delta i = 0.2$ rad	1579	3838	6401	5890
$\delta\Omega = \delta\omega = 0.01$ rad	47	121	187	303
$\delta\Omega = \delta\omega = 0.1$ rad	471	1221	1888	2939
$\delta\Omega = \delta\omega = 0.2$ rad	951	2486	3811	5656

Table 6.2: Test 1, final distance in m.

Test case	Calib.State	SDRE Par.1	SDRE Par.2	SDRE Par.3
		$e = 0$		
$\delta e = 0.01$, $\delta i = 0.01$ rad	3475.229	7.604	126.133	18.294
$\delta e = 0.1$, $\delta i = 0.1$ rad	61 823.227	79.601	1587.308	36.857
$\delta e = 0.2$, $\delta i = 0.2$ rad	215 477.251	164.680	4482.950	66.791
$\delta\Omega = \delta\omega = 0.01$ rad	42 533.259	5.478	54.624	18.983
$\delta\Omega = \delta\omega = 0.1$ rad	424 668.293	67.935	640.280	63.105
$\delta\Omega = \delta\omega = 0.2$ rad	850 265.047	167.139	1514.864	123.165
		$e = 0.3$		
$\delta e = 0.01$, $\delta i = 0.01$ rad	11 792.386	1.224	4.559	47.996
$\delta e = 0.1$, $\delta i = 0.1$ rad	91 268.430	16.498	51.356	48.520
$\delta e = 0.2$, $\delta i = 0.2$ rad	136 942.060	34.356	103.705	50.111
$\delta\Omega = \delta\omega = 0.01$ rad	35 152.162	1.063	0.496	48.015
$\delta\Omega = \delta\omega = 0.1$ rad	353 389.070	14.279	3.049	50.365
$\delta\Omega = \delta\omega = 0.2$ rad	709 117.474	38.512	11.747	56.938

control usage and total maneuver time (time needed to the deputy to converge to the docking condition) were used as performance indexes.

Results are shown in Tables 6.3 and 6.4. As can be seen, calibrate state feedback control law maneuver time is almost ten times greater than maneuver time needed by SDRE controllers. Moreover, calibrated state total control usage increased in this set of tests. As will be seen in Figures 6.1 and 6.2, Sinclair's control oscillates around the origin and need time to satisfy the docking condition, whereas SDRE controllers converge smoothly.

The previous SDRE controllers do not consider the mass variation due to propellant consumption. In the third set of tests, *Test 3*, mass was introduced in the control matrix $\boldsymbol{B}$ of the SDC parametrization, i.e. the new control matrix was $\boldsymbol{B}_{\mathrm{m}} = \frac{1}{m}\boldsymbol{B}$ (see Section 2.1.5). For parametrization 3, mass variation was introduced only in the in-plane motion control matrix. Convergence to docking condition was again considered. The following weighting matrices were found by the automatic tuning procedure,

$$\boldsymbol{Q}_1 = \begin{bmatrix} 6.5 \times 10^{-2}\boldsymbol{I}_{3\times3} & \boldsymbol{0}_{3\times3} \\ \boldsymbol{0}_{3\times3} & 2.7 \times 10^{5}\boldsymbol{I}_{3\times3} \end{bmatrix}, \quad \boldsymbol{R}_1 = 2.8 \times 10^{4}\boldsymbol{I}_{3\times3}$$

$$\boldsymbol{Q}_{2,ip} = \begin{bmatrix} 5.5 \times 10^{-1}\boldsymbol{I}_{2\times2} & \boldsymbol{0}_{2\times3} \\ \boldsymbol{0}_{3\times2} & \boldsymbol{0}_{3\times3} \end{bmatrix}, \quad \boldsymbol{R}_{2,ip} = 5 \times 10^{3}\boldsymbol{I}_{2\times2}$$

$$\boldsymbol{Q}_{2,op} = \begin{bmatrix} 2.4 \times 10^{-2} & 0 \\ 0 & 0 \end{bmatrix}, \quad \boldsymbol{R}_{2,op} = 5 \times 10^{2}$$

$$\boldsymbol{Q}_{3,ip} = \begin{bmatrix} 1.1 \times 10^{-2}\boldsymbol{I}_{2\times2} & \boldsymbol{0}_{2\times2} \\ \boldsymbol{0}_{2\times2} & \boldsymbol{0}_{2\times2} \end{bmatrix}, \quad \boldsymbol{R}_{3,ip} = 10^{2}\boldsymbol{I}_{2\times2}$$

$$\boldsymbol{Q}_{3,op} = \begin{bmatrix} 20 & 0 \\ 0 & 8 \end{bmatrix}, \quad \boldsymbol{R}_{3,op} = 10^{10}$$

Calibrated state feedback control law was no longer considered, since it was developed on equations that do not take in account mass variation. During these tests,

Table 6.3: Test 2, total control usage Δv in m/s.

Test case	Calib.State	SDRE Par.1	SDRE Par.2	SDRE Par.3
		$e = 0$		
$\delta e = 0.01$, $\delta i = 0.01$ rad	93	164	290	228
$\delta e = 0.1$, $\delta i = 0.1$ rad	939	1662	3216	2370
$\delta e = 0.2$, $\delta i = 0.2$ rad	1898	3405	7755	4962
$\delta\Omega = \delta\omega = 0.01$ rad	76	118	235	419
$\delta\Omega = \delta\omega = 0.1$ rad	763	1222	2429	4207
$\delta\Omega = \delta\omega = 0.2$ rad	1538	2550	5028	8350
		$e = 0.3$		
$\delta e = 0.01$, $\delta i = 0.01$ rad	113	155	279	263
$\delta e = 0.1$, $\delta i = 0.1$ rad	1130	1546	2912	2764
$\delta e = 0.2$, $\delta i = 0.2$ rad	2250	3838	6079	5890
$\delta\Omega = \delta\omega = 0.01$ rad	81	121	173	303
$\delta\Omega = \delta\omega = 0.1$ rad	812	1221	1761	2939
$\delta\Omega = \delta\omega = 0.2$ rad	1634	2486	3590	5656

Table 6.4: Test 2, total maneuver time in T.

Test case	Calib.State	SDRE Par.1	SDRE Par.2	SDRE Par.3
		$e = 0$		
$\delta e = 0.01$, $\delta i = 0.01$ rad	18.067	1.880	2.694	1.860
$\delta e = 0.1$, $\delta i = 0.1$ rad	23.447	2.294	3.452	2.305
$\delta e = 0.2$, $\delta i = 0.2$ rad	24.940	2.422	3.815	2.439
$\delta\Omega = \delta\omega = 0.01$ rad	18.209	1.836	2.388	1.981
$\delta\Omega = \delta\omega = 0.1$ rad	23.216	2.263	3.200	2.427
$\delta\Omega = \delta\omega = 0.2$ rad	24.715	2.417	3.434	2.562
		$e = 0.3$		
$\delta e = 0.01$, $\delta i = 0.01$ rad	17.257	1.633	1.604	1.447
$\delta e = 0.1$, $\delta i = 0.1$ rad	23.980	2.034	2.168	2.270
$\delta e = 0.2$, $\delta i = 0.2$ rad	26.150	2.127	2.264	2.273
$\delta\Omega = \delta\omega = 0.01$ rad	21.952	1.634	1.602	1.564
$\delta\Omega = \delta\omega = 0.1$ rad	28.808	2.015	1.952	2.273
$\delta\Omega = \delta\omega = 0.2$ rad	30.134	2.127	2.226	2.284

Table 6.5: Test 3, total control usage Δv difference in % with respect to Test 2 values.

Test case	SDRE Par.1	SDRE Par.2	SDRE Par.3
	$e = 0$		
$\delta e = 0.01$, $\delta i = 0.01$ rad	−8.16	−24.50	6.24
$\delta e = 0.1$, $\delta i = 0.1$ rad	−7.23	−28.58	6.71
$\delta e = 0.2$, $\delta i = 0.2$ rad	−5.30	−36.67	7.42
$\delta\Omega = \delta\omega = 0.01$ rad	−8.51	20.77	89.19
$\delta\Omega = \delta\omega = 0.1$ rad	−8.90	18.23	88.47
$\delta\Omega = \delta\omega = 0.2$ rad	−8.83	15.31	75.18
	$e = 0.3$		
$\delta e = 0.01$, $\delta i = 0.01$ rad	−7.69	14.71	23.74
$\delta e = 0.1$, $\delta i = 0.1$ rad	−6.25	21.22	24.51
$\delta e = 0.2$, $\delta i = 0.2$ rad	−0.56	31.26	25.75
$\delta\Omega = \delta\omega = 0.01$ rad	−4.17	29.95	81.24
$\delta\Omega = \delta\omega = 0.1$ rad	−4.35	30.52	86.67
$\delta\Omega = \delta\omega = 0.2$ rad	−4.39	30.55	91.38

only total control usage was considered and compared to the values reported in Table 6.3. The aim was to understand if the introduction of mass variation in the SDC parametrization improves the control performance. Table 6.5 shows simulations results. As can be seen, only the performance of the SDRE controller using parametrization 1 improved, whereas performance of the other controllers significantly got worse.

In Figures 6.1 and 6.2 the trajectories generated by all the controllers analysed are shown. Sinclair's control does not converge smoothly and the oscillation may be a problem in a real situation, since collision with other objects may occur. Figures 6.3 and 6.4 show the relative distance evolution during the maneuver. Again, calibrated state feedback control law oscillations are visible. Moreover, Sinclair's control shows initial overshoots sometimes excessively high, with values between 1000 and 2000 km.

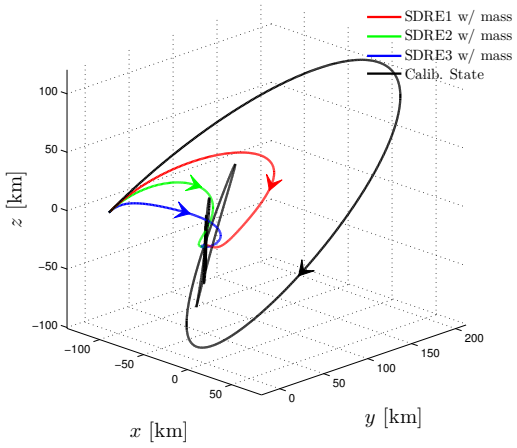

(a) $\delta e = 0.01$, $\delta i = 0.01\,\text{rad}$.

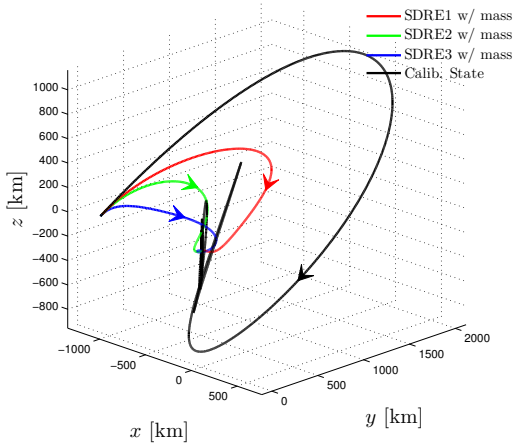

(b) $\delta e = 0.1$, $\delta i = 0.1\,\text{rad}$.

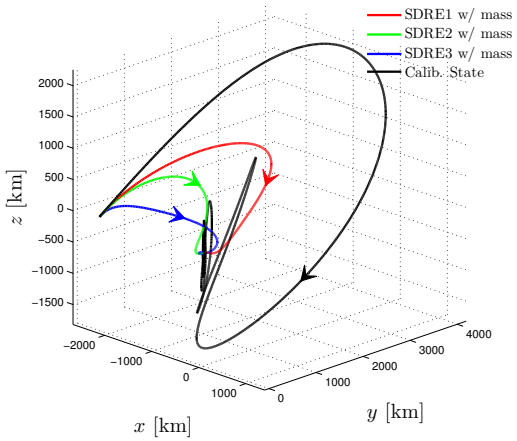

(c) $\delta e = 0.2$, $\delta i = 0.2\,\text{rad}$.

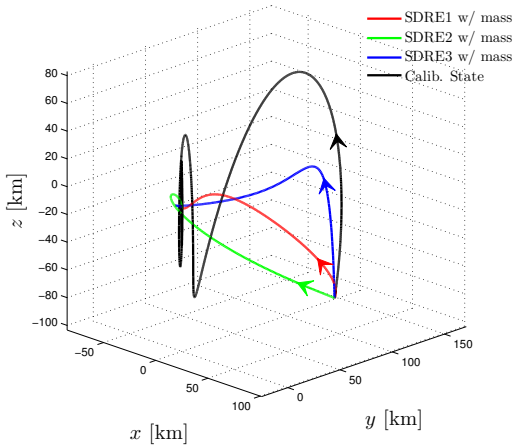

(d) $\delta\Omega = \delta\omega = 0.01\,\text{rad}$.

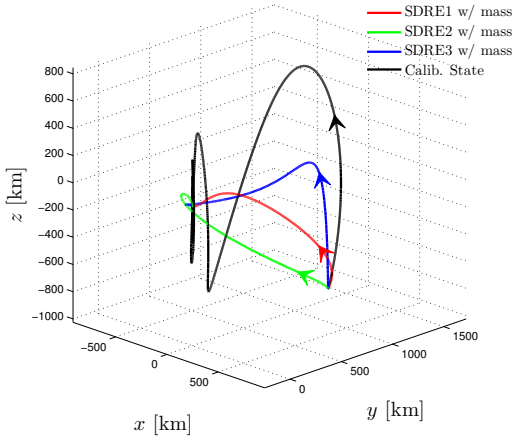

(e) $\delta\Omega = \delta\omega = 0.1\,\text{rad}$.

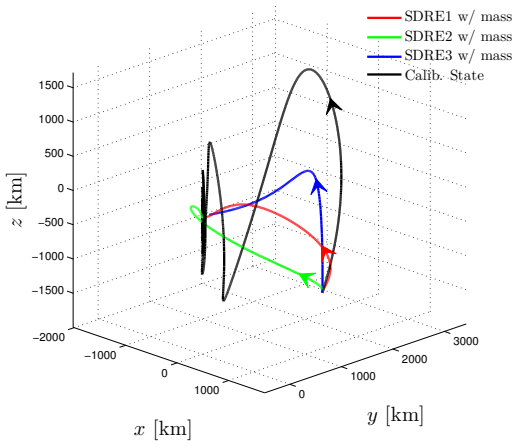

(f) $\delta\Omega = \delta\omega = 0.2\,\text{rad}$.

Figure 6.1: Trajectories for $e = 0$.

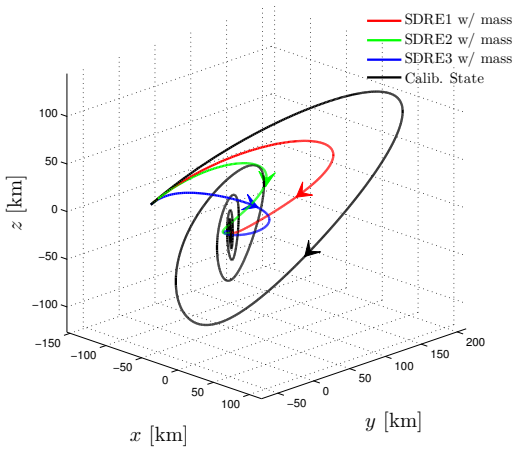

(a) $\delta e = 0.01$, $\delta i = 0.01$ rad.

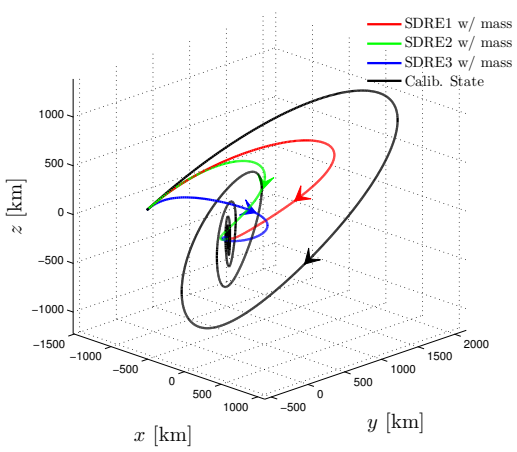

(b) $\delta e = 0.1$, $\delta i = 0.1$ rad.

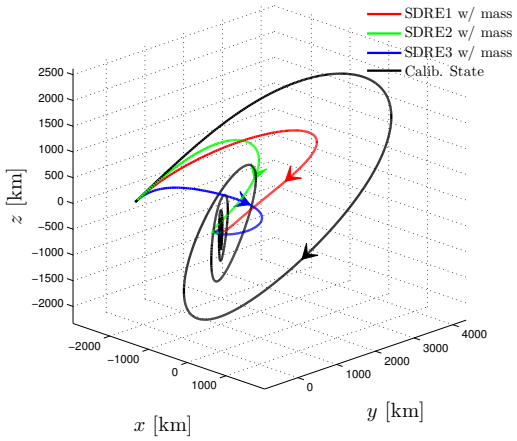

(c) $\delta e = 0.2$, $\delta i = 0.2$ rad.

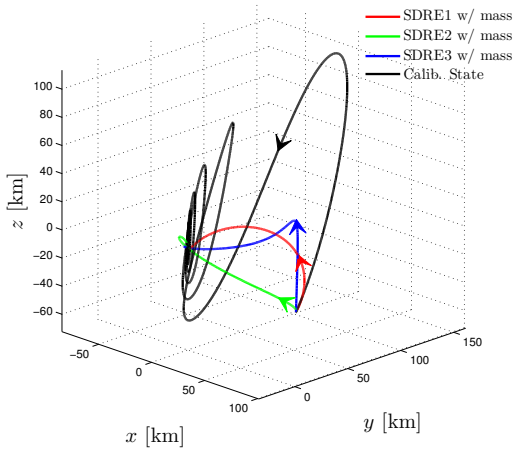

(d) $\delta\Omega = \delta\omega = 0.01$ rad.

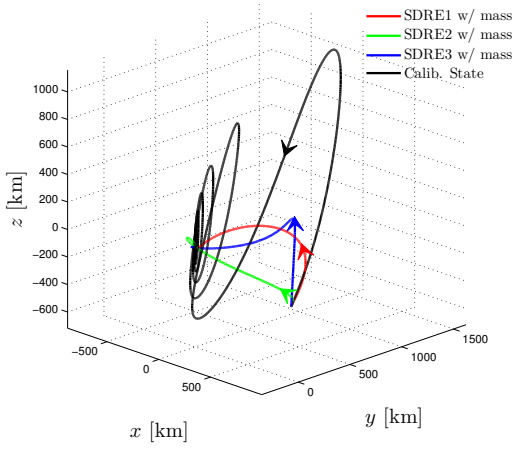

(e) $\delta\Omega = \delta\omega = 0.1$ rad.

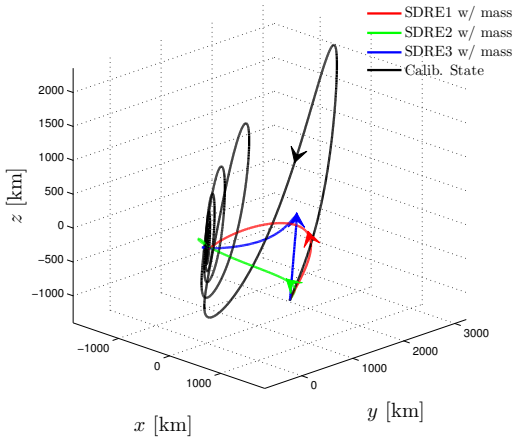

(f) $\delta\Omega = \delta\omega = 0.2$ rad.

Figure 6.2: Trajectories for $e = 0.3$.

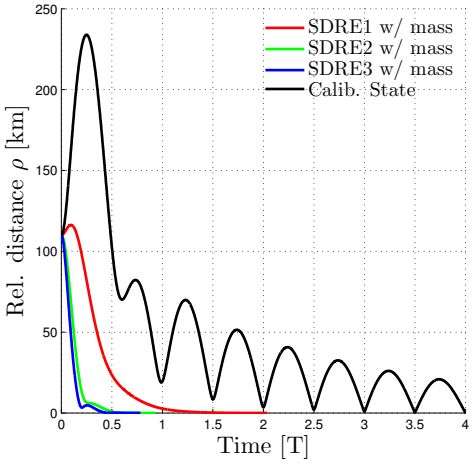

(a) $\delta e = 0.01$, $\delta i = 0.01\,\text{rad}$.

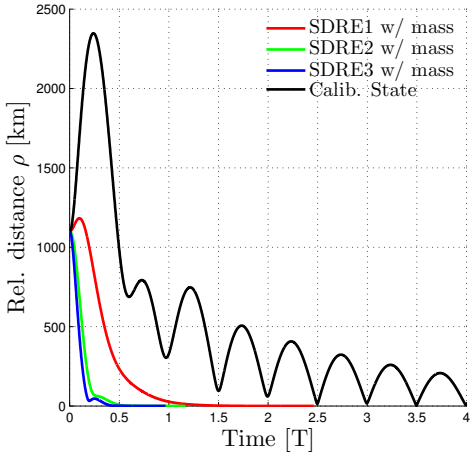

(b) $\delta e = 0.1$, $\delta i = 0.1\,\text{rad}$.

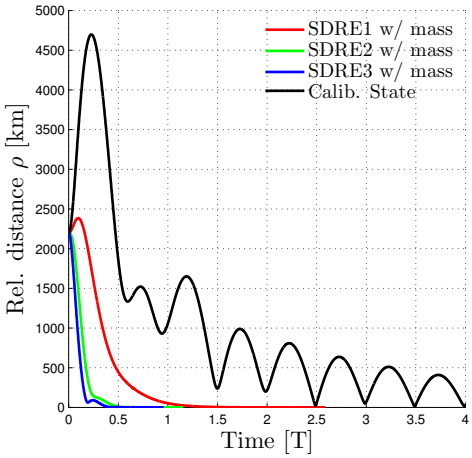

(c) $\delta e = 0.2$, $\delta i = 0.2\,\text{rad}$.

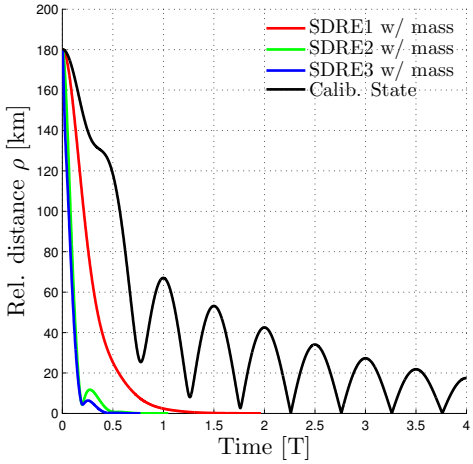

(d) $\delta\Omega = \delta\omega = 0.01\,\text{rad}$.

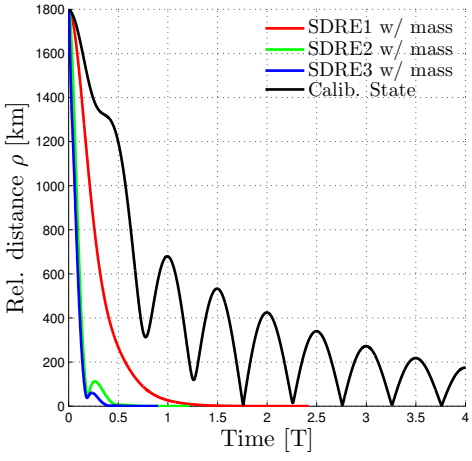

(e) $\delta\Omega = \delta\omega = 0.1\,\text{rad}$.

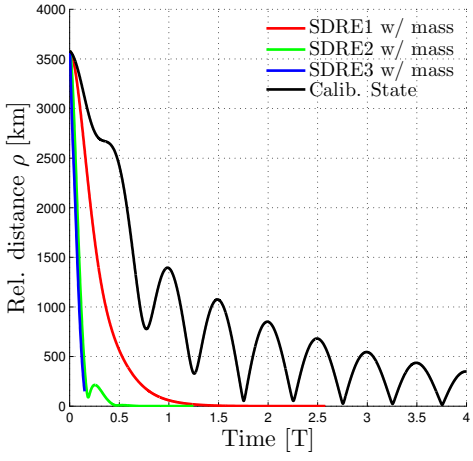

(f) $\delta\Omega = \delta\omega = 0.2\,\text{rad}$.

Figure 6.3: Relative distance over 4 orbit periods for $e = 0$.

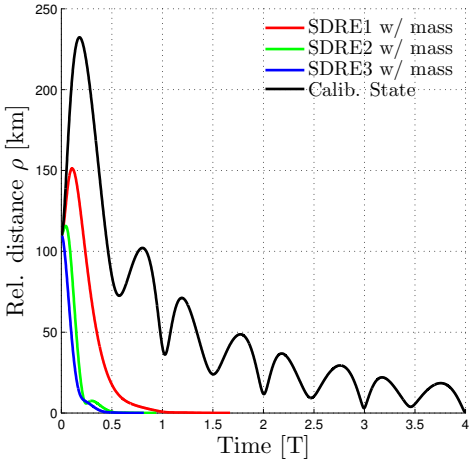

(a) $\delta e = 0.01$, $\delta i = 0.01\,\text{rad}$.

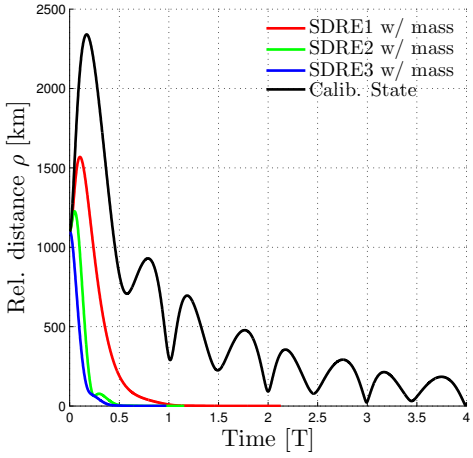

(b) $\delta e = 0.1$, $\delta i = 0.1\,\text{rad}$.

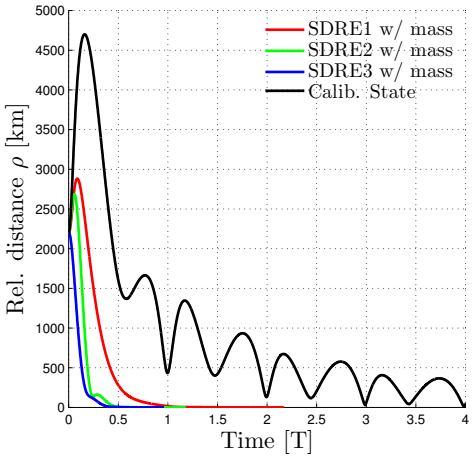

(c) $\delta e = 0.2$, $\delta i = 0.2\,\text{rad}$.

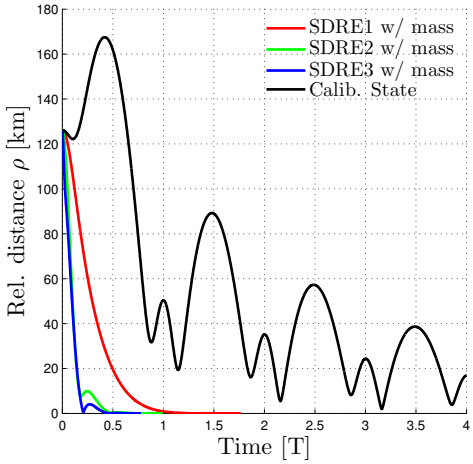

(d) $\delta\Omega = \delta\omega = 0.01\,\text{rad}$.

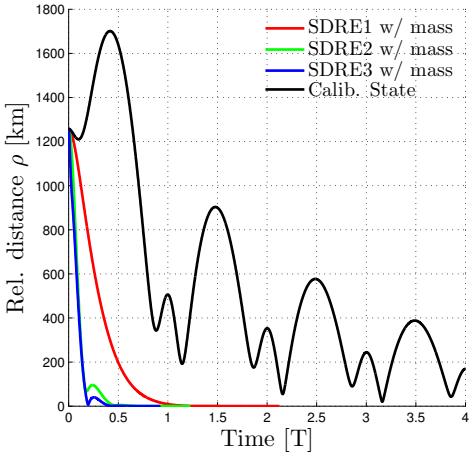

(e) $\delta\Omega = \delta\omega = 0.1\,\text{rad}$.

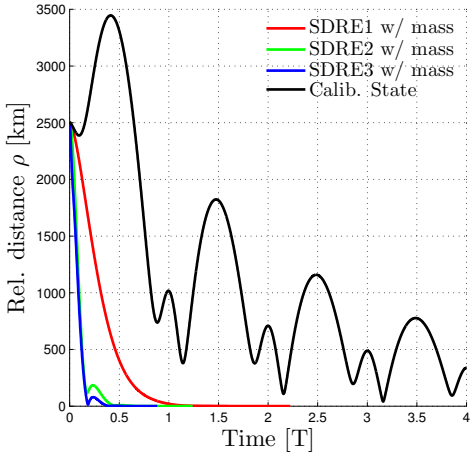

(f) $\delta\Omega = \delta\omega = 0.2\,\text{rad}$.

Figure 6.4: Relative distance over 4 orbit periods for $e = 0.3$.

Chapter 7

SDRE Control of Relative Perturbed Motion

In this section the SDRE control is applied to control the relative perturbed motion. Two different controllers were developed and compared: a nonlinear SDRE-$\mathcal{H}_\infty$ controller and a SDRE controller.

The nonlinear $\mathcal{H}_\infty$ controller was designed using the extended linearization technique presented in Section 5.2. In particular, an $\mathcal{H}_\infty$ controller is computed at each sampling time, using the SDC matrices result of the extended linearization process. A classical SDRE controller was also developed to draw a comparison.

Moreover, a SDRE controller based on LERM equations was designed in order to understand if perturbation modelling is really necessary. Atmospheric drag and J_2 perturbations acceleration are several orders lower than gravitational acceleration and the resulting differential perturbation tends to zero as the distance between deputy and chief decreases. Hence, LERM equations accuracy improves as the system goes to the origin.

In Section 7.1 the nonlinear $\mathcal{H}_\infty$ control based on extended linearization technique is presented. The SDRE-$\mathcal{H}_\infty$ controller for relative perturbed motion is then developed in Section 7.2, whereas in Section 7.3 the SDRE controllers based on nonlinear equations of relative perturbed motion and on LERM equations are de-

veloped. The controllers were tested on terminal rendezvous and formation control mission scenarios and the results are presented in Section 7.4.

7.1 Nonlinear $\mathcal{H}_\infty$ Control using Extended Linearization

The use of extend linearization for $\mathcal{H}_\infty$ nonlinear controller design was proposed by Cloutier et al. in [59, 76]. In literature very few application of this control technique can be found [77].

The idea behind this technique is the same that led to the introduction of the SDRE controllers: given an SDC parametrization of the system, comprehensive of a performance output function, at each sample time compute the linear $\mathcal{H}_\infty$ control law by resolution of its characteristic algebraic Riccati equations. The results is a state-dependent $\mathcal{H}_\infty$ controller that in the following will be referred to as *SDRE-$\mathcal{H}_\infty$ controller*.

Consider a general nonlinear system characterized by the following equations

$$\begin{aligned}\dot{\boldsymbol{x}} &= \boldsymbol{f}(\boldsymbol{x}) + \boldsymbol{B}_1(\boldsymbol{x})\boldsymbol{w} + \boldsymbol{B}_2(\boldsymbol{x})\boldsymbol{u}\\ \boldsymbol{z} &= \boldsymbol{c}_1(\boldsymbol{x}) + \boldsymbol{D}_{12}(\boldsymbol{x})\boldsymbol{u}\\ \boldsymbol{y} &= \boldsymbol{c}_2(\boldsymbol{x}) + \boldsymbol{D}_{21}(\boldsymbol{x})\boldsymbol{w}\end{aligned}$$

where $\boldsymbol{x} \in \mathbb{R}^n$, $\boldsymbol{u} \in \mathbb{R}^{m_2}$ and $\boldsymbol{w} \in \mathbb{R}^{m_1}$ are respectively the state, control and exogenous input (that may include tracking commands and/or disturbances) vectors, $\boldsymbol{y} \in \mathbb{R}^{m_3}$ is the system output and $\boldsymbol{z} \in \mathbb{R}^{m_4}$ is the performance output. Assume that

- $\boldsymbol{D}_{12}(\boldsymbol{x})$ and $\boldsymbol{D}_{21}(\boldsymbol{x})$ have full rank;
- $\boldsymbol{f}(\boldsymbol{0}) = \boldsymbol{c}_2(\boldsymbol{0}) = \boldsymbol{0}$;
- $\boldsymbol{B}_2(\boldsymbol{x}) \neq \boldsymbol{0}$ for all $\boldsymbol{x}$.

The aim of $\mathcal{H}_\infty$ control is to find a causal controller $\boldsymbol{K}$ that minimize the $\mathcal{H}_\infty$ norm of the closed loop system. The cost function J can be expressed in terms of $\mathcal{L}_2$ norm as

$$J(\boldsymbol{K}) = \max_{\boldsymbol{w}(t)\neq\boldsymbol{0}} \frac{||\boldsymbol{z}(t)||}{||\boldsymbol{w}(t)||} \tag{7.2}$$

The minimization of Equation (7.2) is not straightforward. Thus, it is usually considered the sub-optimal problem: given $\gamma_\infty \in \mathbb{R}$, $\gamma_\infty > 0$, find a causal controller $\boldsymbol{K}$ such that $J(\boldsymbol{K}) < \gamma_\infty$. If such a controller exists then the following inequality holds

$$\int_0^T ||\boldsymbol{z}(t)||^2 \,\mathrm{dt} \leq \gamma_\infty^2 \int_0^T ||\boldsymbol{w}(t)||^2 \,\mathrm{dt}$$

for all $T \geq 0$ and all $\boldsymbol{w}(t) \in \mathcal{L}_2$ $\forall t \in [0, T]$ and the exogenous signal $\boldsymbol{w}(t)$ will be locally attenuated by γ_∞. The $\mathcal{H}_\infty$ problem tends to the $\mathcal{H}_2$ control problem as $\gamma_\infty \to +\infty$.

An approximate solution for the stated problem can be obtained using the extended linearization technique. Assume that exists an SDC parametrization of Equations (7.1),

$$\begin{aligned}
\dot{\boldsymbol{x}} &= \boldsymbol{A}(\boldsymbol{x})\boldsymbol{x} + \boldsymbol{B}_1(\boldsymbol{x})\boldsymbol{w} + \boldsymbol{B}_2(\boldsymbol{x})\boldsymbol{u} \\
\boldsymbol{z} &= \boldsymbol{C}_1(\boldsymbol{x})\boldsymbol{x} + \boldsymbol{D}_{12}(\boldsymbol{x})\boldsymbol{u} \\
\boldsymbol{y} &= \boldsymbol{C}_2(\boldsymbol{x})\boldsymbol{x} + \boldsymbol{D}_{21}(\boldsymbol{x})\boldsymbol{w}
\end{aligned} \tag{7.3a}$$

such that the pairs $\{\boldsymbol{A}(\boldsymbol{x}), \boldsymbol{B}_1(\boldsymbol{x})\}$, $\{\boldsymbol{A}(\boldsymbol{x}), \boldsymbol{B}_2(\boldsymbol{x})\}$, $\{\boldsymbol{C}_1(\boldsymbol{x}), \boldsymbol{A}(\boldsymbol{x})\}$, $\{\boldsymbol{C}_2(\boldsymbol{x}), \boldsymbol{A}(\boldsymbol{x})\}$ are respectively stabilizable and detectable in the region of interest Ω.

If γ_∞ is sufficiently large, then the positive-semidefinite solutions $\boldsymbol{P}(\hat{\boldsymbol{x}})$ and $\boldsymbol{Q}(\hat{\boldsymbol{x}})$ of the Riccati equations, which are given below in terms of state-dependent Hamiltonian matrices (state-dependence is omitted for simplicity), will exist and they are such that the maximum eigenvalue of $\boldsymbol{P}(\hat{\boldsymbol{x}})\boldsymbol{Q}(\hat{\boldsymbol{x}})$ is lower than γ_∞^2.

$$\begin{bmatrix} \boldsymbol{A} - \boldsymbol{B}_2\boldsymbol{R}_u^{-1}\boldsymbol{D}_{12}^T\boldsymbol{C}_1 & \gamma_\infty^{-2}\boldsymbol{B}_1\boldsymbol{B}_1^T - \boldsymbol{B}_2\boldsymbol{R}_u^{-1}\boldsymbol{B}_2^T \\ -\hat{\boldsymbol{C}}_1^T\hat{\boldsymbol{C}}_1 & -\left(\boldsymbol{A} - \boldsymbol{B}_2\boldsymbol{R}_u^{-1}\boldsymbol{D}_{12}^T\boldsymbol{C}_1\right)^T \end{bmatrix} \quad \rightarrow \quad \boldsymbol{P}(\hat{\boldsymbol{x}})$$

$$\begin{bmatrix} \left(\boldsymbol{A} - \boldsymbol{B}_1\boldsymbol{D}_{21}^T\boldsymbol{R}_w^{-1}\boldsymbol{C}_2\right)^T & \gamma_\infty^{-2}\boldsymbol{C}_1^T\boldsymbol{C}_1 - \boldsymbol{C}_2^T\boldsymbol{R}_w^{-1}\boldsymbol{C}_2 \\ -\hat{\boldsymbol{B}}_1\hat{\boldsymbol{B}}_1^T & -\left(\boldsymbol{A} - \boldsymbol{B}_1\boldsymbol{D}_{21}^T\boldsymbol{R}_w^{-1}\boldsymbol{C}_2\right) \end{bmatrix} \quad \rightarrow \quad \boldsymbol{Q}(\hat{\boldsymbol{x}})$$

The matrices $\hat{\boldsymbol{B}}_1$, $\hat{\boldsymbol{C}}_1$, $\boldsymbol{R}_u$ and $\boldsymbol{R}_w$ are defined as follows,

- $\hat{\boldsymbol{B}}_1 \triangleq \boldsymbol{B}_1\left(\boldsymbol{I} - \boldsymbol{D}_{21}^T\boldsymbol{R}_w^{-1}\boldsymbol{D}_{21}\right)$;
- $\hat{\boldsymbol{C}}_1 \triangleq \left(\boldsymbol{I} - \boldsymbol{D}_{12}\boldsymbol{R}_u^-1\boldsymbol{D}_{12}^T\right)\boldsymbol{C}_1$;
- $\boldsymbol{R}_u \triangleq \boldsymbol{D}_{12}^T\boldsymbol{D}_{12}$;
- $\boldsymbol{R}_w \triangleq \boldsymbol{D}_{21}\boldsymbol{D}_{21}^T$;

The SDRE-$\mathcal{H}_\infty$ nonlinear controller is then characterized by the following set of equations, that describes the observer and the state-feedback control law,

$$\dot{\hat{\boldsymbol{x}}} = \boldsymbol{A}_o(\hat{\boldsymbol{x}})\hat{\boldsymbol{x}} + \boldsymbol{B}_o(\hat{\boldsymbol{x}})\boldsymbol{y} \tag{7.4a}$$

$$\boldsymbol{u} = \boldsymbol{F}(\hat{\boldsymbol{x}})\hat{\boldsymbol{x}} \tag{7.4b}$$

where the following state-dependent matrices were introduced,

- $\boldsymbol{L} \triangleq -\left(\boldsymbol{Q}\boldsymbol{C}_2^T + \boldsymbol{B}_1\boldsymbol{D}_{21}^T\right)\boldsymbol{R}_w^{-1}$;
- $\boldsymbol{Z} \triangleq \left(\boldsymbol{I} - \gamma_\infty^{-2}\boldsymbol{Q}\boldsymbol{P}\right)^{-1}$;
- $\boldsymbol{F} \triangleq -\boldsymbol{R}_u^{-1}\left(\boldsymbol{B}_2^T\boldsymbol{P} + \boldsymbol{D}_{12}^T\boldsymbol{C}_1\right)$;
- $\boldsymbol{A}_o \triangleq \boldsymbol{A} + \boldsymbol{B}_2\boldsymbol{F} + \gamma_\infty^{-2}\boldsymbol{B}_1\boldsymbol{B}_1^T\boldsymbol{P} + \boldsymbol{Z}\boldsymbol{L}\left(\boldsymbol{C}_2 + \gamma_\infty^{-2}\boldsymbol{D}_{21}\boldsymbol{B}_1^T\boldsymbol{P}\right)$;
- $\boldsymbol{B}_o \triangleq -\boldsymbol{Z}\boldsymbol{L}$.

If the state is known, then Equations (7.3a) disappears, as well as the observer, Equation (7.4a), and the SDRE-$\mathcal{H}_\infty$ controller is given by Equation (7.4b), with the state estimation $\hat{\boldsymbol{x}}$ substituted with the real state $\boldsymbol{x}$.

7.2 SDRE-$\mathcal{H}_\infty$ Control of Relative Perturbed Motion

The relative perturbed motion can be written in a form that considers the differential perturbation acceleration as an external disturbance. In particular, a new set of SDC matrices can be introduced, $\boldsymbol{A}(\boldsymbol{x})$, $\boldsymbol{B}_1(\boldsymbol{x})$ and $\boldsymbol{B}_2$, such that the system dynamic can be written as

$$\dot{\boldsymbol{x}} = \boldsymbol{A}(\boldsymbol{x}) + \boldsymbol{B}_1(\boldsymbol{x}) + \boldsymbol{B}_2\boldsymbol{u}$$

Using Equation (6.2) to rewrite the bias term $\mu\left(\frac{1}{r^2} - \frac{r}{r_d^3}\right)$ as a linear function of the state (Section 6.1.3), the SDC matrices have the following expressions.

$$\boldsymbol{A}(\boldsymbol{x}) = \begin{bmatrix} 0 & 0 & 0 & 1 & 0 & 0 \\ 0 & 0 & 0 & 0 & 1 & 0 \\ 0 & 0 & 0 & 0 & 0 & 1 \\ \omega_z^2 - \frac{\mu}{r_d^3} + \gamma\,(2r + x) & \dot{\omega}_z + \gamma y & \gamma z - \omega_x\omega_z & 0 & 2\omega_z & 0 \\ -\dot{\omega}_z & \omega_x^2 + \omega_z^2 - \frac{\mu}{r_d^3} & \dot{\omega}_x & -2\omega_z & 0 & 2\omega_x \\ -\omega_x\omega_z & -\dot{\omega}_x & \omega_x^2 - \frac{\mu}{r_d^3} & 0 & -2\omega_x & 0 \end{bmatrix}$$

$$\boldsymbol{B}_1(\boldsymbol{x}) = \begin{bmatrix} \boldsymbol{0}_{3\times3} \\ \boldsymbol{I}_{3\times3}\Delta\boldsymbol{a}_p \end{bmatrix}, \qquad \boldsymbol{B}_2 = \begin{bmatrix} \boldsymbol{0}_{3\times3} \\ \frac{1}{m}\boldsymbol{I}_{3\times3} \end{bmatrix}$$

In order to design an SDRE-$\mathcal{H}_\infty$ controller, a performance output function must be introduced,

$$\boldsymbol{z} = \boldsymbol{C}_1\boldsymbol{x} + \boldsymbol{D}_{12}\boldsymbol{u}$$

where

$$\boldsymbol{C}_1 = \begin{bmatrix} \alpha_1\boldsymbol{I}_{3\times3} & \boldsymbol{0}_{3\times3} \\ \boldsymbol{0}_{3\times3} & \alpha_2\boldsymbol{I}_{3\times3} \\ \boldsymbol{0}_{3\times3} & \boldsymbol{0}_{3\times3} \end{bmatrix}, \qquad \boldsymbol{D}_{12} = \begin{bmatrix} \boldsymbol{0}_{6\times3} \\ \alpha_3\boldsymbol{I}_{3\times3} \end{bmatrix}$$

and $\alpha_1, \alpha_2, \alpha_3 \in \mathbb{R}$ are such that $\alpha_1, \alpha_2, \alpha_3 > 0$. With this choice of matrices the performance output norm is

$$||\boldsymbol{z}||^2 = \alpha_1^2 \rho + \alpha_2^2 \dot{\rho} + \alpha_3^2 u$$

and when $\gamma_\infty \to +\infty$ the controller is equivalent to the SDRE controller developed for parametrization 1 in Section 6.1.2 (the differential perturbation acceleration is no longer considered).

7.3 SDRE Control of Relative Perturbed Motion

A possible SDRE controller can be designed considering the differential perturbation acceleration $\Delta \boldsymbol{a}_p$ in Equation (2.34) as a bias term. Actually, the term is state-dependent, but its reformulation as a linear function of $\boldsymbol{x}$ is not straightforward and may increase controller complexity, affecting the overall performance.

The differential perturbation acceleration can be introduced in the SDC matrix $\boldsymbol{A}(\boldsymbol{x})$ defining a new fictitious stable state ξ, with dynamic $\dot{\xi} = -\lambda\xi$ ($\lambda > 0$), similar to parametrization 2 presented in Section 6.1.3. Introducing the new state vector,

$$\tilde{\boldsymbol{x}} = [\ x \quad y \quad z \quad \dot{x} \quad \dot{y} \quad \dot{z} \quad \xi\ ]^T$$

and ξ in Equations (2.34) (comprehensive of fuel comsumption and consequent deputy's mass variation),

$$\begin{aligned}
\ddot{x} &= \left(\omega_z^2 - \frac{\mu}{r_d^3}\right) x + \dot{\omega}_z y - \omega_x \omega_z z + 2\omega_z \dot{y} + \mu \left(\frac{1}{r^2} - \frac{r}{r_d^3}\right) + \frac{\Delta a_{p_x}}{\xi}\xi + \frac{u_x}{m} \\
\ddot{y} &= -\dot{\omega}_z x + \left(\omega_x^2 + \omega_z^2 - \frac{\mu}{r_d^3}\right) y + \dot{\omega}_x z - 2\omega_z \dot{x} + 2\omega_x \dot{z} + \frac{\Delta a_{p_y}}{\xi}\xi + \frac{u_y}{m} \\
\ddot{z} &= -\omega_x \omega_z x - \dot{\omega}_x y + \left(\omega_x^2 - \frac{\mu}{r_d^3}\right) z - 2\omega_x \dot{y} + \frac{\Delta a_{p_z}}{\xi}\xi + \frac{u_z}{m}
\end{aligned}$$

using again Equation (6.2) the SDC matrices $\boldsymbol{A}(\tilde{\boldsymbol{x}})$ and $\boldsymbol{B}$ can be written as follows.

$$\boldsymbol{A}(\tilde{\boldsymbol{x}}) = \begin{bmatrix} 0 & 0 & 0 & 1 & 0 & 0 & 0 \\ 0 & 0 & 0 & 0 & 1 & 0 & 0 \\ 0 & 0 & 0 & 0 & 0 & 1 & 0 \\ \omega_z^2 - \frac{\mu}{r_d^3} + \gamma\,(2r + x) & \dot{\omega}_z + \gamma y & \gamma z - \omega_x \omega_z & 0 & 2\omega_z & 0 & \frac{\Delta a_{p_x}}{\xi} \\ -\dot{\omega}_z & \omega_x^2 + \omega_z^2 - \frac{\mu}{r_d^3} & \dot{\omega}_x & -2\omega_z & 0 & 2\omega_x & \frac{\Delta a_{p_y}}{\xi} \\ -\omega_x \omega_z & -\dot{\omega}_x & \omega_x^2 - \frac{\mu}{r_d^3} & 0 & -2\omega_x & 0 & \frac{\Delta a_{p_z}}{\xi} \\ 0 & 0 & 0 & 0 & 0 & 0 & -\lambda \end{bmatrix}$$

$$\boldsymbol{B}(t) = \begin{bmatrix} \boldsymbol{0}_{3\times 3} \\ \frac{1}{m}\boldsymbol{I}_{3\times 3} \\ \boldsymbol{0}_{1\times 3} \end{bmatrix}$$

Atmospheric drag and J_2 perturbations acceleration are several order smaller than gravitational acceleration. Moreover, as the distance between the satellite decreases, i.e. the state goes to the origin, $\Delta \boldsymbol{a}_p$ goes to zero. Therefore, LERM equation may be taken in account for designing a SDRE controller, since represent a good approximation of the motion and demand less computational resources. As a matter of fact perturbations no longer need to be computed and at each sample time LERM parameters that depend on chief's orbit are updated.

Extended linearization of Equations (2.27) is straightforward,

$$\boldsymbol{A}(\boldsymbol{x}) = \begin{bmatrix} 0 & 0 & 0 & 1 & 0 & 0 \\ 0 & 0 & 0 & 0 & 1 & 0 \\ 0 & 0 & 0 & 0 & 0 & 1 \\ \dot{f}^2\left(1 + 2\frac{r}{p}\right) & -2\dot{f}\frac{\dot{r}}{r} & 0 & 0 & 2\dot{f} & 0 \\ 2\dot{f}\frac{\dot{r}}{r} & \dot{f}^2\left(1 - \frac{r}{p}\right) & 0 & -2\dot{f} & 0 & 0 \\ 0 & 0 & -\dot{f}^2\frac{r}{p} & 0 & 0 & 0 \end{bmatrix}, \quad \boldsymbol{B} = \begin{bmatrix} \boldsymbol{0}_{3\times 3} \\ \frac{1}{m}\boldsymbol{I}_{3\times 3} \end{bmatrix}$$

Table 7.1: TerraSAR-X and TanDEM-X characteristics.

	TerraSAR-X	TanDEM-X
Ballistic Coef.	2.3	2.5393
Transversal Area [m^2]	3.2	3.2
Total Mass [kg]	1238	1340
Fuel [kg]	-	120
Thruster I_{sp}	-	220

7.4 Simulations Results

The controllers developed in the previous sections were tested on formation control and terminal rendezvous operations. Data of TerraSAR-X and TanDEM-X missions was used to set up a realistic simulations with Simulink. Sample time was set to $T/1000$ and 4^{th} order Runge - Kutta integration algorithm was selected.

TerraSAR-X and TanDEM-X missions were developed by DLR and Astrium and their primary objective is the generation of an Earth's digital elevation model with an unprecedented accuracy. The satellites fly in a closely controlled formation with typical distances between 250 and 500 metres since 2010. More information can be found in [78, 79]. Satellites' characteristics for relative perturbed motion simulation were taken from [80, 81]. TerraSAR-X is the formation leader and its orbit is

$$a = 6886.310\,\text{km}, \quad e = 0.0001584, \quad i = 97.44^\circ, \quad \Omega = 0, \quad \omega = 0$$

The satellites began its operations in 2007 and was followed by TanDEM-X, launched in 2010. TanDEM-X was designed to be almost identical to TerraSAR-X, in order to eliminate as much as possible differential perturbations influence. The aim of TanDEM-X mission is not only the development of a digital elevation model, but also the test of new formation control algorithms, collecting data for future mission development. The satellite has different set of thrusters for altitude, position correction and fine-tuning of relative position. In this simulations only position correction thrusters were considered. Satellites' characteristics are listed in Table 7.1.

Table 7.2: Terminal rendezvous tests results, control usage Δv in m/s.

Test case	SDRE-$\mathcal{H}_\infty$	SDRE	SDRE w/ LERM
$\delta e = 0.01$, $\delta i = 0.01\,\text{rad}$	149.532	148.677	164.107
$\delta\Omega = \delta\omega = 0.01\,\text{rad}$	112.231	111.319	111.399
$\delta e = 0.01$, $\delta i = \delta\Omega = 0.01\,\text{rad}$	176.938	177.364	189.581

Three different terminal rendezvous tests were performed with different initial separations. Terminal rendezvous conditions were the same of tests in Section 6.2. For these tests, total control usage, Equation (4.3), and total maneuver duration time were considered as performance indexes. Weighting and output performance matrices were tuned using the same automatic procedure of Section 6.2. For terminal rendezvous simulations the following matrices were found,

$$\boldsymbol{C}_1 = \begin{bmatrix} \boldsymbol{I}_{3\times3} & \boldsymbol{0}_{3\times3} \\ \boldsymbol{0}_{3\times3} & 10^2\boldsymbol{I}_{3\times3} \end{bmatrix}, \quad \boldsymbol{D}_{12} = \begin{bmatrix} \boldsymbol{0}_{6\times3} \\ 10^3\boldsymbol{I}_{3\times3} \end{bmatrix}, \quad \gamma_\infty = 1$$

$$\boldsymbol{Q}_\text{S} = \begin{bmatrix} 10^{-1}\boldsymbol{I}_{3\times3} & \boldsymbol{0}_{3\times3} \\ \boldsymbol{0}_{3\times3} & 10^4\boldsymbol{I}_{3\times3} \end{bmatrix}, \quad \boldsymbol{R}_\text{S} = 10^5\boldsymbol{I}_{3\times3}, \quad \lambda = 10^{-3}$$

$$\boldsymbol{Q}_\text{L} = \begin{bmatrix} 10^{-1}\boldsymbol{I}_{3\times3} & \boldsymbol{0}_{3\times3} \\ \boldsymbol{0}_{3\times3} & 10^{-5}\boldsymbol{I}_{3\times3} \end{bmatrix}, \quad \boldsymbol{R}_\text{L} = 10^5\boldsymbol{I}_{3\times3}$$

$\boldsymbol{Q}_\text{S}$ and $\boldsymbol{R}_\text{S}$ are the weighting matrices of the SDRE controller, whereas $\boldsymbol{Q}_\text{L}$ and $\boldsymbol{R}_\text{L}$ belongs to the SDRE controller developed using LERM equations.

As can be seen in Tables 7.2 and 7.3 controllers performances are almost the same. SDRE controller designed using LERM equations showed a slightly greater control usage. Also the generated trajectories, shown in Figure 7.1, are very close and almost identical.

Two different operations were considered for formation control tests: formation keeping and formation maneuver. During formation keeping the deputy was

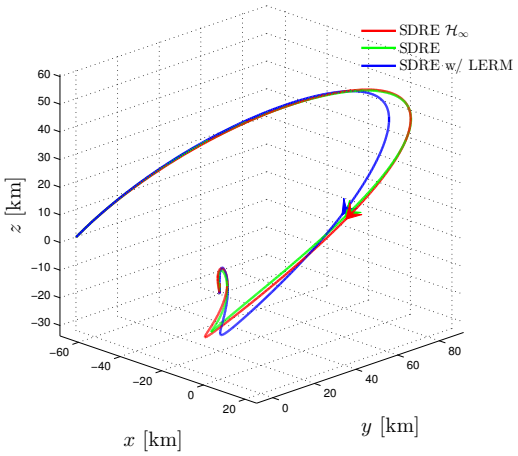

(a) Trajectory, $\delta e = 0.01$, $\delta i = 0.01$ rad.

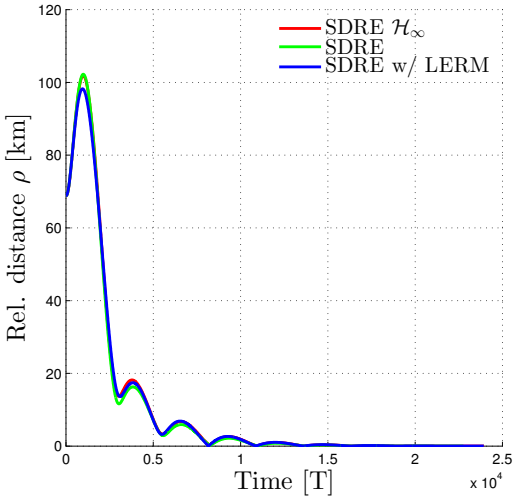

(b) Relative distance, $\delta e = 0.01$, $\delta i = 0.01$ rad.

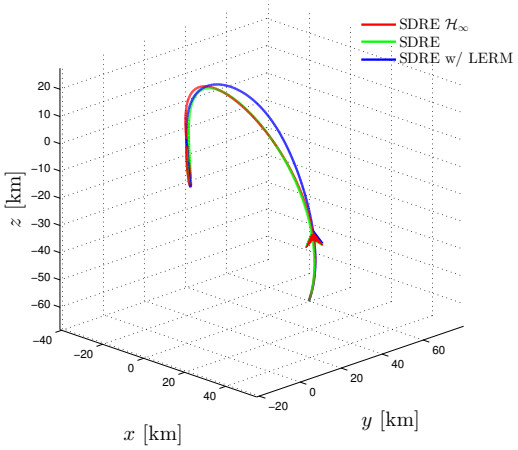

(c) Trajectory, $\delta\Omega = \delta\omega = 0.01$ rad.

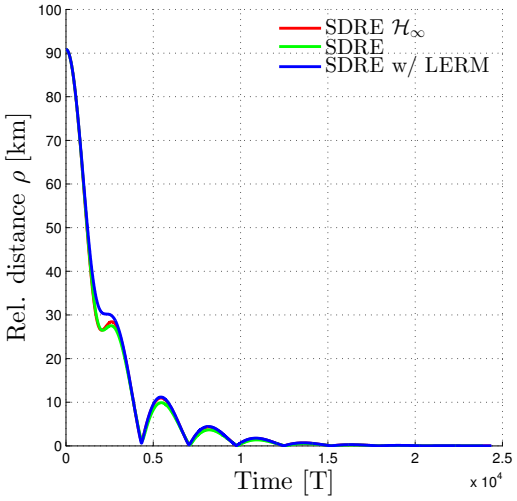

(d) Relative distance, $\delta\Omega = \delta\omega = 0.01$ rad.

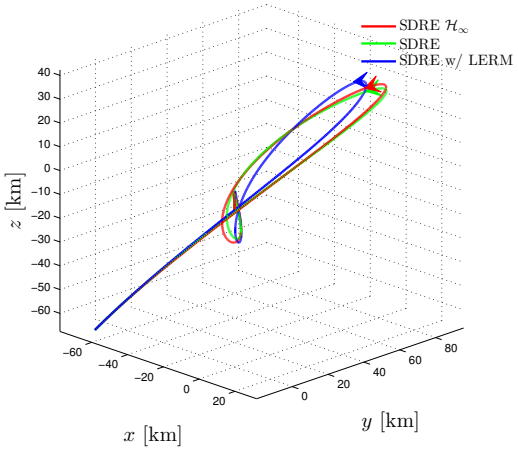

(e) Trajectory, $\delta e = 0.01$, $\delta i = \delta\Omega = 0.01$ rad.

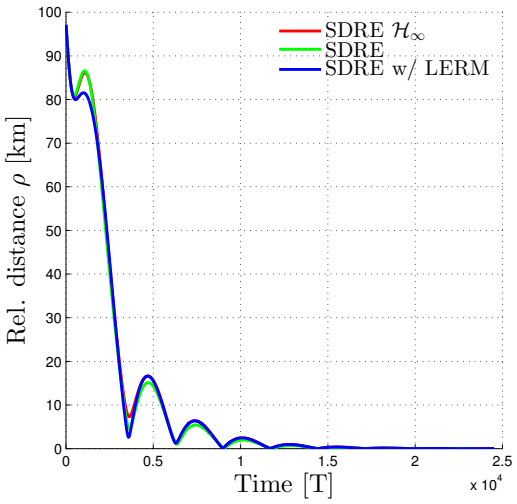

(f) Relative distance, $\delta e = 0.01$, $\delta i = \delta\Omega = 0.01$ rad.

Figure 7.1: Terminal rendezvous simulations.

Table 7.3: Terminal rendezvous tests results, maneuver duration in T.

Test case	SDRE-$\mathcal{H}_\infty$	SDRE	SDRE w/ LERM
$\delta e = 0.01$, $\delta i = 0.01\,\text{rad}$	4.210	4.002	4.207
$\delta\Omega = \delta\omega = 0.01\,\text{rad}$	4.279	4.198	4.285
$\delta e = 0.01$, $\delta i = \delta\Omega = 0.01\,\text{rad}$	4.311	4.121	4.312

demanded to keep a fixed relative position and velocity with respect to the chief,

$$\boldsymbol{\rho}_{\text{k}}^{L} = \begin{bmatrix} -350 \\ -200 \\ 0 \end{bmatrix} \text{ m}, \qquad \dot{\boldsymbol{\rho}}_{\text{k}}^{L} = \mathbf{0}_{3\times 1}$$

Formation maneuver instead consisted in following a time varying trajectory described by the following relative position and velocity vectors.

$$\boldsymbol{\rho}_{\text{m}}^{L} = 0.1 \begin{bmatrix} \cos\left(\frac{2\pi t}{T}\right) \\ \sin\left(\frac{2\pi t}{T}\right) \\ 0 \end{bmatrix} \text{ m}, \qquad \dot{\boldsymbol{\rho}}_{\text{m}}^{L} = 0.2\frac{\pi}{T} \begin{bmatrix} -\sin\left(\frac{2\pi t}{T}\right) \\ \cos\left(\frac{2\pi t}{T}\right) \\ 0 \end{bmatrix} \text{ m/s}$$

For these tests mean distance error $\overline{e}_\rho$ and mean speed error $\overline{e}_{\dot{\rho}}$ were considered, as well as total control usage. The automatic tuning procedure found the following weighting matrices for formation control,

$$\boldsymbol{C}_1 = \begin{bmatrix} 10^5\boldsymbol{I}_{3\times 3} & \mathbf{0}_{3\times 3} \\ \mathbf{0}_{3\times 3} & 10^{-4}\boldsymbol{I}_{3\times 3} \end{bmatrix}, \quad \boldsymbol{D}_{12} = \begin{bmatrix} \mathbf{0}_{6\times 3} \\ 10^5\boldsymbol{I}_{3\times 3} \end{bmatrix}, \quad \gamma_\infty = 1$$

$$\boldsymbol{Q}_{\text{S}} = \begin{bmatrix} 10^4\boldsymbol{I}_{3\times 3} & \mathbf{0}_{3\times 3} \\ \mathbf{0}_{3\times 3} & 10^5\boldsymbol{I}_{3\times 3} \end{bmatrix}, \quad \boldsymbol{R}_{\text{S}} = 10^4\boldsymbol{I}_{3\times 3}, \quad \lambda = 10^{-3}$$

$$\boldsymbol{Q}_{\text{L}} = \begin{bmatrix} 10^5\boldsymbol{I}_{3\times 3} & \mathbf{0}_{3\times 3} \\ \mathbf{0}_{3\times 3} & 10^{-2}\boldsymbol{I}_{3\times 3} \end{bmatrix}, \quad \boldsymbol{R}_{\text{L}} = 10^5\boldsymbol{I}_{3\times 3}$$

Test results are shown in Table 7.4. Controllers performances were tested over two orbital periods. Again, results are almost identical. There is not a significant

Table 7.4: Formation control, tests results.

Index	Formation keeping			Formation maneuver		
	SDRE-$\mathcal{H}_\infty$	SDRE	SDRE w/ LERM	SDRE-$\mathcal{H}_\infty$	SDRE	SDRE w/ LERM
$\overline{e}_\rho$ [m]	1.563	1.703	1.705	0.759	0.761	0.762
$\overline{e}_{\dot{\rho}}$ [10^{-4} m/s]	5.703	2.982	2.954	12.259	12.283	12.292
Δv [m/s]	14.658	14.664	14.664	6.596	6.596	6.596

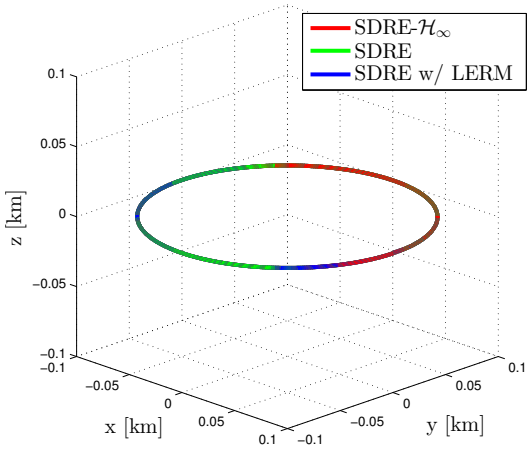

Figure 7.2: Formation maneuver, trajectories.

difference between indexes final values. In Figure 7.2 formation maneuver trajectory is showed. The three SDRE controllers followed almost the same trajectory during all the simulation.

Control loop execution time was also analysed. Using Simulink performance profiler the following values were found

- SDRE-$\mathcal{H}_\infty$: 2.701 ms;
- SDRE: 3.025 ms;
- SDRE w/ LERM: 2.018 ms.

SDRE designed using LERM equations resulted the quickest as expected, since perturbations accelerations do not need to be computed. SDRE-$\mathcal{H}_\infty$ controller execute its control loop in less time than the SDRE controller. Also this result was expected. The SDRE controller was developed upon a system of order 7, whereas the SDRE-$\mathcal{H}_\infty$ controller upon a system of order 6. ARE resolution demands more

time for the SDRE controller, since the greater order of the Hamiltonian matrix.

Chapter 8

Conclusions

The SDRE control method was applied to the control of relative motion in space. First, the unperturbed case was considered and three different parametrization of nonlinear equations of relative motion were proposed. The developed SDRE controllers were tested setting up a terminal rendezvous mission scenario and their performance were compared to a novel near-optimal control law. The SDRE controllers were the quickest to converge to the considered docking condition. However, propellant consumption was higher compared to calibrated state feedback law consumption.

Then, atmospheric drag and J_2 perturbations were considered and introduced in the equations of relative motion. The resulting equations set was used to develop a nonlinear $\mathcal{H}_\infty$ controller. In particular, using the extended linearization technique, an SDC parametrization of nonlinear equations of relative perturbed motion was obtained, considering differential perturbation acceleration term as an external disturbance. Then, an SDRE-$\mathcal{H}_\infty$ controller was developed, that, at each sampling time, compute an $\mathcal{H}_\infty$ controller, rather than a linear quadratic regulator. The SDRE-$\mathcal{H}_\infty$ controller was tested and compared to two classical SDRE controller, one based on nonlinear equation of relative perturbed motion, the other one developed using linear equations of relative motion. The aim was to understand if perturbations need to be taken in account by the SDRE control law. As a matter of

fact, the technique update the SDC matrices at each sampling time and as the system converges to the origin the differential perturbation term goes to zero. Thus, perturbation influence decrease as the manuever goes on and the correspondent accelerations computation may be avoided, decreasing control computational cost. The controllers were tested on terminal rendezvous and formation control mission scenarios. Simulation results showed that all the controllers are characterized by similar performance. However, the computational cost of SDRE controller based on linear equations of relative motion was significantly lower. This suggests a possible use of simpler relative motion models for SDRE controllers development.

Bibliography

[1] G. Mengali and A. A. Quarta, "Fondamenti di Meccanica del Volo Spaziale, Nuova Edizione", Italian. Pisa University Press, 2013.

[2] H. Schaub and J. L. Junkins, "Analytical Mechanics of Space Systems". AIAA Education Series, Oct. 2003.

[3] H. D. Curtis, "Orbital Mechanics for Engineering Students", Third Edition. Elsevier, 2014.

[4] K. Alfriend, S. Vadali, P. Gurfil, J. How, and L. Breger, "Spacecraft Formation Flying: Dynamics, Control and Navigation". Elsevier Astrodynamics Series, 2009.

[5] G. P. Sutton and O. Biblarz, "Rocket Propulsion Elements", Seventh Edition. John Wiley & Sons, Inc., 2001.

[6] S. R. Vadali, H. Schaub, and K. T. Alfriend, "Initial conditions and fuel-optimal control for formation flying of satellites", in *AIAA Guidance, Navigation and Control Conference*, Portland, OR, Aug. 1999.

[7] G. W. Hill, "Researches in the lunar theory", English, *American Journal of Mathematics*, vol. 1, no. 1, pp. 5–26, 1878.

[8] L. Euler, "Theoria motuum lunae nova methodo pertractata", Springer, Ed., ser. Leonard Euler, Opera Omnia. 1958, vol. 2.

[9] W. H. Clohessy and R. S. Wiltshire, "Terminal guidance for satellite rendezvous", *Journal of the Aerospace Sciences*, vol. 27, no. 9, pp. 653–658, 1960.

[10] J. A. Kechichian, "Motion in general elliptic orbit with respect to a dragging and presessing coordinate frame", *The Journal of the Astronautical Sciences*, vol. 46, no. 1, pp. 25–45, 1998.

[11] W.-y. Chen and W. Jing, "Differential equations of relative motion under the influence of J2 perturbation and air drag", in *AIAA SPACE 2010 Conferences & Exposition*, Anaheim, California, Aug. 2010.

[12] A. Deprit and A. Rom, "The main problem of artificial satellite theory for small and moderate eccentricities", *Celestial mechanics*, vol. 2, no. 2, pp. 166–206, 1970.

[13] H. Schaub, "Spacecraft relative orbit geometry description through orbit element differences", in *14^{th} US National Congress of Theoretical and Applied Mechanics*, Blacksburg, VA, Jun. 2002.

[14] H. Schaub, "Relative orbit geometry through classical orbit element differences", *Journal of Guidance, Control, and Dynamics*, vol. 27, no. 5, pp. 839–848, Sep. 2004.

[15] H. Schaub and K. T. Alfriend, "Hybrid cartesian and orbit element feedback law for formation flying spacecraft", *Journal of Guidance, Control, and Dynamics*, vol. 25, no. 2, pp. 387–393, Mar. 2002.

[16] K. T. Alfriend, H. Schaub, and D.-W. Gim, "Gravitational perturbation, nonlinear and circular orbit assumption effects on formation flying control strategies", in *AAS Guidance and Control Conference*, Breckenridge, CO, Feb. 2000.

[17] M. Pavone, B. Açikmeşe, I. A. Nesnas, and J. Starek, "Spacecraft autonomy challenges for next generation space missions", in *Springer Lecture Notes in Control and Information Sciences*, 2014 Submitted, 2013.

[18] NASA, "Overview of the DART mishap investigation results", Tech. Rep., 2006.

[19] R. T. Howard, A. F. Heaton, R. M. Pinson, and C. K. Carrington, "Orbital express advanced video guidance sensor", in *IEEE Aerospace Conference*, Big Sky, MT, Mar. 2008, pp. 1–10.

[20] National Research Council, "Vision and voyages for planetary science in the decade 2013-2022", Tech. Rep., 2012.

[21] Y. Luo, J. Zhang, and G. Tang, "Survey of orbital dynamics and control of space rendezvous", *Chinese Journal of Aeronautics*, vol. 27, no. 1, pp. 1–11, 2014.

[22] D. Mayne, J. Rawlings, C. Rao, and P. Scokaert, "Constrained model predictive control: stability and optimality", *Automatica*, vol. 36, no. 6, pp. 789–814, 2000.

[23] J. Maciejowski, "Predictive control: with constraints". Prentice Hall, 2002.

[24] C. Petersen, A. Jaunzemis, M. Baldwin, M. Holzinger, and I. Kolmanovsky, "Model predictive control and extended command governor for improving robustness of relative motion guidance and control", in *AAS/AIAA Space Flight Mechanics Meeting*, Santa Fe, NM, Jan. 2014.

[25] S. Di Cairano, H. Park, and I. Kolmanovsky, "Model predictive control approach for guidance of spacecraft rendezvous and proximity maneuvering", *International Journal of Robust and Nonlinear Control*, vol. 22, no. 12, pp. 1398–1427, 2012.

[26] P. A. Felisiak, K. Sibilski, W. Wroblewski, and J. Z. Sasiadek, "Spacecraft rendezvous in elliptical orbit using nonlinear model predictive control", in *AIAA Guidance, Navigation, and Control Conference*, National Harbor, Maryland, American Institute of Aeronautics and Astronautics, Jan. 2014.

[27] M. Saponara, V. Barrena, A. Bemporad, E. Hartley, J. Maciejowski, A. Richards, A. Tramutola, and P. Trodden, "Model predictive control application to spacecraft rendezvous in mars sample return scenario", in *EUCASS Proceedings Series - Advances in AeroSpace Sciences*, vol. 6, 2013, pp. 137–158.

[28] I. Lopez and C. R. McInnes, "Autonomous rendezvous using artificial potential function guidance", *Journal of Guidance, Control, and Dynamics*, vol. 18, no. 2, pp. 237–241, Mar. 1995.

[29] A. B. Roger and C. R. McInnes, "Safety constrained free-flyer path planning at the International Space Station", *Journal of Guidance, Control, and Dynamics*, vol. 23, no. 6, pp. 971–979, Nov. 2000.

[30] F. McQuade and C. R. McInnes, "Autonomous control for on-orbit assembly using potential function methods", *Aeronautical Journal*, vol. 101, no. 1006, R. A. Society, Ed., pp. 255–262, 1997, eng.

[31] F. McQuade, R. Ward, and C. R. McInnes, "The autonomous configuration of satellite formations using generic potential functions", in *3rd International Workshop on Satellite Constellations and Formation Flying*, Pisa, Italy, 2003.

[32] E. Frazzoli, "Quasi-random algorithms for real-time spacecraft motion planning and coordination", *Acta Astronautica*, vol. 53, no. 4-10, pp. 485–495, 2003.

[33] J. Phillips, L. Kavraki, and N. Bedrossian, "Spacecraft rendezvous and docking with real-time, randomized optimization", in *AIAA Guidance, Navigation, and Control and Conference and Exhibit*, Austin, Texas, Aug. 2003.

[34] T. E. Carter and M. Humi, "Fuel-optimal rendezvous near a point in general keplerian orbit", *Journal of Guidance, Control, and Dynamics*, vol. 10, no. 6, pp. 567–573, Nov. 1987.

[35] T. E. Carter, "Effects of propellant mass loss on fuel-optimal rendezvous near Keplerian orbit", *Journal of Guidance, Control, and Dynamics*, vol. 12, no. 1, pp. 19–26, Jan. 1989.

[36] T. E. Carter and J. Brient, "Fuel-optimal rendezvous for linearized equations of motion", *Journal of Guidance, Control, and Dynamics*, vol. 15, no. 6, pp. 1411–1416, Nov. 1992.

[37] T. E. Carter, "Optimal power-limited rendezvous for linearized equations of motion", *Journal of Guidance, Control, and Dynamics*, vol. 17, no. 5, pp. 1082–1086, Sep. 1994.

[38] J. Michael, K. Chudej, M. Gerdts, and J. Pannek, "Optimal rendezvous path planning to an uncontrolled tumbling target", in *19^{th} IFAC Symposium on Automatic Control in Aerospace*, Würzburg, Germany, Sep. 2013.

[39] M. Baldwin, R. S. Erwin, and I. Kolmanovsky, "Robust controller for constrained relative motion maneuvering with disturbance rejection", in *AIAA Guidance, Navigation, and Control and Control Conference*, Boston, MA, Aug. 2013.

[40] S. Zhang, M. Hou, D. Wang, and T. Zhou, "Optimal low-thrust trajectory design and robust tracking control for spacecraft rendezvous", in *Proceeding of the 32^{nd} ChineseControl Conference,*, Xi'an, China, Jul. 2013, pp. 4885–4888.

[41] J. T. Betts, "Survey of numerical methods for trajectory optimization", *Journal of Guidance, Control, and Dynamics*, vol. 21, no. 2, pp. 193–207, Mar. 1998.

[42] R. P. Russell and G. Lantoine, "Optimal control of relative motion in arbitrary fields: application at Deimos", English, *The Journal of the Astronautical Sciences*, vol. 59, no. 1-2, pp. 193–215, 2012.

[43] S. Ueda, T. Kasai, and H. Uematsu, "HTV rendezvous technique and GN&C design evaluation based on 1st flight on-orbit operation result", in *AIAA/AAS Astrodynamics Specialist Conference*, Toronto, Canada, Aug. 2010.

[44] M. Ganet-Schoeller, J. Bourdon, and G. Gelly, "Non-linear and robust stability analysis for ATV rendezvous control", in *AIAA Guidance, Navigation, and Control Conference*, Chicago, Illinois, Aug. 2009.

[45] D. J. Pearson, "The glideslope approach", *Advances in the Astronautical Sciences*, vol. 69, pp. 109–123, 1989.

[46] R. Zanetti, "Optimal glideslope guidance for spacecraft rendezvous", *Journal of Guidance, Control, and Dynamics*, vol. 34, no. 5, pp. 1593–1597, Sep. 2011.

[47] G. Basset, Y. Xu, and K. Pham, "Bio-inspired rendezvous strategies and respondent detections", *Journal of Guidance, Control, and Dynamics*, vol. 36, no. 1, pp. 64–73, Jan. 2013.

[48] H. Yoon and B. N. Agrawal, "Novel expressions of equations of relative motion and control in Keplerian orbits", *Journal of Guidance, Control, and Dynamics*, vol. 32, no. 2, pp. 664–669, 2009.

[49] A. Heydari and S. N. Balakrishnan, "Adaptive critic-based solution to an orbital rendezvous problem", *Journal of Guidance, Control, and Dynamics*, vol. 37, no. 1, pp. 344–350, Jan. 2014.

[50] G. Ortega, "Fuzzy logic techniques for rendezvous and docking of two geostationary satellites", *Telematics and Informatics*, vol. 12, no. 3/4, pp. 213–227, 1995.

[51] R. E. Sherrill, "Dynamics and control of satellite relative motion in elliptic orbits using Lyapunov-Floquet theory", PhD thesis, Auburn University, 2013.

[52] R. E. Sherrill, A. J. Sinclair, S. C. Sinha, and T. A. Lovell, "Time-varying transformations for Hill-Clohessy-Wiltshire solutions in elliptic orbits", English, *Celestial Mechanics and Dynamical Astronomy*, vol. 119, no. 1, pp. 55–73, 2014.

[53] J. Tschauner and P. Hempel, "Rendezvous zu einem in elliptischer bahn umlaufenden ziel", *Astronaut Acta*, vol. 11, no. 2, pp. 104–109, 1965.

[54] A. Sinclair, R. E. Sherrill, and T. A. Lovell, "Review of the solutions to the Tschauner-Hempel equations for satellite relative motion", in *22nd AAS/AIAA Space Flight Mechanics Meeting*, Charleston, South Carolina, 2012.

[55] A. J. Sinclair, R. E. Sherrill, and T. A. Lovell, "Calibration of linearized solutions for satellite relative motion", *Journal of Guidance, Control, and Dynamics*, vol. 37, no. 4, 2014.

[56] A. Sinclair, R. E. Sherrill, and T. A. Lovell, "Use of cartesian-coordinate calibration for satellite relative-motion control", in *24th AAS/AIAA Space Flight Mechanics Meeting*, Santa Fe, New Mexico, 2014.

[57] T. Çimen, "Systematic and effective design of nonlinear feedback controllers via the state-dependent Riccati equation (SDRE) method", *Annual Reviews in Control*, vol. 34, pp. 32–51, 2010.

[58] C. P. Mracek and J. R. Cloutier, "Control designs for the nonlinear benchmark problem via the state-dependent riccati equation method", *International Journal of Robust and Nonlinear Control*, vol. 8, no. 4-5, pp. 401–433, 1998.

[59] J. R. Cloutier, C. N. D'Souza, and C. P. Mracek, "Nonlinear regulation and nonlinear H-infinity control via the state-dependent riccati equation technique: part 1, theory", in *First International Conference on Nonlinear Problems in Aviation and Aerospace*, Daytona Beach, Florida, 1996.

[60] A. Bracci, M. Innocenti, and L. Pollini, "Estimation of the region of attraction for state-dependent riccati equation controllers", *Journal of Guidance, Control, and Dynamics*, vol. 29, no. 6, pp. 1427–1430, Nov. 2006.

[61] Y. Huang and W.-M. Lu, "Nonlinear optimal control: alternatives to Hamilton-Jacobi equation", in *35th IEEE Conference on Decision and Control*, Kobe, Japan, 1996, pp. 3942–3947.

[62] T. Çimen, "State-dependent Riccati equation (SDRE) control: a survey", in *17th World Congress The International Federation of Automatic Control*, Seoul, Korea, Jul. 2008.

[63] W. H. Press, S. A. Teukolsky, W. T. Vetterling, and B. P. Flannery, "Numerical Recipes - The Art of Scientific Computing", Third Edition. Cambridge University Press, 2007.

[64] B. D. O. Anderson and J. B. Moore, "Optimal Control: Linear Quadratic Methods". Prentice Hall, 1990.

[65] D. Kleinman, "On an iterative technique for Riccati equation computations", *IEEE Transactions on Automatic Control*, vol. 13, no. 1, pp. 114–115, Feb. 1968.

[66] P. K. Menon, T. Lam, L. S. Crawford, and V. H. L. Cheng, "Real-time computational methods for SDRE nonlinear control of missiles", in *2002 American Control Conference*, Anchorage, Alaska, May 2002.

[67] D. T. Stansbery and J. R. Cloutier, "Position and attitude control of a spacecraft using the state-dependent riccati equation technique", in *Proceeding of the American Control Conference*, Chicago, Illinois, 2000.

[68] H.-e. Park, S.-Y. Park, and K.-H. Choi, "Satellite formation reconfiguration and station-keeping using state-dependent Riccati equation technique", *Aerospace Science and Technology*, vol. 15, pp. 440–452, 2011.

[69] M. Massari, F. Bernelli-Zazzera, and S. Canavesi, "Nonlinear control of formation flying with state constraints", *Journal of Guidance, Control, and Dynamics*, vol. 35, no. 6, 2012.

[70] M. Massari and M. Zamaro, "Application of SDRE technique to orbital and attitude control of spacecraft formation flying", *Acta Astronautica*, vol. 94, pp. 409–420, 2014.

[71] G. Di Mauro, P. Di Lizia, and M. Lavagna, "Control of relative motion via state-dependent Riccati equation technique", *Advances in the Astronautical Sciences*, vol. 142, 2012.

[72] G. Di Mauro, P. Di Lizia, R. Armellin, and M. Lavagna, "Nonlinear control of leader-follower formation flying", *Advances in the Astronautical Sciences*, vol. 145, 2012.

[73] G. Di Mauro, M. Schlotterer, S. Theil, and M. Lavagna, "Experimental implementation of SDRE method for autonomous rendezvous and docking maneuvering", in 5^{th} *International Conference on Spacecraft Formation Flying Missions and Technologies*, Munich, Germany, May 2013.

[74] D. Lee and H. Pernicka, "Optimal control for proximity ooperation and docking", *International Journal of Aeronautical and Space Science*, vol. 11, no. 3, pp. 206–220, 2010.

[75] D. Lee and H. Bang, "Robust nonlinear full state feedback control for autonomous close range rendezvous and docking of spacecraft", *International Journal of Engineering and Innovative Technology*, vol. 3, no. 2, pp. 544–557, Aug. 2013.

[76] J. R. Cloutier, C. N. D'Souza, and C. P. Mracek, "Nonlinear regulation and nonlinear H-infinity control via the state-dependent riccati equation technique: part 2, examples", in *First International Conference on Nonlinear Problems in Aviation and Aerospace*, Daytona Beach, Florida, 1996.

[77] M. Xin and S. Balakrishnan, "Missile longitudinal autopilot design using a new suboptimal nonlinear control method", in *IEE Proceedings - Control Theory and Applications*, vol. 150, Nov. 2003, pp. 577–584.

[78] G. Krieger, A. Moreira, H. Fiedler, I. Hajnsek, M. Werner, M. Younis, and M. Zink, "TanDEM-X: a satellite formation for high-resolution SAR interferometry", *IEEE Transactions on Geoscience and Remote Sensing*, vol. 45, no. 11, pp. 3317–3341, Nov. 2007.

[79] G. Krieger, I. Hajnsef, K. P. Papathanassiou, and M. Younis, "Interferometric synthetic aperture radar (SAR) missions employing formation flying", in *Proceedings of the IEEE*, vol. 98, May 2010.

[80] S. D'Amico and O. Montenbruck, "Proximity operations of formation-flying spacecraft using an eccentricity/inclination vector separation", *Journal of Guidance, Control, and Dynamics*, vol. 29, no. 3, pp. 554–563, May 2006.

[81] R. Kahle, M. Wermyth, Schlepp, and S. Aida, "The TerraSAR-X/TanDEM-X formation flight: challenges to flight dynamics and first results", in 4^{th} *International Conference on Spacecraft Formation Flying Missions & Technologies*, 2011.